CHAPTER ONE

INTRODUCTION

The knowledge and study of long wave atmospheric radiation (extending from 4 μm to 100 μm and peaking at 10 μm) at the Earth's surface is of fundamental importance and has long been studied both empirically and theoretically. Its applications include meteorology, climatology, remote sensing, the study of radiative cooling of buildings, and solar energy collectors. In recent years, interest in these wavelengths has also grown in the field of site selection for astronomical and astrophysical observatories as a tool to detect the presence of cloud. This latter application will be examined as part of the work discussed in this thesis.

Atmospheric radiation was studied in this work using simple single pixel infrared (IR) radiometers (thermopile detectors) which have been developed by the High Energy Astrophysics group at the University of Adelaide for monitoring clouds over astronomical sites. Those detectors were developed with different fields of views (3^o and 90^o) and have a broad spectral response extended from 5.5 μm to above 20 μm, covering the wavelength around 10 μm which relates to the atmospheric radiation.

The main aims of this project were to investigate infrared emission from clear skies, to understand the key parameters that impact on the clear sky emission and to quantify what level of changes from the clear sky are produced by cloud under different

temperature and humidity conditions, along the line of sight and at different elevation angles.

To achieve these goals it was necessarily firstly to develop sufficient understanding of the detector operation, to develop a good detection system with optimum performance and to conduct the preliminary and detailed calibrations processes necessary for the development of ideal detection systems. The operation of these detectors was studied to determine possible limitations to their performance and to develop a general understanding of the instrument. This means that certain requirements must be placed on the detection system and the performance of the detector should be well established under various conditions.

Measurements of the atmospheric radiation, represented here as sky temperatures, were made using these detectors during different times and seasons of the year between 2001 to 2005 at six places around the world. These are Adelaide in Australia, four sites in Saudi Arabia and at the Pierre Auger cosmic ray site in Argentina. The necessary accessible meteorological variables were also collected from those sites over relevant periods of time.

The thesis presents results mainly for clear sky conditions. Based on these data, using statistical regression analysis, different empirical models for predicting clear sky infrared temperatures were developed for each site. The resulting models can be most appropriately summarized in terms of the correlation between sky temperatures and the available meteorological variables, mainly the screen level temperature and the amount of atmospheric water content, represented by either screen vapour pressure or precipitable water vapour. These models were from either one-variable or two-variable models. Although one-variable models give useful estimations of the clear sky temperature, it was assumed in this study that two-variable models are more reliable and more appropriate as predictors. Two different groups of the two-variable models were produced for each site. The first (*group1*) are those which use the screen level temperature and the total amount of atmospheric water content represented by the precipitable water vapour (PWV). PWV was obtained in this study either from GPS receivers in the case of Adelaide or from radiosondes in the case in the four sites in Saudi Arabia. The second (*group2*) are those which use the screen level temperature and the screen level water vapour pressure. Generally, it was found that *group1* gives a better prediction for clear sky temperatures than *group2*. However, *group2* models were found to have advantages since they use easy-to-measure screen level variables.

Apart from the Auger site, both groups of models were developed for each site. Due to the unavailability of the PWV data at the Auger site, only *group2* models were developed in that case.

For the purpose of detecting the presence of clouds over astronomical sites it is preferable to use models that have accessible variables. Hence the models based on g*roup2* formulae were tested and shown to be reliable in predicting clouds in different atmospheric conditions. The validity of the *group2* models was also checked for each site against some clear sky models found in the literature.

The thesis is divided into three parts. In addition to this introductory chapter, part one also includes chapters 2 and 3. The first half of chapter 2 reviews the fundamentals of atmospheric radiation and atmospheric related topics. The second half reviews the literature of the field, both theoretical and experimental. In chapter 3 the performance and the design concepts of the IR monitors is presented. Calibration procedures and results are also given. Methods and techniques used throughout the project are summarised at the end of this chapter.

The second part of this thesis forms more than one third of the work conducted in this project and is based on data collected from the Adelaide site. These data cover more than four years of recorded observations and come from different cloud monitors with different FOV, different filters, and different zenith angles. They are from both clear and overcast sky conditions. This part contains chapter 4 to chapter 7. Chapter 4 presents the results of parameterizing the clear sky temperature at the zenith using data collected from Adelaide. Chapter 5 investigate the zenith angle dependence of the clear sky temperature. Theoretical justifications for the proposed clear sky models from the last two chapters at Adelaide were carried out using MODTRAN software. These models were also used to predict the level of discrimination necessary to select between skies of different overcast conditions. These processes are presented in chapter 7.

The final part consists of chapters 8 to 11. This work is based on data from different sites and includes the conclusion chapter. In chapter 8, data from IR monitors from four sites and different seasons in Saudi Arabia were used to model the clear sky temperatures over each site. Unified models for these sites were also found. Similarly, a model which predicts the clear sky temperature using data collected using the cloud monitor installed at the Auger project in Argentina was found and is described in chapter 9. For each site, the applicability of some existing clear sky models was tested and compared to the proposed model at that site. In chapter 10, data from all sites are

used to find a universal model capable of predicting the clear sky temperature. The final conclusions from this thesis are given in chapter 11

CHAPTER TWO

ATMOSPHERIC RADIATION

2.1 Introduction

Atmospheric radiation is a field in which the interaction of solar and terrestrial radiation with molecules, aerosols and cloud in the atmosphere as well as with the ground, are studied through the theory of radiation transfer and through radiometric observations from the ground and space. These processes are complex and critical for understanding the atmospheric radiation in many applications. This chapter is intended to review and give the basic ideas, understanding, and quantitative analysis of atmospheric radiation to help the reader to follow the structure of the work in this project. In sections 2.2 and 2.3 we discuss the basic radiation laws, followed by a general description of atmospheric radiation. Atmospheric thermal structure and chemical composition are discussed in sections 2.4 and 2.5 respectively. In section 2.6 we present some of the relevant basic aspects of molecular spectroscopy of the most important atmospheric gases. We

conclude this chapter by giving methods used to calculate atmospheric radiation. These include a theoretical approach plus a literature review of empirical approaches. These two approaches will be taken in this project.

2.2 Basic Radiation Laws

The following discussion is based mainly on Andrews (1998) and Goody and Young (1989). Background radiation is the basic mechanism by which energy is transferred between regions of different temperatures. Thermal radiation is defined as radiant energy emitted by a medium by virtue of its temperature. The intensities and dominant wavelengths of the radiation are a function of the absolute temperature of the radiating medium.

The range of wavelengths commonly associated with thermal radiation lies between 0.l μm and 100 μm. This range is further subdivided into three subranges; the ultra-violet, the visible, and the infrared (IR). Thermal radiation from natural surfaces and from the atmosphere falls within the infrared range. Wavelengths associated with this portion of the spectrum are from 3 μm to 100 μm.

A blackbody is a body, which emits and absorbs, at any temperature, the maximum possible amount of radiation at any given wavelength. The blackbody is a theoretical concept, which sets an upper limit on the emission of radiation in accordance with the second law of thermodynamics. It is also a standard against which the radiation characteristics of other media are compared.

The emissive power of a blackbody is the amount of energy radiated per unit area per unit time. At a wavelength λ in the wavelength range $d\lambda$, the emissive power of a blackbody can be denoted by $B_\lambda \, d\lambda$. B_λ is called the spectral or monochromatic blackbody emissive power. A relationship which yields the emissive power of a blackbody at any temperature and wavelength was derived by Max Planck in 1900. Planck's law states (Andrews, 1998):

$$B_\lambda(T) = \frac{2hc^2}{\lambda^5(\exp(\frac{hc}{k_B T \lambda}) - 1)} \qquad (2.1)$$

or in wave number as :

$$B_{\nu}(T) = \frac{2h\nu^3 c^2}{\exp(\frac{h\nu c}{k_B T}) - 1} \qquad (2.\ 2)$$

where $B_{\lambda}(T)$ is the monochromatic emissive power of a black body ($W/m^2/\mu m$) or ($W/m^2/cm$) at temperature T(K) for the wavelength λ (μm) or wave number (cm^{-1}), and the constants are Planck's constant, h; the Boltzmann constant (k_B) and the velocity of light (c).

From Planck's law the monochromatic emissive power for a blackbody at any particular temperature can be plotted as a function of wavelength. This is shown in figure (2.1 a) for two different temperatures; 5780 K and 255K, the approximate temperatures of the sun and the earth respectively.

Planck's law gives values of zero at λ = 0 and λ = ∞ and reaches a maximum at some finite value of λ. The maximum is larger for higher values of temperature. For a given temperature, the wavelength at which B_{λ} is a maximum is given by Wien's displacement law:

$$\lambda_{max} T = 2897 \quad (\mu m.K) \qquad (2.\ 3)$$

Wien's law shows that the wavelength λ_{max} (in μm) at which the maximum energy density occurs decreases as the temperature increases. For the two temperatures previously considered, the wavelengths at which the blackbody radiation is maximum are:

$$\lambda_{max}(5780K) = 0.49\ \mu m \qquad \text{and} \qquad \lambda_{max}(255K) = 11.36\ \mu m \qquad (2.\ 4)$$

The total energy radiated from a blackbody is the integration of (2.1) over all wavelengths, λ= 0→∞, which gives the well-known Stefan-Boltzman equation for blackbody radiation as:

$$B(T) = \sigma T^4 \qquad (2.\ 5)$$

where σ is the Stefan-Boltzman constant = 5.67×10^{-8} Watts/m^2/K^4. For radiating from non-black surface, the monochromatic emissive power is denoted by R_λ. This quantity can be expressed in terms of the monochromatic emissive power of a blackbody by:

$$R_\lambda = \varepsilon_\lambda B_\lambda \tag{2. 6}$$

where ε_λ is the monochromatic hemispherical emittance of the surface.

The emissive power of a non-black surface at temperature T, radiating into the hemispherical region above it is:

$$R = \varepsilon B = \varepsilon \sigma T^4 \tag{2. 7}$$

where ε is the hemispherical emissivity.
ε_λ is the emissivity at wavelength λ , both ε and ε_λ can be related by:

$$\varepsilon = \frac{1}{\sigma T^4} \int_0^\infty \varepsilon_\lambda \frac{C_1}{\lambda^5 \left(e^{\frac{C_2}{\lambda T}} - 1 \right)} d\lambda \tag{2. 8}$$

If ε_λ is not a function of λ then $\varepsilon_\lambda = \varepsilon$. Surfaces which have this characteristic are called grey surfaces. Because a grey body emits a fixed proportion of the blackbody radiation at all wavelengths, grey surfaces are often assumed in calculations for simplicity.

If a_λ, r_λ and τ_λ represent the fraction of absorbance, reflectance, and transmittance respectively and, I_λ is the monochromatic incident radiation energy per unit time per unit area per μm, then the absorbed part of the radiation must equal the total radiation minus the losses due to reflections away from the surface and transmission through it (Stephens 1994). Hence:

$$a_\lambda I_\lambda = I_\lambda - r_\lambda I_\lambda - \tau_\lambda I_\lambda \tag{2. 9}$$

or

$$a_\lambda + r_\lambda + \tau_\lambda = 1 \tag{2.10}$$

This states that the processes of absorption, reflection, and transmission account for all the incident radiation in any particular situation. For a blackbody a_λ =1, so it follows that, $r_\lambda = 0$ and $\tau_\lambda = 0$. Radiation incident upon any opaque surface is either absorbed or reflected, so that $a_\lambda + r_\lambda = 1$. Moreover, at any wavelength, strong reflectors are weak absorbers, and weak reflectors are strong absorbers.

An important relationship exists between ε_λ and a_λ and can be obtained from Kirchhoff's radiation law. Kirchhoff's law states that for every wavelength the spectral emissivity is equal to the spectral absorptivity. If the source of radiation is thermal equilibrium with the absorbing medium, then (Andrews 1998):

$$I_\lambda = R_\lambda \tag{2. 11}$$

so that

$$a_\lambda = \varepsilon_\lambda \tag{2. 12}$$

Consequently, from Kirchhoff's law, equation 2.10 can be written as:

$$\varepsilon_\lambda + r_\lambda + \tau_\lambda = 1 \tag{2. 13}$$

NOTE: This figure is included on page 10 of the print copy of the thesis held in the University of Adelaide Library.

Figure 2. 1: The normalized blackbody emission spectra, $T^{-4}\lambda B_\lambda$, for the Sun (5780K) and Earth (255K) as a function of $\ln\lambda$ (a) where B_λ is the black body function and λ is the wavelength. The fraction of radiation absorbed from the tropopause (typically at a height of 11km) to the top of the atmosphere as a function of wavelength (b). The fraction of radiation absorbed while passing from the surface to the top of the atmosphere as a function of wavelength (c). The atmospheric molecules contributing the important absorption features at each frequency are also indicated. after Goody and Yung (1989).

2.3 General Description of Atmospheric Radiation

The Earth receives energy from the Sun at wavelengths mostly in the visible and infrared part of the spectrum. This energy is absorbed by the Earth and re-radiated at infrared wavelengths, mainly from 4 μm to 50 μm, due to the absolute temperature of the Earth. The Earth's surface is usually taken as emitting and absorbing as a grey body in the infrared region with emissivities varying between 0.85 to 0.99 depending on the surface conditions (Levi 1980). Of the radiation from the Earth, approximately 90% is absorbed in the atmosphere and the rest is lost to space. The radiation absorbed in the

atmosphere is then re-radiated, either back to Earth or out into space. The net IR radiation received on the Earth's surface is the difference between that radiated from the Earth and that which is re-radiated back to Earth from the atmosphere. The latter is called *atmospheric emission* (Houghton, Taylor and Rodgers, 1984). Atmospheric radiation is due to those gases in the atmosphere that absorb and emit energy in the infrared. Gaseous absorption (and emission) of radiation in the atmosphere is mainly due to water vapour, carbon dioxide, ozone and some minor constituents, such as methane and carbon monoxide. The transmission characteristic of the Earth's atmosphere as a function of wavelength is shown in fig (2.1 b and c).

It is interesting to note that these gases make up less than 1%, by volume, of the earth's atmosphere. Without the absorption and emission by these gases, the average temperature of the earth would decrease approximately 40^{o}C (Sellers 1965).

The atmospheric radiation depends upon sky temperature and the distribution and proportions of water vapor, carbon dioxide, and ozone in the atmosphere. The proportions of carbon dioxide and ozone remain essentially constant; but the proportion of water vapor can change considerably at ground level.

Radiation from the atmosphere can be considered as the sum of the radiation from many discrete layers of atmosphere, with each layer having its own temperature and pressure. Every layer of the atmosphere is involved in the radiation of energy from the sky. However, not all layers contribute the same amount of radiation. Most radiation comes from lowest 100 m of the atmosphere (Sellers 1965). Geiger (1965) gave computations showing the percentage of atmospheric radiation received at ground level contributed by the various layers of atmosphere, the results are illustrated in table (2.1). The first layer, 87 m thick, is shown to contribute no less than 72 % of the total atmospheric radiation.

In addition to the radiation from the atmospheric gases, clouds are also a radiation source. The radiation from the clouds comes from the water and ice particles that make up the clouds. Atmospheric aerosols, on the other hand, mainly scatter the visible incoming solar radiation, (Liou 2002).

NOTE: This table is included on page 12 of the print copy of the thesis held in the University of Adelaide Library.

Table 2. 1: Contribution of various Atmospheric Layers to the Atmospheric Radiation (After Geiger 1965).

2.4 Atmospheric Composition and Structure

Knowing the structure and the composition of the atmosphere is important in understanding the role of which the atmosphere plays in different atmospheric applications. It also enables us to study the radiative transfer problem with its associate absorption and emission.

2.4.1 Thermal Structure

Roughly speaking, the atmosphere is composed of the troposphere and stratosphere. The troposphere extends to about 10 km altitude and is characterized by a decrease in temperature with height from a surface temperature of about 288 K to about 220 K with typical lapse rate of 6.5 K km^{-1}. Almost all water vapour, clouds, and precipitation are confined in this layer. The stratosphere, on the other hand, is characterized by an isothermal layer from the tropopause to about 20 km, figure (2.2). Ozone occurs predominantly in this layer. Solar UV is absorbed by ozone which can produce IR emission at 9.3 μm.

Other quantities describing atmospheric gases such as pressure, density and mean free path vary dramatically with height in the atmosphere. The variation can be over many orders of magnitude and is very much larger than horizontal or temporal variations. The vertical variation of pressure with height may be written as:

$$p(z) = p(0) \exp(-z/H) \qquad (2.14)$$

where *p(z)* is the pressure at height z above sea level, *p(0)* is the sea level pressure, and *H* is a constant called the *scale height*, which is about 8.4 km. Pressure decreases by a factor of e in passing upward through a layer of depth H. Similar behaviour applies to the atmospheric density (see Wallace and Hobbs, 1977 for more details). Above 30 km atmospheric emission is negligible; hence atmospheric structure above this altitude will not be considered.

NOTE: This figure is included on page 13 of the print copy of the thesis held in the University of Adelaide Library.

Figure 2. 2: Temperature profiles of the standard atmospheric models often used in radiative transfer calculations. "Standard U.S. 1976 atmosphere" ■ is representative of the global mean atmospheric conditions; "Tropical atmosphere" ▼ is for latitudes < 30°;"Mid-latitude atmosphere" is for latitudes between 30° and 45°; ○ summer and× winter. "Sub-arctic atmosphere" is for latitudes between 45° and 60°,● summer and + winter (These are standard atmospheres found in the MODTRAN package, Berk et al. (1989).

2.4.2 Chemical Composition

The atmosphere is largely a mixture of gases. In addition there are suspended particles (e.g. aerosol, smoke, ash, etc.) and hydrometeors (e.g. cloud droplets, raindrops, snow, ice crystals, etc). These composition components will be discussed briefly in the following.

2.4.2.1 Atmospheric Gases

Atmospheric gases are divided into two types, some with fairly permanent concentrations, others that are variable in space and time. Table (2.2) lists the chemical concentrations of permanent and variable gases. Nitrogen and oxygen account for more than 98% of the atmosphere by volume. On the other hand, variable gases contributions are small but they are extremely important in the radiation balance in the atmosphere. Figure (2.3) shows the composition of the atmospheric gases up to 120 km. About 99% of the atmospheric mass lies below an altitude of 30km.

NOTE: This table is included on page 15 of the print copy of the thesis held in the University of Adelaide Library.

Table 2. 2: The main constituents of the earth's atmosphere near the earth's surface, ppmv is part per million volume. Liou 2002.

NOTE: This figure is included on page 16 of the print copy of the thesis held in the University of Adelaide Library.

Figure 2.3: Vertical profiles of mixing ratios of some gases in the atmosphere for mean mid-latitude conditions. Adapted from (Liou 2002).

2.4.2.2 Aerosols

Atmospheric aerosols are solid or liquid particles suspended in the air with diameters between about 0.002 μm and 100 μm. They vary in sources, sizes, production mechanism, chemical composition, amount and distribution in space and time. Aerosols found in the atmosphere can either be from direct emission into the atmosphere (for instance, volcanic dust, and smoke) or are produced by gas-to-particles conversion processes (for instance, sulfates). Aerosols scatter incident radiation re-radiating the energy in all directions. They generally have more effect on visible light and little in the IR (see for example, Twomey 1977 and Van de Hulst 1957). The relative intensity of the scattering pattern depends strongly on the ratio of the particle size to the wavelength of the incident wave (figure 2.4). Atmospheric aerosol concentration varies with locality; the largest concentrations generally occur in urban and desert areas (Satheesh and Moorthy 2005).

NOTE: This figure is included on page 17 of the print copy of the thesis held in the University of Adelaide Library.

Figure 2. 1: Scattering regimes for various ranges of the size parameter. Ordinate is scattering particle radius r in microns and the abscissa is the wavelength of incident radiation in microns. Size Parameter $\alpha = 2\pi r/\lambda$. Adapted from Wallace and Hobbs (1977).

2.4.2.3 Clouds

Clouds are composed of tiny water droplets, or ice crystals, which form on cloud condensation nuclei. Only a small fraction of aerosol particles are cloud condensation nuclei (Hartmann1993). Typical concentrations of cloud droplets are of order of 100 droplets/cm^3. Clouds are characterized by their type, coverage, liquid water content, droplet concentration and droplet sizes. On average, droplets of continental clouds have typical radii ranging from 2 to 10 μm, whereas maritime cloud droplets may be larger and range from 3 to 20 μm (Hartmann 1993). The relatively rare giant condensation nuclei may produce drops in the 20 μm to 30 μm range or larger. Clouds scatter visible radiation considerably and hence reflect some of the incoming solar radiation. They emit IR and microwave radiation (e.g. Hartmann, Bell, and Michelsen 1992). They are fairly opaque at IR wavelengths where they can be detected using IR techniques such as with the method used in this study (see chapter 3).

2.5 Important Atmospheric Gases

Understanding the atmospheric absorption produced by the atmospheric gases requires information on their distribution in the atmosphere and understanding of their molecular structure. A brief description of the atmospheric properties and radiative characteristics

of the most important atmospheric gases will be given in the following subsections. These gases are water vapour, carbon dioxide and ozone. More details can be found in standard references (e.g. Goody 1964).

2.5.1 Water Vapour

Water vapour is the most abundant and highly variable component of the relatively important gases in the atmosphere, and it has important absorption bands at both solar and terrestrial blackbody wavelengths (figure 2.1). It contributes more than any other gas to the greenhouse effect. It plays an important role in the hydrological cycle, and has effects on our climate and weather systems (Czajkowski *et al*. 2002). Water vapour alters the attenuation of electromagnetic radiation through the atmosphere, which is of significance in fields of astronomy, radar, communications and remote sensing. It has an effect on the temperature of the atmosphere at whichever level it occurs, having a large impact on the formation of temperature inversions. Water vapour concentration varies with space and time. More than 50 % of it is concentrated below 1 km and 90% below 4 km. The concentration of the water vapour is relatively small in the stratosphere. The water vapour content of air is a strong function of air temperature. For example, air at 40 ^{o}C can hold up to 49.8 grams of water per kg of dry air, while at 5 ^{o}C this reduces to 5.5 grams per kg of dry air (Andrews 1998). The major sources of water vapour are evaporation and transpiration from plant life. The main sink is condensation in clouds with resulting precipitation over oceans and land. On average, the concentration of atmospheric water vapour decreases with altitude, although this distribution may be reversed from time to time. The release of latent heat from condensation of water in the atmosphere is significant in the global energy budget and climate. Relatively small amounts of water vapour can produce great variations in weather. This is largely due to changes in its concentration and in latent heat release, particularly below about 6 km (Aguado and Burt 2004). Various units used to quantify the amount of water vapour in the atmosphere include dew point, saturation pressure, vapour pressure, absolute humidity, water vapour density and relative humidity.

It is common to represent the water vapor content in the atmosphere by what is known as integrated or precipitable water vapor (*PWV*). Precipitable water vapor is the amount of water obtained if all the water vapor in the atmosphere were to be compressed to the point at which it condenses into liquid. This can be derived by summing the water

vapor density distribution or by the knowledge of scale height of water vapor (H_{sc}, [km]):

$$PWV = \sum_i (z_{i+1} - z_i) \times \rho_i \qquad (2.\ 15)$$

Also,

$$PWV = \rho_0 \times H_{sc} \qquad (2.\ 16)$$

where z_i is the altitude in km for the *i*th layer of the atmosphere ρ_i is the water vapor density at the *i*th layer [g/m^3] and ρ_o is the surface water vapor density [g/m^3].

Scale height is defined as the altitude at which water vapor falls to *1/e* of the total precipitable water vapor. Almost 99% of the water vapor lies below the altitude corresponding to 2.7 times the scale height.

The values of the screen level vapor pressure and the PWV will be used frequently in this thesis as a representative to atmospheric water content.

Quantifying the amount of water in the atmosphere has a great importance for many fields of study, including meteorological and weather modelling, astronomical and atmospheric applications. Although it was not original aim of this project, a method was found to derive the PWV in the clear atmosphere using measurements from IR cloud monitors (See chapter 4).

2.5.2 Carbon Dioxide

Carbon dioxide has a relatively constant mixing ratio with height in the atmosphere. That is, it is fairly evenly distributed on average. The main sources of carbon dioxide are the burning of fossil fuels, human and animal respiration, the oceans and volcanic activity (Drake 2000 and Field and Raupach 2004). Although it is known as a permanent atmospheric gas, the concentration of carbon dioxide (a greenhouse gas) in the atmosphere has been rising steadily by about 0.4% per year since the early part of this century (Hansen 2004). It is estimated that the annual amount of carbon dioxide entering or leaving the air by all mechanisms is about one tenth of the total carbon dioxide content of the atmosphere. Figures (2.5) and (2.6) shows an example of the

change of the atmospheric concentration of CO_2 over Tasmania in Australia in the past 20 years (Hopler 2001)[1], and the history of its concentrations as directly measured at Mauna Loa, Hawaii.

NOTE: This figure is included on page 20 of the print copy of the thesis held in the University of Adelaide Library.

Figure 2. 5: Shows the variations of CO2 concentration of Tasmania in Australia during the last 20 years. (Holper 2001).

1 http://www.cmar.csiro.au/e-print/open/holper_2001b.html

NOTE: This figure is included on page 21 of the print copy of the thesis held in the University of Adelaide Library.

Figure 2. 6: Measurements of atmospheric carbon dioxide concentration at Mauna Loa, Hawaii. The red curve shows the average monthly concentrations, and blue curve is a moving 12 month average. (Source: C.D. Keeling. and T.P. Whorf. 2006, Scripps Institute of Oceanography, University of California).

2.5.3 Ozone

The concentration of ozone is highly variable in space (latitude and altitude for example) and time. Most of the ozone is generated and destroyed by photochemical reactions (photodissociation of molecular oxygen) in the layer between 20 km and 60 km (McElroy 2002). Ozone tends to accumulate in the lower stratosphere at altitudes between 15 and 25 km with a maximum concentration at 20 to 25 km, depending on latitude and season. Small amounts of ozone are also produced by electrical discharges and in photochemical smog over cities. At the surface, ozone is destroyed rapidly by reacting with plants and dissolving in water, whereas in the stratosphere its lifetime is on the order of months. Ozone has characteristic pronounced absorption at UV, IR and microwave wavelengths. The absorption of UV radiation makes human life possible on the Earth's surface.

Figure (2.7) shows an atmospheric profile for the atmospheric concentration of the three gases as a function of altitude.

NOTE: This figure is included on page 22 of the print copy of the thesis held in the University of Adelaide Library.

Figure 2. 7: Distribution of the radiative main constituents with altitude for the mid-latitude summer standard atmosphere as defined by McClatchy 1971, in MODTRAN code Berck et al.(1989).

2.5.4 Nitrous Oxide, Methane and Other Trace Gases

Nitrous Oxide is one of a group of nitrogen compounds found in the atmosphere that includes NO, NO_2, HNO_3 and NH_3. These nitrogen compounds are very important in the photochemistry of smog and ozone chemistry of the stratosphere. Produced naturally by biological activity, nitrous oxide is of concern because it has an infrared band at 1350 cm^{-1}. Absorption at this band strengthens and broadens the absorption band already presented by methane.

Methane primarily reaches the atmosphere from natural biological sources. It has an absorption band at 1350 cm^{-1}, which is usually heavily masked by water vapour. Methane is an important greenhouse gas; however, it has a less important effect in the radiation balance of the atmosphere in low resolution spectra.

Similarly trace gases with minor concentrations, listed in table (2.2), have little effect on the atmospheric IR especially at lower resolutions. For the purpose of this thesis trace gases, methane and nitrous oxides will not be considered any further.

2.6 Interactions between Radiation and Molecules

This section will briefly discuss the basic mechanisms of interaction between radiation and matter, which lead to the production of absorption lines. This discussion will be completed by giving a summary of the main absorptions bands for the most important atmospheric gases discussed in section 2.5, mainly water vapour, carbon dioxide and ozone. More detail and discussions in the topic of this section can be found in Banwell (1983) and McCartney 1983.

2.6.1 Vibration and Rotational Energies

The origin of atmospheric absorption and emission lies in the exchange of energy between molecules and electromagnetic fields. The long-wave infrared radiation is absorbed strongly by certain minor atmospheric gases. This absorption is very spectrally dependent.

The radiation is absorbed in spectral bands in which the absorption band consists of many individual narrow spectral lines. The production of the absorption spectra, which is a result of interactions between the incident radiation and molecules, requires that the molecule posses an electric or magnetic dipole moment. This moment exists whenever the effective centres of positive and negative charges of the molecule have non-zero separations. Interaction of the dipole moment and the electromagnetic field effectively couples the molecules and the fields. The polarizability of the molecule is related to the extent to which a molecule has a permanent dipole moment or can acquire an oscillating one produced by its vibrational motion. Most species of IR active molecules, such as, CO, N_2O, H_2O and O_3, have a permanent electric dipole because of an asymmetrical charge distribution. On the other hand N_2, O_2, CO_2 and CH_4 do not have permanent dipoles. However, as molecules like CO_2 and CH_4 vibrate, an oscillating electrical dipole moment is produced and radiation interaction can take place, hence CO_2 and CH_4 posses vibrational-rotational couplings with incident waves (Banwell 1983).

The N_2 and O_2 species have symmetrical charge distributions; hence they have no permanent electric dipole and no IR activity. However, both species have a weak magnetic dipole moment that permits radiative activity in the UV and to a slight extent in the visible.

The excitation energy of a molecule is of three types (McCartney 1983):

(a) Electronic excitation; occurs when the orbital electrons change in the individual atoms. This transition requires large amount of energy, hence the resulting spectra are found in the ultraviolet, visible and near IR;

(b) Rotational excitation: occurs when the molecule rotates about their center of mass. The changes of rotational energy are small (10^{-4} eV) and spectral lines produced are in the far IR and microwave regions. These absorption lines are well separated and are related to the transformation from one discrete rotational state into another (Rizzi 1998).

(c) Vibrational excitation: occurs when the individual atoms vibrate with respect to the combined molecular centre of mass. Here, the atoms in the molecule are assumed to be bound by a weak spring that resists deviation of the distance between the atoms from its equilibrium point. During vibration, the molecules can stretch and compresses in a mode called antisymeterical stretch to produce an electric dipole. In this case one bond stretches while the other compresses and vice versa. The vibrational energy is typically about 10^{-1} eV and is found in the IR region of the spectrum. Since vibrational energies are roughly a thousand times greater than rotational energies, vibrational lines rarely occur alone, but usually in conjunction with rotational lines.

A combination of rotational and vibrational energy transitions causes absorption lines in the region of 1 μm to 20 μm. The existence of both types of process leads to very complex structure (e.g. the vibrational-rotational band of H_2O around 6.3 μm) as an enormous number of lines are involved, which rapidly overlap each other.

2.6.2 Absorption Bands for Some Important Atmospheric Gases

2.6.2.1 Water Vapor Molecules

The water vapor molecule is a triatomic non-linear molecule, with a rich and complex vibration spectrum in the IR (McCartney 1983). It is of the asymmetric top (bent triatomic) configuration, which has three fundamental vibration modes, figure (2.8). The v_1 and v_2 fundamental vibrations, involving stretching of the chemical bonds, are at short IR wavelengths, 2.74 μm and 2.6 μm respectively, (3657.05 cm^{-1} and 3755.92 cm^{-1}). The v_3 fundamental due to bending of the bands is centered at 6.25 μm (1594.78 cm^{-}

[1]), and in combination with rotational transitions is responsible for very strong 6.3 μm bands, the wings of which extend from at least 5 μm to 9 μm. A pure rotational band of water vapor extends, with varying intensity, from about 18 μm to beyond 100 μm, fig (2.9), with wings overlapping parts of the 15 μm CO_2 band (Goody 1964).

NOTE: This figure is included on page 25 of the print copy of the thesis held in the University of Adelaide Library.

Figure 2. 8: Vibrational modes of diatomic and triatomic atmospheric molecules. Adapted from McCartney (1983).

2.6.2.2 Carbon Dioxide Molecules

Carbon dioxide is a triatomic molecule with a linear symmetrical configuration, which means that the CO_2 molecules have no permanent electric dipole. The CO_2 molecule has three vibrational modes: v_1 for symmetric stretch, v_2 for bending motion and v_3 for anti symmetrical stretch. Because of the symmetry of the molecule, the v_1 has no spectrum in the IR. The v_2 fundamental is centred at 14.95 μm. Together with a number of overtone and combination bands it is responsible for the very strong 15 μm band of CO_2 (figure 2.10). The v_3 bands are centered near 4.3 μm and are very strong, but they are at a low intensity region of both terrestrial and solar radiation and have minor influence in the energy exchange in the atmosphere. Other bands of CO_2 in the IR occur at 5 μm

and at about 9.4 μm and 10.4 μm. These are weaker than those mentioned above and are of less importance in atmospheric radiation (Drayson *et al* 1972).

NOTE: This figure is included on page 26 of the print copy of the thesis held in the University of Adelaide Library.

Figure 2. 9: Absorption spectrum of the water vapor rotational band beyond 18 μm, at high resolution. Adapted from Rizzi (1998).

NOTE: This figure is included on page 26 of the print copy of the thesis held in the University of Adelaide Library.

Figure 2. 10: Same as figure (2.9) but for the carbon dioxide rotational band near 15 μm, at high resolution. Adapted from Rizzi (1998).

2.6.2.3 Ozone

The ozone molecule is of triatomic non-linear type with a relatively strong rotation spectrum. The three fundamental vibrational bands are v_1, v_2, v_3 and occur at wavelength of 9.066 µm, 14.2 µm and 9.597 µm respectively. The very strong v_3 and moderately strong v_1 combine to make the well-known 9.6 µm band of ozone. This band has a very significant influence on the IR radiation budget of the atmosphere, particularly at higher altitudes. This is because it occurs at the atmospheric window of other gases and is located near the maximum of the Planck black-body curve for atmospheric temperatures.

Table (2.3) summarizes the energy transitions, the band intervals and centres for some of the most important atmospheric gases.

NOTE: This table is included on page 28 of the print copy of the thesis held in the University of Adelaide Library.

Table 2. 3: The most important vibrational and rotational transitions for H2O, CO2, O3, CH4, N2O, and CFCs.(McCartney 1983).

2.7 Method of Calculating the Atmospheric Radiance

There are two methods for estimating thermal atmospheric radiance. The first is practical and the second is empirical (Berdahl and Fromberg 1982). In the following two sections a summary of these two techniques will be given.

2.7.1 Practical Approach

This technique is called “detailed”, in the sense that it utilizes the detailed spectral profiles of atmospheric constituents together with knowledge of their radiative properties to derive the atmospheric radiance. This method is accurate. However, it needs detailed input information for the state of the atmosphere and information concerning the radiative properties of atmospheric constituents.

In the IR region of the spectrum from 5 μm to 25 μm and beyond, the atmospheric emission can be determined by numerical integration of the equation of radiative transfer (RT) to give the upward radiance. McClatchy *et al* (1971) expressed the upward radiance as $L_{\uparrow}$:

$$L_{\uparrow} = \int_{\tau_{rg}}^{1} B(\nu, T)\, d\, Tr_{\nu} + B(\nu, T_g)\, Tr_g \qquad (2.17)$$

where the integral represents the atmospheric contribution. The contribution from the surface (ground or lower boundary), modified by the total atmospheric transmittance Tr_g between the boundary and the observer is given by the second term. Tr_{ν} is the spectral transmittance (see equation 2.18) which ranges from 1 at the level of observation to Tr_g at the lower boundary (for example, the earth’s surface or cloud top); $B(\nu, T)$ is the black body radiance corresponding to a frequency ν and the average temperature T of an atmospheric layer, and T_g is the ground temperature.

The clear sky (downward) atmospheric emission can be obtained by excluding the second term of equation (2.17) and assuming that Tr_g is the transmittance of the entire atmosphere. In a cloudy sky the subscript, g, refers to a cloud base.

Transmittance of radiation in the atmosphere is, however, more complex due to the dependence of the scattering and absorption coefficients on a number of physical properties of the atmosphere. For monochromatic radiation along a path in the atmosphere the monochromatic transmittance is defined as:

$$Tr_{\nu} = exp(-\tau_{\nu}) \qquad (2.18)$$

Where τ_{ν} is the optical depth defined as (Berger 1988):

$$\tau_{\nu} = \int_{u}^{u_1} \kappa_{\nu} \, du \qquad (2.19)$$

u is the path length written as (LaRocca 1978):

$$u = \int_{z_1}^{z_2} \rho(z) \, dz \qquad (2.20)$$

$\rho(z)$ is the density of the absorber at level z and z is the altitude of the layer.

The absorption line coefficient κ_v is defined by the position, strength and shape of the spectral line, and is written as (LaRocca 1978):

$$\kappa_{\nu} = S f(\nu - \nu_0) \qquad (2.21)$$

Where $f(v\text{-}v_o)$ is the shape factor of the spectral line, v_0 is the wavenumber of the central position of a line and S is the line strength.

The expression of κ_v is linked to the nature of the spectral lines; Lorentz, Doppler Voigt (i.e. mixed Lorentz-Doppler) (LaRocca 1978).

Calculations of the atmospheric transmittance (function of absorption coefficient and equivalent absorber amount) require knowledge of the attenuation coefficient and the total amount of the absorber. The calculations of the attenuation coefficient are divided essentially into three parts (McClatchy *et al* 1971): the contribution from molecular scattering, molecular absorption and that due to aerosol particles. The molecular scattering coefficient can be easily obtained using Rayleigh's law. For larger size aerosol particles, the aerosol attenuation coefficient has to be computed from Mie scattering theory.

Molecular absorption, on the other hand, is even more complex. The absorption coefficient κ_v over a single molecular absorption line varies according to the variations of the *line width* and *strength*.

The line width is a function of gas pressure and temperature. The line strength is a function of the molecular transition and also temperature. The factors that govern the strength of absorption and emission lines are derived from molecular, statistical and quantum mechanics theory. Spectroscopic databases, such as HITRAN, Rothman *et al.* (1992), include information about the line strength at a reference temperature and some

quantum mechanical information needed for the calculation of the line strength and its temperature dependence.

Calculations of atmospheric transmission using this detailed technique fall into two categories. The *first group* of models are those that sum the contributions of each molecular absorption line to the total absorption, it is called *Line-By-Line models*, LBL. The strategy to perform LBL calculations is to solve the equation of radiation transfer, as follows, Ellingson, and Fouquart, (1991). Calculate a monochromatic optical depth for a layer by summing the contribution of all absorption lines, then sum layers vertically, and then integrate across the spectrum. The LBL calculations were first applied to specific bands such as H_2O (Calfee and Gates, 1966), CO_2 (Drayson, 1966) and O_3 (Aida, 1975).

Line-by-line models are accurate but very expensive to run. They use complex algorithms to speed up the computation time. The FAS transmission CODE (FASCODE), Clough *et al* (1988) and the Line By Line Transmission Model (LBLRTM), Clough and Iacono (1992, 1995) are examples of the LBL codes.

However, this method encounters the difficulty of the availability of spectral line information for some molecules, and considerable computer time is required for the thousands of lines constituting an absorption band.

The *second group* are semi-empirical models, which use various *band models,* BM. Absorption BMs are developed in order to compute the atmospheric absorption over spectral bands to simplify the computation of the spectral transmittance. Band models are simple expressions for the mean transmittance over a spectral band with many absorption lines. The basic approach of these models is to divide the spectrum into finite spectral intervals that are small enough, Δv usually 10-100 cm^{-1}, to regard the $B(T)$ in equation (2.17) as a constant across the interval, yet are wide enough to smooth out the detailed spectral features. The parameters for a given spectral interval are specified either from laboratory observations or by forcing agreement with spectroscopic theory. Elsasser (1938, 1942) and Goody(1952, 1964) are examples of the well-known band models

The Elsasser band model (1938) consists of an array of equally spaced identical lines. This model has been applied to absorption bands, which have a regular line structure, for example, to some bands of CO_2. The Goody model (1952), on the other hand, assumes that the band is composed of spectral lines with an exponential intensity distribution and with random spacing between lines. This model has been applied to

bands, which have an irregular structure, e.g. some H_2O bands Mayer (1947). A number of other band models have been developed, but most are modifications of these two.

Due to the variations of the line half-width with pressure, temperature and concentration over vertical paths in the atmosphere, the band models need to have some adjustments to account for inhomogeneous paths. The basic strategy to solve this problem and account for inhomogenousity is to reduce the radiation transfer problem to that of a homogonous path with some sort of averaged values of temperature, pressure and the absorber amount so that the spectral line properties and optical depth can be computed accurately. One parameter and two parameter scaling procedures are the most commonly methods used to solve this difficulty (Goody and Young 1989).

One parameter approximation is the method used to scale the absorber amount. The procedure of doing so is to find an equivalent homogenous path at fixed reference pressure and temperatures, and the results in the band model having the correct transmission. This procedure was used in the LOWTRAN model (McClatchy *et al* 1971). More accurate band transmission for inhomogeneous paths is obtained with the *two-parameter approximation* this is known as Curtis-Godson approximation, which was developed, independently by Curtis (1952) and Godson (1953). The concept of this approximation is to adjust the line strength and the line-half width. This approximation was used in MODTRAN code, Berk *et al* (1989).

These scaling procedures in connection with an appropriate band model are commonly used in developing atmospheric IR codes.

LOWTRAN, FASCODE, MODTRAN and MOSART are examples of several algorithms have been developed and are available nowadays to calculate the atmospheric transmittance and radiance.

In this project, the MODTRAN4 package was used to perform various IR atmospheric related tasks including various investigations and comparisons with the experimental data.

2.7.2 Empirical Approach

This method uses direct measurements of the sky radiance correlated with some meteorological variables to predict the radiance. Empirical studies are another, and easier, way to study atmospheric radiation. They can help provide a simplified method

to find the key parameters impacting on, for example, the net clear sky atmospheric emission. The upward radiation can be calculated from the Stefan-Boltzman law with knowledge of the absolute temperature and the emissivity of the surface from which the radiation originates, equation (2.6). The atmospheric radiation can be expressed in two ways (Ramsey *et al*. 1982):

1- The sky may be assumed to behave like blackbody, with emissivity of 1, where in this case the atmospheric radiation is given by:

$$R_{sky} = \sigma T_{sky}^{4} \qquad (2.22)$$

2- The sky may be assumed to be a grey body with an apparent emissivity, ε_{sky} , defined as :

$$R_{sky} = \sigma \varepsilon_{sky} T^{4} \qquad (2.23)$$

In both equations R_{sky} is the measured atmospheric radiation, T and T_{sky} are the screen level (air) temperature and the sky temperature respectively (both in K) and σ is Stefan-Boltzman constant, ε_{sky} is the sky emissivity.

Most of the developed simple formulae are based on the statistical fitting of measured radiation and screen level parameters. Alternatively, some simple formulae can be obtained from the integration of the radiative transfer equations with the help of some simplification hypothesis that allows an approximate analytical solution in terms of screen level variables (Brutsaert, 1975 and Prata 1996).

In this section some of the proposed empirical formulae for calculating clear sky radiation at the zenith will be discussed first. Also some formulae for calculating the radiation at different zenith angles will be given. Finally, models used in calculating overcast conditions will be summarized.

2.7.2.1 Clear Sky Models (At the Zenith)

In the following discussion T, and *eo* will represent the screen level temperature in K and screen level water vapor pressure in mb unless otherwise stated. T_{dp} is the dew point temperature and is always in ^{o}C

The first significant work on calculating IR radiance using the empirical approach was conducted by Angstrom (1915) and Brunt (1932), each of whom devised a simple equation for the emissivity (ε_{sky}) that depended only on surface screen level water vapor pressure *eo*. Angstrom's equation takes the form:

$$\varepsilon_{sky}(eo) = A - B \times 10^{-Ceo} \tag{2. 24}$$

where *A*, *B* and *C* are empirical constants which have assigned values in the range (0.75 to 0.82), (0.15 to 0.33) and (0.09 to 0.22) respectively.

The Brunt formula is:

$$\varepsilon_{Sky}(eo) = a + b \times \sqrt{eo} \tag{2. 25}$$

where *a*, and *b* constants which depend upon local conditions and *eo* is the vapor pressure in mb. In fact Brunt's formula is preferable at ground level, and it has only two adjustable constants. Several investigators (e.g. Monteith 1961, Centro 1982) have adopted this formula in their studies, and found that the values of *a* and *b* fall in the range (0.3 to 0.71) and (0.023 to 0.110) respectively.

Efimova (1961) studied the clear sky emissivity over 24 sites in the USSR and found:

$$\varepsilon_{sky}(eo) = (0.746 + 0.0066 \times eo) \tag{2. 26}$$

Elsasser (1942), Anderson (1954) and Marshunova (1966) also found an expression for the clear sky emissivity which depended on the screen vapor pressure. Their forms respectively were:

$$\varepsilon_{sky}(eo) = 0.672 + 0.0412 \times ln\, eo \tag{2. 27}$$

$$\varepsilon_{sky}(eo) = (0.67 + 0.05 \times \sqrt{eo}) \tag{2. 28}$$

$$\varepsilon_{sky}(eo) = (0.68 + 0.036 \times \sqrt{eo}) \quad (2.29)$$

In an attempt to overcome the locality specified in equations (2.24) to (2.29) Swinbank (1963) undertook a reevaluation of the subject. He firstly established a relation between sky flux and σT^4 exclusive of *eo*, from certain measurements made in the UK. Then, from observations in Australia and the Indian Ocean, he related the sky flux to the sixth power of the temperature T

$$R_{sky} = 5.31 \times T^6 \quad (2.30)$$

$$\varepsilon_{sky}(T) = 9.365 \times 10^{-6} T^2 \quad (2.31)$$

where *T* is the ambient temperature in K. Swinbank's formula is acknowledged to be a significant improvement over most relations and has provided the universality lacked by the Angstrom and Brunt formulas. However, Swinbank's regression equation is based on night-time data. Paltridge (1970) found experimentally that there are biases towards inversion conditions. Deacon (1970) also noted that Swinbank did not give a theoretical justification for his T^2 dependence of ε_{sky}.

Idso and Jackson (1969) argued that the Swinbank formula does not cover a large enough temperature range to make his conclusion of universal validity. They then proposed a formula:

$$\varepsilon_{Sky}(T) = (1 - C\,exp[-d(273 - T)]^2) \quad (2.32)$$

where C and d are constants and T is the ambient temperature in K. They concluded that their formula accurately describes a general relation between clear sky emissivity and screen level air temperature and is valid at any latitude and for any air temperature reached on earth.

Zillman (1972) and Ohmura (1981) proposed formulae for clear sky emissivity with similar dependences on the screen level temperature as Swinbank, these respectively are:

$$\varepsilon_{sky}\ (T) = (9.2 \times 10^{-6} \times T^2) \quad (2.33)$$

$$\varepsilon_{sky}\ (T) = \ (\ 8.733\times10^{-3}\times T^{0.788}\ ) \quad (2.\ 34)$$

Brutsaert (1975) showed that an analytical equation could be derived for clear sky emissivity that again utilized vapor pressure and air temperature at screen level. The result is:

$$\varepsilon_{Sky}(eo,T) = 1.24(\frac{eo}{T})^{\frac{1}{7}} \quad (2.\ 35)$$

In fact, this equation has been derived using radiative-transfer theory with some approximations. In reality such an empirical relation represents the emissivity of a slab of water vapor path which includes CO_2.

Similarly, Srinivasan (1982) adopted a semi-empirical procedure by using laboratory data for water vapor emissivites. He then proposed a formula for ε as a function of local temperature, water vapor scale height, and temperature lapse rate. The result is:

$$\varepsilon_{Sky}(eo,T) = 0.684(\frac{eo^{1/9}}{1+\frac{H}{Hw}})\{1+\frac{0.20(-0.117\times\gamma)}{1+(\frac{H}{Hw})}\}+0.0656-0.0003(T-288) \quad (2.\ 36)$$

where H (in km) is the scale height, H_w (in km) is the scale height of water vapor and γ (in ^oC/km) is the lapse rate.

Satterlund (1979) developed an empirical model which also depends on both screen temperature and vapor pressure. His model was:

$$\varepsilon_{sky}(eo,T) = 1.08[1-exp\{-eo^{\frac{T}{2016}}\}] \quad (2.\ 37)$$

An excellent comprehensive study was conducted by Idso (1981) in Arizona, involving the monitoring of the full sky thermal radiation spectrum and the flux in the ranges 8 μm – 14 μm and 10.5 μm-12.5 μm. He reasoned that the relationship between water vapor and thermal emissivity of the clear sky atmosphere is due to the variable

atmospheric concentration of water dimers – pairs of water molecules linked together by weak hydrogen bonds.

With this physical model he proposed three equations relating the clear sky emissivity of the atmosphere in both the 10.5 μm -12.5 μm, 8 μm-14 μm bands and the full thermal spectrum, to the screen vapor pressure and screen temperature:

$$\varepsilon_{10.5-12.5}(T,eo) = 0.10 + 3.53\times10^{-8}\times eo^{2}\times exp(\frac{3000}{T})$$

$$\varepsilon_{8-14}(T,eo) = 0.24 + 2.98\times10^{-8}\times eo^{2}\times exp(\frac{3000}{T}) \qquad (2.\ 38)$$

$$\varepsilon_{Full}(T,eo) = 0.70 + 5.95\times10^{-5}\times eo^{2}\times exp(\frac{1500}{T})$$

In a different approach, Centro (1982) conducted a long study of more than twenty years of sky radiation measurements over different sites in Venezuela at night using various methods. He found that the clear sky emissivity can be calculated under a variety of conditions, air temperatures from –10 ^{o}C to + 30 ^{o}C, and relative humidity RH ranges from 40 to 100 %, and site altitude (Z) from 0 to 3 km above mean sea level MSL, and sky nebulosity from clear to complete cloudy sky. The formula is:

$$\varepsilon_{Sky}(T,RH,Z) = (1-N)\times(5.7723+0.9555\times(0.6017)^{Z}]\times10^{-4}\times T^{1.1893}\times RH^{0.0665} + N(1-(3000+175)\times Z^{0.635})\times RH^{-3/2}\times T^{-1})^{4} \qquad (2.\ 39)$$

For N = 0 (the nebulosity factor), clear sky conditions, the second term can be removed. Andreas and Ackley (1982) proposed a model which depends on both temperature and vapor pressure:

$$\varepsilon_{sky} = [0.601 + 5.95\times10^{-5}\times eo\times exp(1500/T)] \qquad (2.\ 40)$$

Clark and Allen (1978) employed the dew point temperature T_{dp}(^{o}C) to summarize the result of 800 clear sky measurements of IR radiation at San Antonio, Texas. They found a logarithmic relation between sky emissivity and T_{dp} for both nighttime and daytime in the form:

$$\varepsilon_{Sky}(T_{dp}) = 0.787 + 0.764\, ln[\frac{(T_{dp} + 273)}{273}] \quad (2.41)$$

Berdhal and Foromberg (1982) and later Berdhal and Martin (1984) have designed a radiometer particularly to obtain extensive measurements, at 6 sites for 57 months, of the angular and spectral distribution of the sky radiation. They concluded that for monthly averages the clear sky emissivity is a function of dew point temperature and written as:

$$\varepsilon_{Sky}(T_{dp}) = 0.711 + 0.56(\frac{T_{dp}}{100}) + 0.73(\frac{T_{dp}}{100})^2 \quad (2.42)$$

Bliss(1961) and Berger *et al*. (1984) proposed models that also containing the dew point temperature. These respectively are:

$$\varepsilon_{sky}(T_{dp}) = 0.00344 \times (T_{dp} + 273.16) - 0.037 \quad (2.43)$$

$$\varepsilon_{sky}(T_{dp}) = 0.77 + 0.0038 \times T_{dp} \quad (2.44)$$

Where the T_{dp} in equations (2.41) to (2.44) is in ^{o}C

Prata (1996) proposed a formula to calculate the full hemispheric infrared flux (or sky emissivity) at the surface over the full infrared spectrum band. His formula mainly depends on screen-level air temperature and water vapor pressure. This formula is

$$\varepsilon_{Sky} = 1 - (1 + \xi)\exp(-(1.2 + 3\xi)^{1/2}) \quad (2.45)$$

Where $\xi = 46.5(\frac{eo}{T})$

or, in another form,

$$\varepsilon_{Sky}(eo, T) = \{1 - (1 + 46.5(\frac{eo}{T}))exp[1 - (1.2 + 3.0 \times 46.5(\frac{eo}{T}))]\} \quad (2.46)$$

Prata has tested his formula extensively using measurements covering a large range of environmental temperatures (-40 ^{o}C to 40 ^{o}C) and by using different radiosonde profiles. He compared his formula with an accurate LOWTRAN computer model and concluded that there was successful agreement.

Zapadka *et al* (2001) studied the long wave radiation budget at the Baltic Sea and found:

$$\varepsilon_{sky}(eo,T) = 1 - 0.35 \times exp(-\frac{eo}{(T+273)}) \qquad (2.47)$$

Where *eo* in mb and *T* in ^{o}C

In studying the IR atmospheric radiation at two sites at different altitude, Izmon *et al.* (2003) proposed a model such as:

$$\varepsilon_{Sky}(T,eo) = [1 - X_s \, exp(-(\frac{Y_s eo}{T})] \qquad (2.48)$$

The empirical constants X_s and Y_s have values of 0.35 and 10 Kmb^{-1}, respectively, for low land site and values of 0.43 and 11.5 Kmb^{-1} for mountain sites.

Dilley and O'Brien (1998) developed a long wave (LW) scheme for calculating clear sky radiation, which depends on the screen level temperature and the precipitable water, *PWV* (kg/m^2):

$$R_{Sky} = 59.38 + 113.7(\frac{T}{273.16})^6 + 96.96\sqrt{\frac{PWV}{25}} \qquad (2.49)$$

They empirically tuned their parameterization using an accurate radiative transfer model and have obtained good results using this model. It is interesting to notice that their model can be considered as an extension of the Swinbank scheme (Eq 2.31), because of the T^6 term.

Apart from the model proposed by Dilley and O'Brien (1998) which uses the PWV variable, it is obvious that all the proposed models for calculating IR clear sky radiation (or emissivity) fall in one of five categories:

1. Those which contain only the screen level vapor pressure in linear, exponential, or other form (*eo*).

2. Those which contain only the screen level temperature in different forms (T).
3. Those which contain both of the parameters.(eo,T).
4. Models that parameterize the emissivity/ IR radiation as a function of dew-point temperature (T_{dp}).
5. Semi-empirical models that have a factor of the scale height relating the screen level parameters to the upper level contents e.g. Prata , Srinivasan and Brutsaert.

Several models other than those mentioned above have been proposed. They are based on statistical fits between measurements of the infrared radiation and the screen level parameters at the site.

Most of the purely empirical or semi-empirical models can not be expected to perform well without local calibrations. This is due to the difference in geography and climatology of the site. In addition, some of the previous models were developed from daily or long-term averages and therefore are usually much less accurate at shorter intervals. Different instruments (e.g. different wavelength of response and different FOV) used by the investigators can be a possible cause of diversity. At any rate, verifications of the local performance of different models are still necessary to allow for locality differences. Assessments and comparisons for the suitability of some of the existing models have been conducted (see for example Ase and Idso (1978), Zapadka and Wozniak (2000), Niemela Raisanen and Savijarvi (2001), Guest (1998), Key *et al*. (1996), and Duarte, Dias and Maggiotto (2006)). Calibration and adjustments to the constants of some of the existing models were obtained for specific locations and purposes (Garcia 2004), Sridhar and Elliot (2002) Buckley *et al* (1998).

In this project, comparisons between the performances of some of the clear sky models and data collected will be carried out. At the same time these models will be assessed against a model proposed in this study (see chapter 4, 8 and 9).

2.7.2.2 Zenith Angle Distribution

Generally speaking the atmosphere is semi-transparent and it is 'thinnest' and coldest when viewed vertically. It progressively thickens as the viewing angle increases from the zenith, until its emission is close to blackbody emission at the ground temperature at low elevations. This has been confirmed experimentally in the literature see for example Buckley *et al*. (1998), Chadwick *et al.* (1999) and Berger and Bathiebo (2003).

Bell *et al*. (1960) investigated the spectral radiance of clear sky in the infrared spectrum and its changes with elevation angle. Their results showed that at lower angles the

atmosphere is very thick and the radiance is nearly as a blackbody. As the elevation angle is increased, the path length through the atmosphere is decreased. They found that at those wavelengths where the absorption is low the emissivity becomes low. However, in the 6.3-μm water vapor band and the 15 μm CO_2 band, absorption is so high that even over a short path length the emissivity is essentially equal to unity, and the system remains a blackbody. Deacon (1970) used Dines and Dines (1927) data to investigate this relation. He found that an increase of the amount of water vapor in the line of sight appreciably increases the sky radiation. Unsworth and Monteth (1975) have tested this experimentally and succeeded in explaining the cause of these variations. They deduced a formula that describes the variation of the sky emissivity with the zenith angle and the optical water vapor path. This is

$$\varepsilon(\theta) = a + b\ln(u \times sec\,\theta) \qquad (2.50)$$

where u is the precipitable water in cm, a and b are constants, θ is the zenith angle.
Martin and Berdhal (1984) showed that the measured spectral and angular distribution of sky radiation emissivities can be reliably estimated from knowledge of total sky emissivity using an empirical sky emissivity equation. According to them the spectral and angular sky emissivity $\varepsilon_{sky}(\lambda,\theta)$ can be calculated from the following:

$$\varepsilon_{Sky}(\lambda,\theta) = (1-(1-\varepsilon_{sky})[\frac{t(\lambda)}{t_{av}}] \times \exp b(1.7 - \frac{1}{\cos\theta}) \qquad (2.51)$$

Where ε_{sky} is the total sky emissivity, θ is the zenith angle, the factor $t(\lambda)/t_{av}$ is a factor implicitly dependant on the total sky emissivity ε_{sky} and can be determined experimentally (see Martin and Berdhal (1984) for further details on this topic).
The zenith angle distribution of the clear sky will be further investigated in this study both experimentally and theoretically. This will be the topic of chapter five.

2.7.2.3 Overcast and Partly Overcast Models

When the sky is cloudy, radiation from clouds must be considered in the heat exchange between surface and the atmosphere. As previously mentioned, in the presence of cloud the effective radiation and downward atmospheric radiation values undergo

considerable changes. The former decreases and the latter increases, which is accounted for by the fact that clouds are powerful sources of thermal radiation. Paltridge (1970) tried to correlate the increase in infrared radiation coming from the sky with a cloud cover index by analysing a set of data recorded in Aspendale, Australia. He found that any 1/10 increase in the cloud cover index corresponds to a mean increase of 0.6 mW cm^{-2} in the long-wave radiation flux.

The radiation received from the atmosphere is different for different parts of the sky. The effective net outgoing radiation is greatest in the direction of the zenith and least in the direction of the horizon. Clouds that are at the zenith will obscure the coldest portion of the sky and have larger effects than clouds near the horizon. Therefore, the effect of clouds will be greatest in reducing the net radiation when they are near zenith.

Beside the amount of cloud cover present, the altitude of the base of the clouds will have an effect on the net radiation too. Less radiation is received from cold clouds at high altitudes than from warm clouds at low altitudes. A particular cloud type is normally present only within a particular range of altitude. For example, cirrus clouds are always found at high altitude (8-12 km) while stratus clouds are always found at low altitude (1.5-3 km).

The theoretical treatments of the influence of cloud on both effective and downward radiations are found in many articles e.g. Kondratyev (1959), Paltridge and Platt (1976) and Goody (1964).

To account for the effect of the clouds in the atmospheric radiation, the basic method used by the previous investigators is to apply an empirical correction to their clear sky estimates. The general form of this correction (Sellers 1965, Monteith 1973, Geiger 1961) is:

$$L\downarrow = L\downarrow_c (1 + k n^x) \qquad (2.52)$$

Where $L\downarrow$ (W/m^2) is the downward atmospheric radiation from clear and partly cloudy sky, $L\downarrow_c$ (W/m^2) is the clear sky radiation, k is an empirical constant depend on cloud type and elevation and needs to be determined from observations. A list of the values of k can be found for example in Geiger (1965), Kondratyev(1965) and Sellers(1965). The cloud types corresponding to the low, medium and high level along with the values of k obtained by (Oke 1987) are summarized in table (2.4).

The factor n is the fraction of the sky covered in cloud, expressed in tenths from zero to unity (e.g. n = 1 for overcast skies, $n=0$ clear skies) and the exponent x is also an empirical constant.

Different empirical relationships have been developed to relate the atmospheric radiation with a cloud cover index.

Marshunova (1966) used a cloud factor that includes the fractional cloud cover and a coefficient to parameterize the IR downward radiation in the Arctic:

$$L\downarrow = L\downarrow_c (1 + kn) \qquad (2.53)$$

She found that the values of the coefficient, k, exhibits a seasonal variation with extreme values ranging from 0.16 in summer to 0.31 in winter.

NOTE: This table is included on page 44 of the print copy of the thesis held in the University of Adelaide Library.

Table 2. 4: Values of the k factor found in equation 2.52 to compensate for the effect of clouds on long ave radiation in the atmosphere for different cloud types. (Oke 1987).

Budyko(1974) suggested a different cloud factor, showing that the increase in the flux was a power law (n^y) of the cloud amount. Boltz (1949) varied *k* according to the cloud type and used for *y* a value of 2. This type of cloud factor may be more accurate when the cloud type is known, although cloud type is subjective:

$$L\downarrow = L\downarrow_c (1 + kn^2) \qquad (2.54)$$

Maykut and Church (1973), used year round data collected from Alaska to arrive at values for *k* and *y* of 0.223 and 2.75 and their model was:

$$L\downarrow = L\downarrow_c (1 + 0.2\ 2n^{2.75}) \qquad (2.55)$$

Zillman (1972) treated the cloud effect a different way. The cloud factor is considered a function of both fractional cloud cover and the near surface temperature. Zillman developed his equation using data from the southern ocean and it has been used by Pease (1975) in an Antarctic sea ice modelling experiment. The Zillman's equation was:

$$L\downarrow = L\downarrow_c \sigma T^4\ 0.9\ 6\ (1 - 9.2 \times 10^{-6}\ T^2)n \qquad (2.56)$$

The above equations are written for use with a single layer clouds only. No schemes were developed for using them when more than one cloud layer was present. Just as the net radiation can be modified for cloudy skies, it can also be modified for situations when there is more than one cloud layer present. However, a method is described by Kondrat'yev (1969) to take into accounts the effects of clouds at different altitudes. This summaries as:

$$L\downarrow = L\downarrow_c [1 + (c_l n_l + c_m n_m + c_h n_h)] \quad (2.57)$$

In this relationship n_l, n_m and n_h are the total opaque sky covers for low, medium and high level cloud respectively. The coefficients c_l, c_m and c_h describe the effect of low, medium and high clouds on the net radiation.

The values for these coefficients are empirical and must be found experimentally.

Kimball *et al*. (1982) showed that the total predicted atmospheric radiation is:

$$L\downarrow = L\downarrow_c + \sum_i^n \tau_8 A_i \varepsilon_i f_{8i} \sigma T_{ci} \quad (2.58)$$

Where n varies from zero for cloudless sky to 4 (for the maximum-cloud layer observed); $\tau_8 = 1 - \varepsilon_8$ is the transmissivity of the atmosphere in the 8-13 μm window, A_i is the fraction of the sky covered by the *i*th cloud layer, ε_i is the *i*th cloud emissivity, f_{8i} is the fraction of black body radiation emitted in the 8 μm -13 μm band and T_{ci} is the *i*th cloud temperature in K.

None of these equations and the methods mentioned above treats adequately the effects of variable cloud base height, cloud thickness or cloud water phase. Their accuracy is therefore likely to be limited, particularly for estimating fluxes over short time scales. There are some further parameterizations for atmospheric radiation that deserve mention. Schmetz *et al*. (1986) showed that the all sky IR radiation modelling consists of parameterization for the clear sky flux plus a parameterization for the cloud contribution as:

$$L\downarrow = L\downarrow_c + (1 - \varepsilon_o) k \varepsilon_c \sigma T_o^4 \exp[(T_B + T_o)/46] \quad (2.59)$$

Where ε_o is the clear sky emissivity, ε_c is the cloud emissivity. T_o is the near-surface air temperature, and T_B is the cloud base temperature. This scheme performs well under both winter and summer conditions and for a wide range of atmospheric emissivities.

In studying overcast skies using one year of night-time data collected under Mediterranean-like conditions, Riordan *et al.* (2005) (see chapter 7) proposed a model similar to that of Schmetz *et al*. (1986). The atmospheric radiation for *overcast skies* (in their model represented by sky temperatures) can be calculated from:

$$\sigma T_{sky}^4 = \varepsilon_{cloud}\sigma T_{cloud}^4 + \varepsilon_{ground}\sigma T_{ground}^4 (1-\varepsilon_{cloud}) \quad (2.\ 60)$$

Where T_{sky} is the measured sky temperature, ε_{cloud} is the cloud emissivity; ε_{ground} is the ground emissivity and T_{ground} is the screen level temperature. All the temperatures in this model are in K.

In chapter (7) the sky temperature from overcast skies will be studied using the same instrument used by Riordan *et al.* with data collected for more than four years. This investigation will include the parameterizations of the overcast sky temperature and a test of the proposed clear sky models in discriminating cloudy skies.

CHAPTER THREE

INSTRUMENTATION AND METHODS

3.1 Introduction

The University of Adelaide has developed simple single pixel thermopile IR cloud detectors for monitoring clouds over astronomical sites. Those detectors were developed with 3^o and 90^o fields of view (FOV) and have a broad spectral response extended from 5.5 μm to above 20 μm centred on a wavelength of 10 μm.

This project is largely based on data collected from these detectors. The data collected and used in this project have come from different sites, different modes of operation, different filters, and different fields of view.

This chapter aims to give a detailed description of these detectors and the methodology followed to construct them and analyse the collected data. The chapter starts by

introducing the techniques of detecting clouds using the IR method. The principles of the thermopile sensors as radiation detectors will be detailed in section (3.3).
The concepts of constructing the cloud monitors will be discussed in section (3.4). This includes a description of the instruments, the mechanical design, the characteristics and electronic properties. The procedure for calibrating these monitors will be illustrated in section (3.5). This calibration was one of the important tasks of this project. Hence, it was intended to produce detectors with optimum performance and high sensitivity to detect clouds in various circumstances. Some illustrative results from different cloud detectors will be presented in section (3.6). A summary of the database and a brief outline of the methodology used throughout this project will be given in sections (3.7) and (3.8) respectively. The chapter will end by giving comments and notes about some issues related to these detectors.

3.2 Detecting Clouds in the IR

Clouds are highly variable and exhibit a wide range of spatial extents and lifetime scales. They vary in their heights, temperatures, densities and constituents. The cloud cover must be continuously observed by some method to determine its nature and, when needed, for astronomical and atmospheric applications. For astronomical and astrophysical observatories, as is the case for cosmic ray sites, a continuously operating automated system requiring little attention is needed, as the sites will operate without on-site personnel for much of the time Abu-Zayyad *et al.* 1999, and Clay *et al*. 2001.
Clouds may be detected in a number of ways. Radar, laser reflection, and attenuation of starlight are all examples of methods that have been used to detect the presence of clouds (Bird 1996). Recently, infrared techniques have been used for cloud detection above astronomical observatories (e.g. Ashley and Jurcevic 1991, Bird *et al*. 1995, Chadwick *et al.* 1999 and Buckley *et al*. 1999).

Assuming that a cloud represents a grey body at terrestrial temperatures ~ 300 K, Wien's Law (Eq. 2.3) implies that it will radiate with maximum intensity at a wavelength ~10 μm, in the IR part of the spectrum. It follows then that an IR cloud monitor can be used in theory to detect cloud.

Sloan, Shaw and Williams (1955) provided data, which show that infrared measurements of the sky at wavelengths between 8 μm and 14 μm (the atmospheric window) are sensitive to the presence of clouds. The presence of clouds produces an enhanced signal above that from clear sky. The amount of contrast between clear sky and cloudy sky depends on the wavelength band selected, the optical and intrinsic properties of the cloud and the intensity of emission from clear sky.

Chadwick *et al.* (1999) and Buckley *et al.* (1999) used a mid-infra red (MIR) radiometer operating at wavelengths between 8 μm and 14 μm to sense the temperature of the sky as a measure of the presence of clouds in the FOV of the atmospheric Cerenkov telescopes at different sites.

3.3 IR Thermopile cloud Detector

3.3.1 Thermocouple

A thermopile is a serially interconnected array of thermocouples, each of which consists of two dissimilar materials (figure 3.1). A thermocouple is a device that makes use of the voltages developed by a junction of two dissimilar metals to measure a temperature. They work via the Seebeck effect, which is that the voltage developed between the two junctions is proportional to the temperature difference between those two points. For an ideal thermocouple the potential difference (ΔV in μV) may be written as a function of the temperature change (ΔT in K) such that:

$$\Delta \mathrm{V} = S_{AB}(T)\Delta T \qquad (3.1)$$

Here S_{AB} is the relative Seebeck coefficient, expressed in μv/K. (Coté 1996). This coefficient depends not only on the temperature, but also on the intrinsic properties of the two metals, such as the conduction, electron density and mobility.

The detailed mathematical explanation of the thermocouple effect is complex and involves electron quantum theory. However, the fundamental concept is straightforward. Two different materials have different Fermi levels i.e. different electron densities, while they are both at the same temperature. When one end of a

conductive material is heated to a temperature larger than the opposite end, the electrons at the hot end are more thermally energized than electrons at the cooler end. These more energetic electrons will migrate (diffuse) to the cooler end in order to establish a new equilibrium of the junctions and balance the charge difference. This move disturbs the individual equilibrium of each of the materials and leaves exposed positive charges on one side of the junction and an excess of negative charges on the other side. Thus, this redistribution of electrons creates negative charges at the cool end and an equal positive charge at the other end.

Consequently, this heating of the end causes an electrostatic voltage to be formed across the junctions. Since the temperature determines how energetic the free electrons will be and since their migration determines how many exposed positive and excess negative charges are on the two sides of the junctions, it follows that the magnitude of the (Seebeck potential) electric field is a function of temperature (Weckmann 1997).

In order to increase the output voltage, several junction pairs may be connected in series. The responsivty and sensivity, is then increased by a factor of *n*. If *n* is the number of thermocouple junction pairs placed in series then 3.1 yields:

$$\Delta V = n \times S(T) \Delta T \qquad (3.2)$$

Such a device called a thermopile. As shown in fig (3.1), elements of a series of thermocouples of alternate materials A and B are placed between the heat source and a heat sink. The hot junction comes into thermal equilibrium with the high temperature surroundings producing an electromagnetic field at the leads. If a current flow results, thermal energy is converted into electrical energy. The remaining energy absorbed at the hot junction is rejected to the heat sink at the cold junction

Figure 3. 1: Example of Thermopile. Adapted from Weckmann1997

3.3.2 Principle of Radiation Detection Using Thermopile Detectors

In infrared radiation measurements using thermopiles, the active or "hot" junctions of the detector are blackened to absorb radiation (called the absorber), while the reference, or "cold" junctions are maintained at the ambient temperature of the detector. Typically, the cold junctions are placed on a silicon substrate to provide heat sinking while the hot junctions are formed over a thin diaphragm that effectively thermally isolates the hot junction from the cold junctions, figure (3.2). The absorption of IR radiation, by the blackened area, causes a change in the in the temperature of the hot junctions. This difference in temperature between the active and reference (cold) junctions is translated into an output voltage depending on the intensity of the incident radiation through the Seebeck effect.

Figure 3.2: Illustrates the physical design of thermopile sensor and its main components. Adapted from Lee 2001.

The output of a radiation thermopile is a function of the temperature difference of the object in question and the sensor. It is essential for calculation of the object's temperature to know the temperature of the cold junction in the sensor, which in most cases is identical with the ambient temperature, and to correct the measured value. This procedure is called *temperature compensation*. In this case the thermopile requires either reference junction temperature measurements or a constant temperature sink for its reference junction. The latter is usually difficult to implement in an instrument because of size and weight requirements.

In most thermopiles used nowadays a *thermistor* is coupled to the sensor reference junction and allows one to determine the absolute temperature of the sensor, hence thermopile signals represent a temperature of the object with respect to the ambient temperature. Then the temperatures of the thermopile and the sensor just have to be added.

Thermopiles, as a remote tool for temperature measurements, have shown some unique properties, which cannot be duplicated by other temperature sensors. For example they have an inherently stable response to DC radiation; they respond to a broad infrared spectrum and do not require any source of bias voltage or current. The application of thin film technology allows the production of a thermopile with 1000 thermocouple junctions in an area less than a 1 mm2, with better performance and less cost than

traditional sensors. For more details of thermopile characteristics see the Perkin Optoelectronic website[1] .

Thermopile sensors have been employed in some precision applications and have been used heavily due to their long-term stability and a very low temperature coefficient of sensivity. In thermopile packages an optical filter is often included in the assembly to exclude short wave IR and visible light. For special applications thermopiles are available with either narrow or broadband transmittance.

3.3.3 Theoretical Consideration

The total radiation power P_{obj} per unit area emitted by an object of temperature T_{obj} can be expressed as (Schilz 2000):

$$P_{obj} = \sigma . \varepsilon_{obj} . T_{obj}^{4} \quad (3.3)$$

Where σ is the Stefan-Boltzmann constant = 5.668 x 10^{-8} $Wm^{-2}K^{-4}$, and ε_{obj} is the emissivity of the object in question. In the ideal case, for a perfect blackbody, ε has the value of 1 and for most non-metallic substances ε ranges between 0.85-0.99 for wavelengths centred on 10 μm. The thermopile itself emits heat energy following:

$$P_{a} = \sigma . \varepsilon_{sens} . T_{a}^{4} \quad (3.4)$$

Where T_a is the sensor temperature, which is in most cases is equal to the ambient, ε_{sens} is emissivity of the thermopile itself. For simplicity, in theoretical considerations, we shall assume both the object and the sensor emissivites equal 1. The relation between the power received by the thermopile to the temperature of the object and the temperature of the instrument itself is called the heat-balance equation and can be expressed as:

$$Power = K'(T_{obj}^{4} - T_{a}^{4}) \quad (3.5)$$

[1] http://www.perkinelmer.com

K' is the instrument constant which contains σ and detector properties such as the properties of the optical system of the thermopile. The thermopile produces a voltage proportional to this received power. The proportionality constant is called the sensitivity *S*. Sensitivity connects the voltage output of the sensor to the absorbed radiation and is expressed as:

$$V = Power.S \tag{3. 6}$$

Where *V* is the output voltage from the thermopile (in V), and the unit of S is V/W.
The sensivity is the most important parameter for thermopile characterization. Typical sensivity values of a thermopile are several 10s to about 100 V/W depending on the area of the absorber and the number of the thermocouples.
Therefore from equations (3.5) and (3.6), the output voltages from the thermopile can be written as:

$$V = k(T_{obj}{}^4 - T_a{}^4) \tag{3. 7}$$

where the new constant *k* includes the older constant K' and proportionality constant. This equation tells us that the output voltage is a function of the object and ambient temperatures. For a fixed ambient temperature, the output voltage of the thermopile increases with the fourth power of the object temperature, $T_{obj}{}^4$. Figure (3.3) shows the theoretical characteristic curve of the thermopile output as a function of object temperatures at fixed ambient for the output voltages at different target temperatures. Over a wide range of temperatures this relation is not linear. As seen from equation 3.7 the output signal will also vary when the ambient temperature changes. In real temperature measurements this effect needs to be compensated for. Equation 3.7 has a real physical basis and will be used as the basis of the detector calibrations discussed in the next sections.

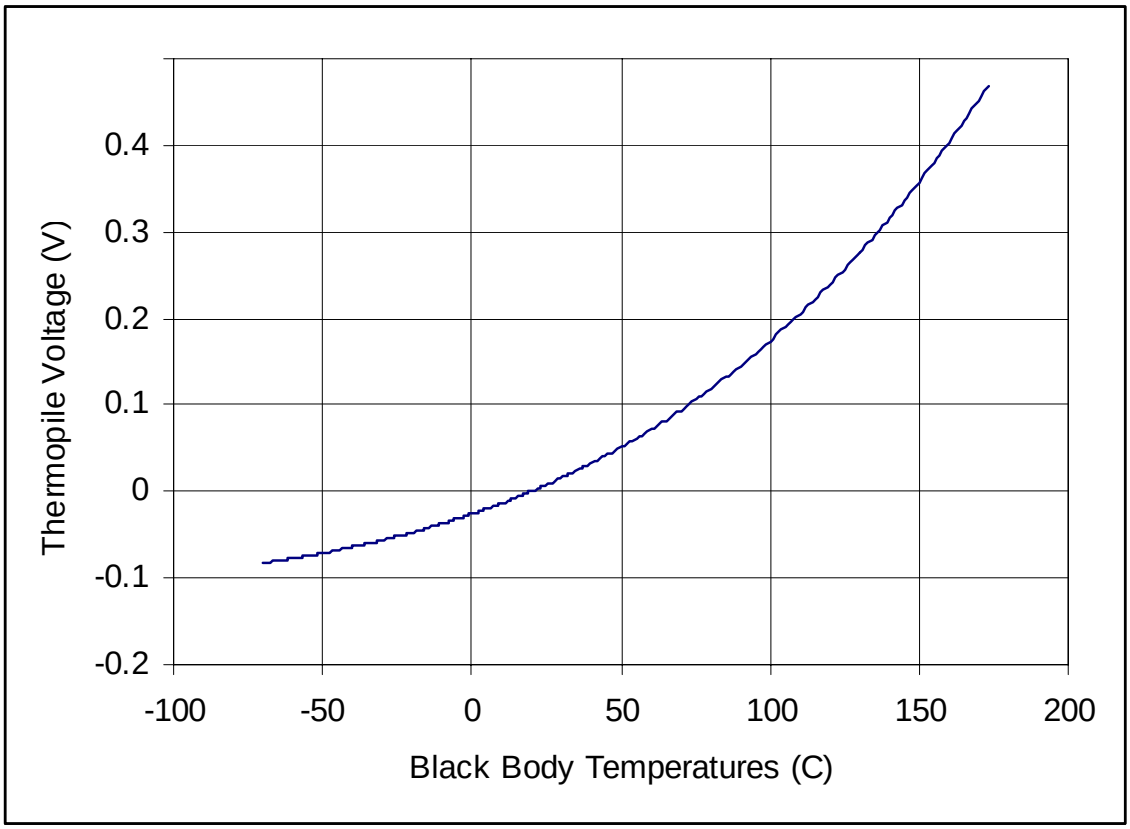

Figure 3. 3: Shows the theoretical characteristic curve of the thermopile output voltages at different target temperatures at an ambient of 20 ^{o}C.

3.4 The Detector

3.4.1 Description of the Detector and its Characteristics

The idea of building a cloud detector using an infrared technique was described by Ashley and Jurcevic (1991). They used an infrared pyroelectric element as an IR detector. Instead, we developed a detector based on commercial IR thermopile sensors (EG&G Heimann TPS 534). They have similar sensitivity to the pyroelectric detectors but will retain an output voltage proportional to the temperature difference between the field of view and a local reference within the detector canister. Unlike the pyroelectric detectors thermopile detectors require no mechanical chopping and draw little current. They have a wide spectral range from 1 µm to beyond 20 µm. The sensors are hermetically sealed into a housing, similar to a standard TO5, with an optical filter (a window) with a 5.5 µm spectral short wave cut-off. The TPS 534 series employs a chip of 1.2 x 1.2 mm^2 absorber size and is fitted with a 30-kΩ thermistor as a temperature

reference. The sensor shows a flat sensitivity characteristic over the wavelengths of interest. It has a large absorber size, high signal output and low temperature coefficient with a resolution of ± 1^{o} and with a sensivity value of 42 V/W. The detector is DC coupled, unlike AC pyroelectric detectors, and hence has a response directly proportional to the incident radiation. The time constant of the thermopile is 35 ms. With our additional circuitry, however, this becomes 100 ms. This time is a measure of the delay between a temperature change and the thermopile response. However, this is not significant for atmospheric applications since the temperature changes over times of the order of minutes. The sensor's specifications and characteristic curves are presented in the TPS 534 data sheet from EG&G Heimann[2].

We have used TPS 534 detectors with standard filters and with G15 filters. The standard (STD) filter has a spectral range from 5.5 µm to above 20µm while the G15 filter has a spectral response ranging from 6.6 µm to above 20 µm, figure (3.4).

[2] http://optoelectronics.perkinelmer.com/content/Datasheets/DTS_TPS534R3.pdf

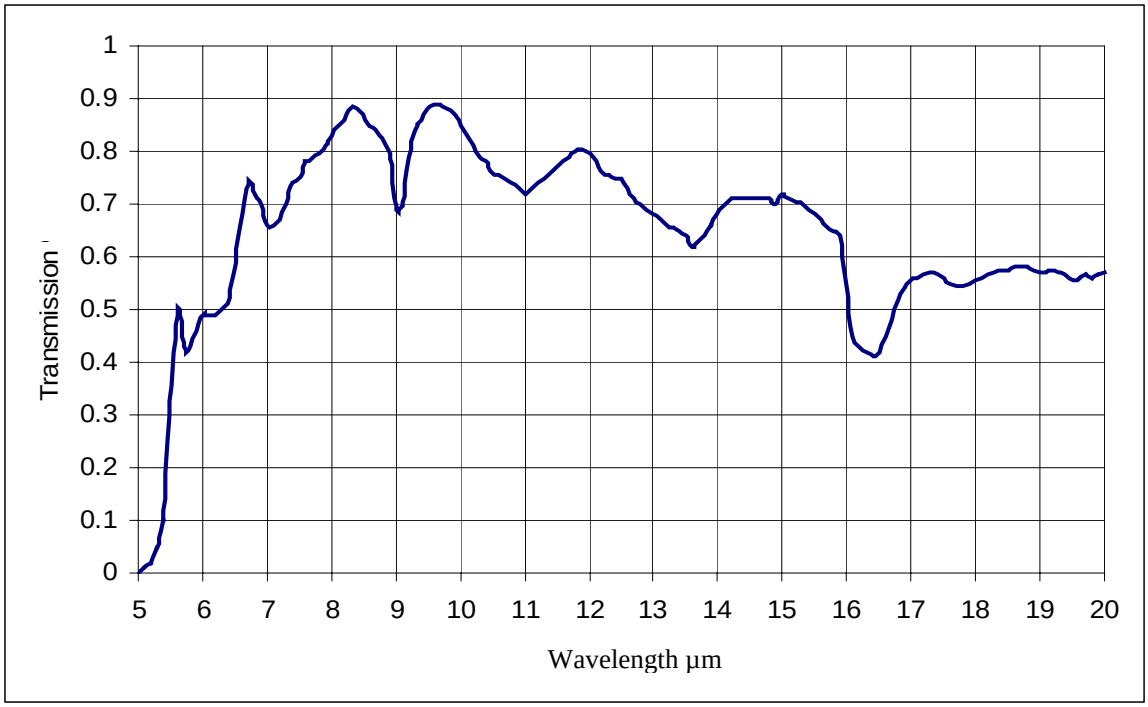

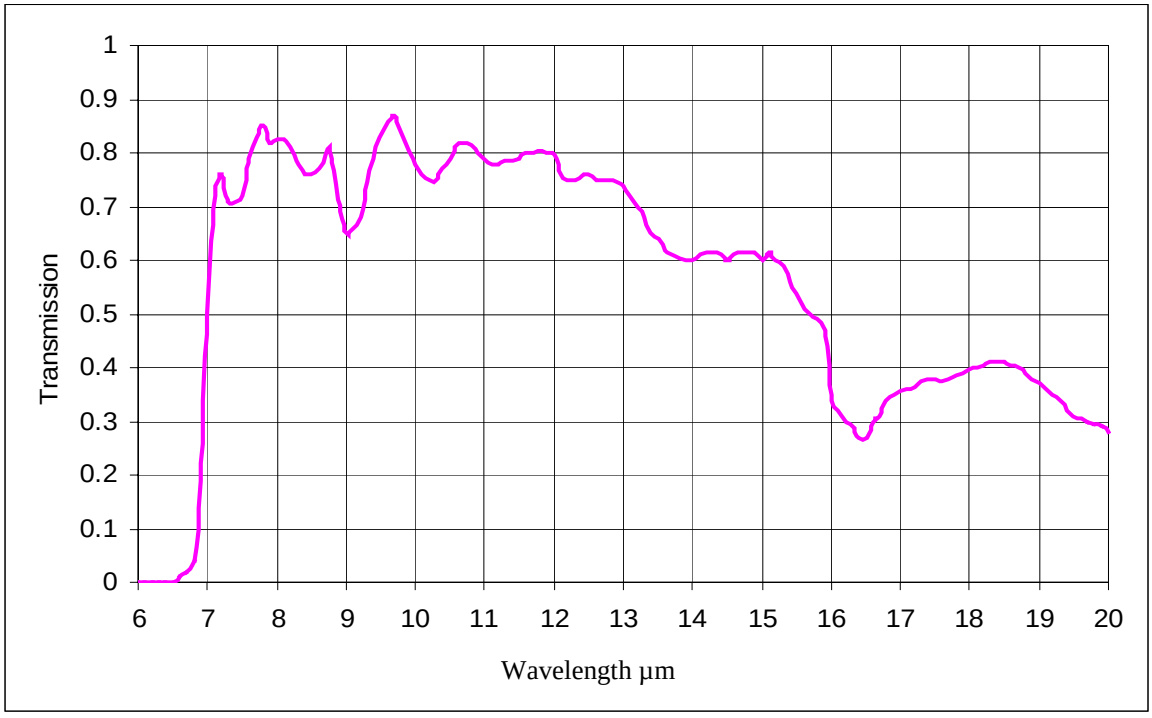

Figure 3. 4: The transmission characteristics curves for STD (above) and G15 (lower) filters.

3.4.2 Physical Design of the Cloud Monitors

The thermopile sensor unit was incorporated in a Printed Circuit Board (PCB), which contained all the required amplification, the electronics of the compensation stage and other filtering circuitry. The entire PCB was mechanically placed in a sealed die-cast box as weather protection.

We have designed detectors with 90^o and 3^o FOV. In the former the end of a collimating tube is covered with an IR transmission polyethylene cover (model 2063 manufactured by KUBE[3], as weather protection. For the latter a Fresnel lens (model PIR1010 manufactured by KUBE) is used.

The materials used to protect the radiometer can have a major effect on the sky temperature measurements. This effect results in attenuating the IR radiation received by the thermopile sensor. Aye *et al* (2003) for example, have shown that different protective materials can significantly influence the measured values of sky radiation by the detector. Figure (3.5) is adapted from their article. At a Durham site and at an angle close to the zenith, 16 ^{o}C in difference was found between the sky temperatures measured using a Clartan window and Polyethylene. These measured temperatures were about – 24^o C for the former and $–40^o$ C for the latter. Similarly in Namibia the measured sky temperature using PVC window was 2 ^{o}C colder than the Clartan window at the zenith.

However, in our case, this attenuation effect has been taken into account and was compensated electronically by employing a higher amplification stage with large gain during the first calibration procedures (zero degree calibration, see below).

Also the protective materials may have a small effect on the spectral response of the filters, especially around 7 μm. This contributes modest extra attenuation to both the sensor and sensor/cover systems but does not significantly affect the cloud monitor's response.

[3] http://www.kube.ch

NOTE: This figure is included on page 59 of the print copy of the thesis held in the University of Adelaide Library.

Figure 3.5 : The relation between sky temperature and elevation angle of the radiometer with different window materials. Ambient conditions in Namibia: nighttime, T = 16 °C, rel.Humidity 41%; Durham: afternoon, T = 5 °C, rel. Humidity (70 ± 10) % . Adapted from Aye et al. (2003)

The exact pass band of the detectors and lens/cover systems were not specified either by the manufacturer of the thermopile or by the manufacturer of the lenses/covers. Therefore it was one task of this project to investigate the upper wavelength range of response of the detection system. This task, and the related results, will be discussed in detail in chapter 6.

3.4.3 Mode of Operation and Data Acquisition

Cloud monitors were placed on the roof of physics building at the University of Adelaide, in four sites in Saudi Arabia and in one site at the Pierre Auger Observatory in Argentina.

In Adelaide, both G15 and STD detectors were placed on the roof of the physics building. They were installed in two different modes. Two detectors with 90° FOV, one STD and one G15, were pointed at *fixed* vertical directions toward the sky. Also, two detectors with 3°, one STD and one G15, were used as *scanning* detectors. They

were placed on a rotator attached to the railing at the side of the roof that allowed us to completely scan the sky from East to the West (from horizon to horizon) through the zenith in 3^o steps every 5 minutes (see figure 3.6). G7 is a new cloud monitor (with a bandwidth between 10.5-11.2 μm centered at 10.9 μm.) installed late 2003 to study the atmospheric emission in the atmospheric window. They are operating in both scanning and fixed modes. G7 detectors were not related to the purpose of this thesis; hence their data will not be used. In Saudi Arabia, four STD detectors were installed at a fixed vertical position with three of them being with 90^o FOV and the fourth with 3^o FOV. One vertical STD detector with 3^o FOV was deployed in 2005 at the Central Laser Facility (CLF) of the Pierre Auger Observatory.

Figure 3. 6: Shows the scanner detector at the roof of the physics department at the University of Adelaide. The figure shows the scanner at different zenith angles. From top left the scanner at the east (toward the hills), at the zenith, west (towards the sea) and finally at 10^o from the zenith toward the west. The picture also shows the configuration of the detectors on the scanner. The three detectors with larger sizes are those with 3^o FOV while those with smaller sizes are those with 90^o FOV. The 3^o and 90^o FOV detector's configuration is from left to right (G7, G15 and STD) detectors. See text for more details

3.4.4 Data Acquisition

The electronics of the detection system was designed to read raw information from the detector channels. The three output voltages from the detector are:

1. Uncompensated output voltage; this is the temperature difference between the detector and the target.
2. Thermistor: due to the temperature of the detector.
3. Compensated: the difference between the uncompensated and the thermistor voltages.

After scaling and converting the measured voltages to pre-scaled temperatures (see next section), the three outputs were then collected via a connection to a computer with an appropriate data logger.

In Adelaide, data were collected via a Multifunction I/O Data Acquisition Card (DAC) from National Instruments[4]. LabView software was used to interface the DAC and acquire the data. The acquired data were then tabulated every 5 minutes and saved in daily files with a total of 288 records of data every day. For every 5 minute scan each record of data has eventually 121 readings from the scanners, and 2 reading from the vertical detectors. The software was programmed to display and plot the recorded data every 5 minutes on the screen. At the four sites in Saudi Arabia XR5-8-A-SE data loggers manufactured by Pace Scientific[5] were used. At the CLF site data were logged by the on-site data acquisition system.

3.5 Thermopile Module

3.5.1 Design Concept and the Electronics

The concepts of designing and developing the IR thermopile monitors can be summarized as following:

1. The signal generated by the thermopile chip needs to be amplified using an adjustable low noise amplifier.
2. Signals from the temperature reference sensor (*thermistor*) require an electronics processing stage.
3. Combine the thermopile voltage with the thermistor to compensate for ambient temperature variations.
4. Scale the voltages to a fixed calibration scheme.

The circuitry of the detector described in Clay *et al.* (1998) is shown schematically in figure 3.7. The module has four main sections: A thermopile chip, ambient temperature sensor, amplifiers, voltage reference (not shown here) and a final output stage.

[4] http://www.ni.com/dataacquisition/
[5] www.omniinstruments.com.au/aquisition

The module works as follows. The voltage generated by the thermopile is amplified by a factor of 100, by using the first operational amplifier (OP) U1. This OP is physically located behind the thermopile to minimize noise pick-up. Then, the amplified signal is amplified by an additional factor, approximately 15, by a second OP U2D. This factor depends on the required scaling scheme for the desired final output voltage of the detector. The adjusted output signals are then inverted using the U3A amplifier, which has a gain of –1, to get the final uncompensated output voltage. The output from the thermistor is calibrated to give 25 mV/^{o}C, which is then amplified using U3C by a factor of 2. Finally an analogue processor is employed for ambient temperature compensation. Here, a voltage signal is generated from the thermistor is added to the thermopile voltage by means of another (OP) U3B.
The resulting voltage at the output of that stage is then:

$$V_{comp} = (V \times A_1 \times A_2) + \{V_{ther} \times A_3\} \qquad (3.8)$$

A_1, A_2, and A_3 are the gains of the operational amplifiers U1, U2D and U3C respectively. V is the uncompensated output voltage given by equation 3.7; V_{Thr} is the thermistor output voltage.

This equation can be simplified to:

$$V_{comp} = V + V_{ther} \qquad (3.9)$$

The last two equations are considered as the basis of calibrating the detector's output.

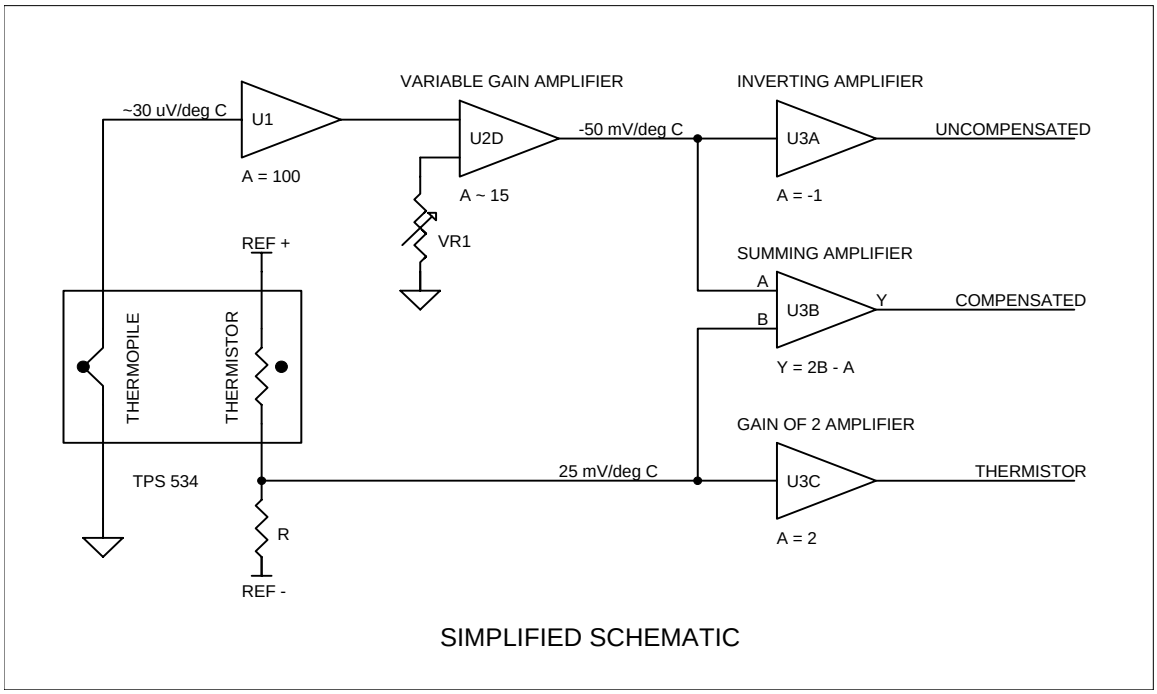

Figure 3. 7: Schematic diagram of the detector module. It shows the main components of the detector, and the outputs.

3.5.2 Zero Degree Calibration

The aim of this calibration is to set a scaling factor between the output voltage and the measured temperature of the object and to linearize the relation between these two parameters (see equation 3.7 and figure 3.3) over a preferred range of temperatures. The scaling factor of the detector outputs was adjusted electronically and set to 50mV/ ^{o}C. The procedure of setting this factor is as follows.

The first step before doing the calibration was adjusting the **thermistor** output to a fixed conversion factor.

The thermistor resistance has a non-linear resistance to temperature characteristic, as shown here (Phillips Handbook 1989):

$$\frac{1}{T} = \frac{1}{T_0} + \frac{1}{\beta} ln\left(\frac{R_T}{R_0}\right) \qquad (3.\ 10)$$

Where R_T is the resistance at temperature T (in ^{o}C), R_o is the resistance at a reference temperature T_o (at 25 ^{o}C = 30.000Ω for TPS534), and β is a constant, (characteristics of the material) has a value of 3800 for the TPS 534 . Equation (3.10) becomes:

$$R_T = \frac{30000}{e^{\left(\frac{3800}{25+273} - \frac{3800}{T+273}\right)}} \quad (3.11)$$

Figure (3.8) is a plot of the thermistor resistance versus temperature. In order to linearize the relationship between the resistance and temperature, a resistance was connected in series with the thermistor. The linearizing circuit (voltage divider) can be also used to plot the $R/(R+R_T)$ for different values of resistance see figure (3.7). We can see that with 30 kΩ we get a quite linear response from about 0 to 35 ^oC. This is ideal for the expected range of operating temperatures. The equation of the straight line fitted to this curve is:

$$A = 0.0106\,T + 0.2343 \quad (3.12)$$

where A is the ratio $R/(R+R_T)$ and T is the thermistor temperature in ^oC. This equation has a slope of 0.0106/T. The voltage across R = A (REF^+ -REF^-) which needs to have a slope of 0.025 V/T. Therefore (REF^+ -REF) needs to have a slope of 0.025/0.0106 = 2.3585. By adjusting the voltage precisely across REF^+ and REF^- we get a thermistor output of 25 mV/^{o}C. This voltage is then amplified by a factor of 2 by the U3C OP to get the thermistor-measured voltage scaling factor of 50 mV/^{o}C. This scaling for the thermistor output is useful in calibrating the thermopile output because it is based on the thermistor and thermopile specifications provided by the manufacturer.

Having the thermistor output pre-scaled, according to equations (3.8) or (3.9), the thermopile output has to be added to compensate for the temperature variations. This additionally generated voltage must be equivalent to that voltage originally delivered by the thermopile if working at a fixed reference temperature and sensing an object at an ambient temperature. This was done as follows.

The detector was exposed to a block of ice at 273 K (0 ^oC), with a target-detector distance resulting in the ice filling the FOV. For our calibration we require that a target temperature of 0^{o}C give zero volts at the compensated output V_{comp}. By doing this, the sum of equation 3.8 or 3.9 is equal to zero i.e. $V_{comp} = 0$. Equation 3.9 then becomes,

$$V = V_{ther} \quad (3.13)$$

Then we varied the variable resistor to adjust the gain of U2D to have uncompensated output of 50 mV/^{o}C. This adjusted uncompensated output factor is the same as the thermistor scaling factor. In this case we get the desired compensated output voltages, and all what we need to do then is to covert the measured voltages to temperatures using a factor of 20 ^{o}C/V.

This calibration is called *zero degree calibration*. It is used to linearise the Voltage-Temperature curve over a range of sky temperatures.

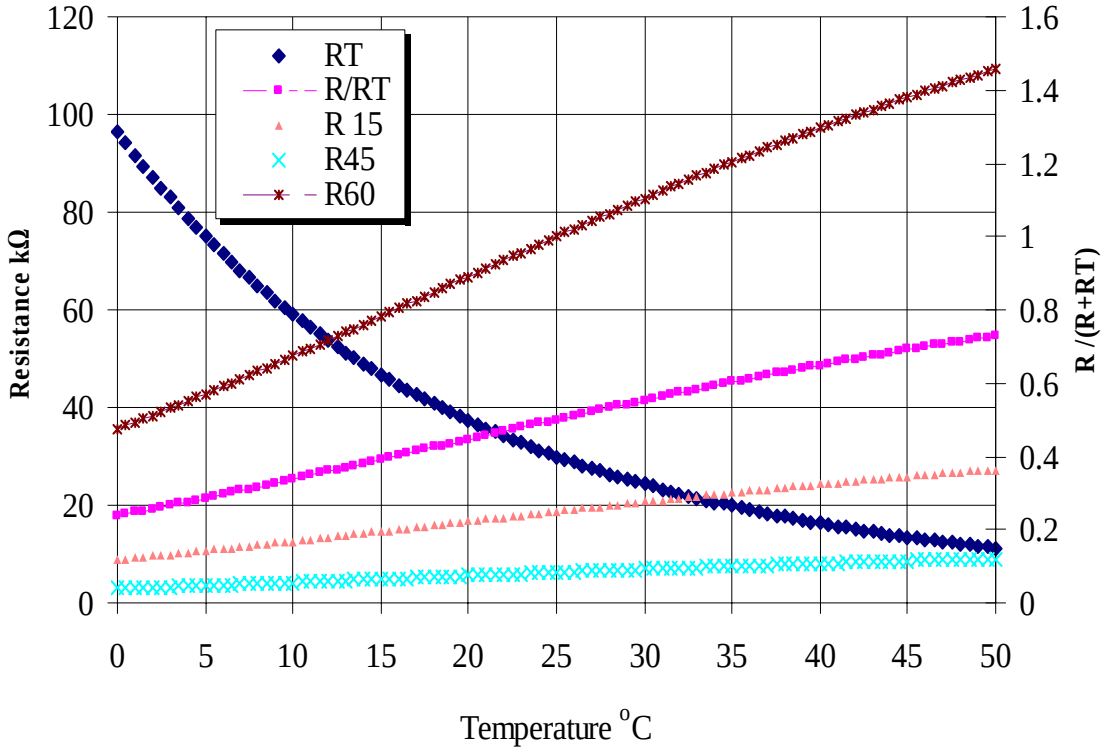

Figure 3. 8: Shows the Temperature versus resistance relationship equation (3.11) for different temperatures represented by RT in the graph . It also shows the R/(R+RT) plot against temperatures for different values of resistance, R30, R15, R45, and R60 are the resistance values of 30 kΩ, 15 kΩ, 45 kΩ, and 60 kΩ respectively.

3.5.3 Absolute Calibration

The scaling factor of the detector output of 50 mV/^{o}C was a good approximation over a substantial range of sky temperatures. However, for colder sky temperatures, such as those exhibited by clear skies, this scaling needs to be modified to give accurate sky temperature measurements. This is because the output of the thermopile is not really

linear over a wide range of source temperatures as we saw before (figure 3.3). One objective of the absolute calibration was to develop a technique for determining the sensor output if the range of temperatures extended beyond the linear 50mV/^{o}C-calibration scale.

Blackbody calibration is commonly utilized in instruments using IR techniques for remote temperature measurements. It is usually achieved by using a well-calibrated referenced black body in order to give a precise temperature output, Albercht and Cox (1977) and Philiopona *et al*. (2001).

A blackbody (BB) was built in the laboratory for the purpose of these calibrations. The BB was a blackend round aluminium plate about 8 cm thick and 23 cm in diameter. A temperature sensor was embedded within the plate. The plate was held on a retort stand at the edge of the bench and the detectors were placed a distance of approximately 10 cm from the plate so the entire FOV was filled. The set up of the experiment is shown in figure (3.9). The plate was cooled using 4 litres of liquid nitrogen to a temperature lower than –50 ^{o}C. As it subsequently warmed over time, temperature measurements from the plate and the three output voltages from each sensor were recorded. A reading was taken approximately every 5-10 minutes, over a whole day, until the plate temperature reached the ambient temperature. Fig (3.10) is an example of the three output voltages from one of the detectors during the calibration procedure. The curve shows that the calibration exercises have covered a wide range of cold temperatures, which is more desirable when measuring clear skies that exhibit such temperatures. The graph also shows the stability of the measurements throughout the whole experiment.

The duration of taking each measurement was limited to less than 15 seconds. This was to avoid any saturation of the sensor's elements by the close distance to the plate. Any ice was scraped off from the plate's surface before each measurement was taken. This was to ensure that the reading was taken from the plate itself rather than from the ice, which may have a different emissivity to the plate, which is assumed to be 1. This calibration exercise was carried out for all the sensors used in this project.

From these data, a calibration curve was produced for each filter and FOV. These curves relate the plate temperature of the black body and the detector temperature output based on an assumed 50 mV/^{o}C calibration.

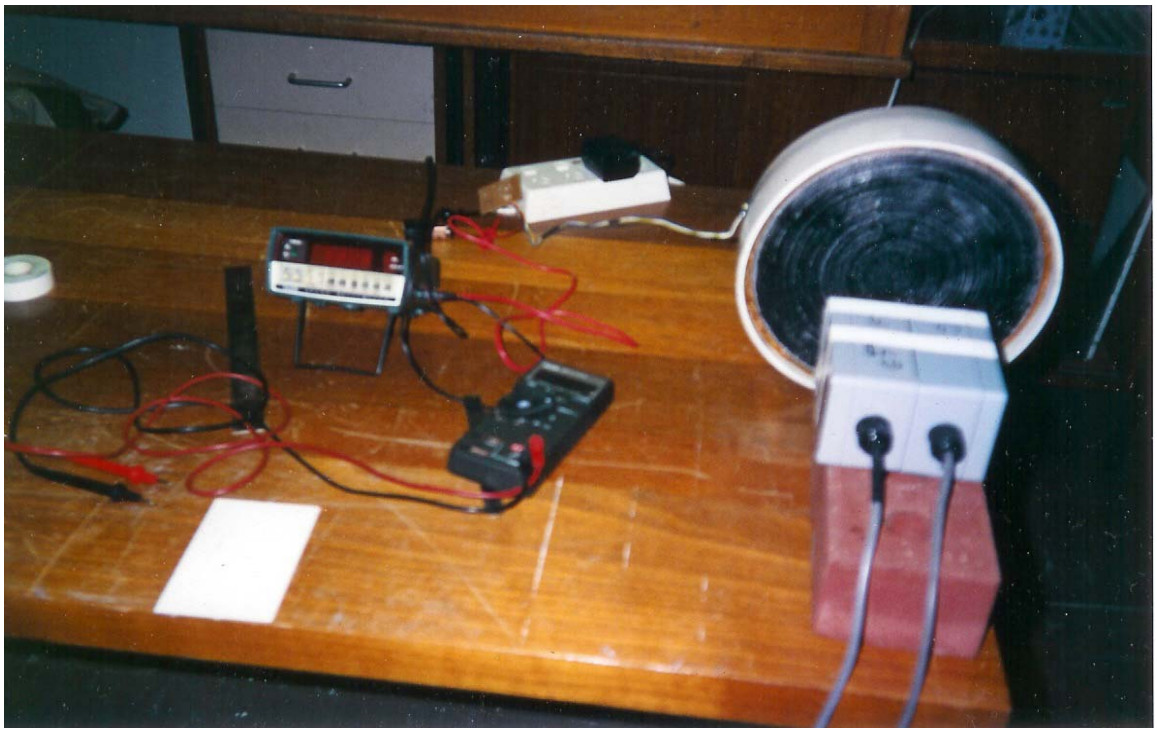

Figure 3. 9: Set-up of the experiment for calibrating the cloud monitors used in this project.

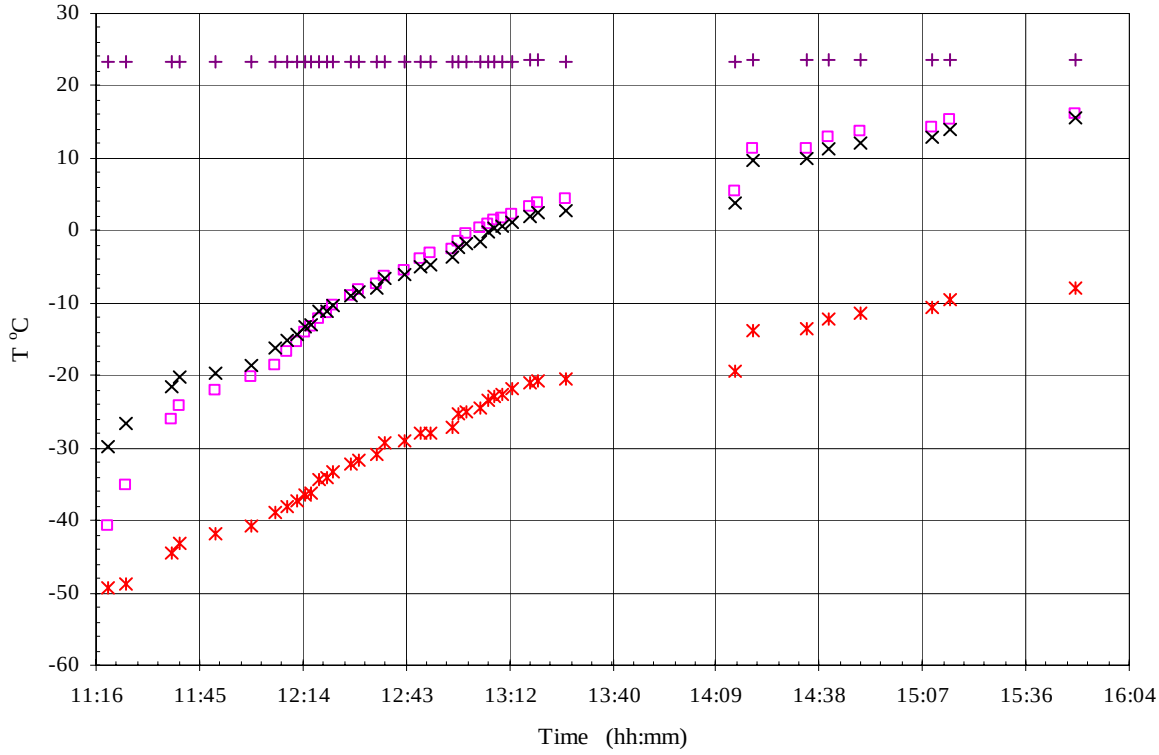

*Figure 3. 10: Example of the three outputs voltages from G15 detector with 3° FOV detector in addition to that from the black body during the calibration procedures. The output voltages are scaled to temperature with a conversion factor of 20 °C /volt. The □ is the black body temperature, +, □ and * are the outputs from the thermistor, compensated and uncompensated temperatures respectively.*

A second-degree polynomial fit was applied to each curve between the detector temperatures and the real BB temperatures. This was carried out for STD filters with 3^o and 90^o FOV figure (3.11) and for G15 filters with 3^o and 90^o FOV figure (3.12).

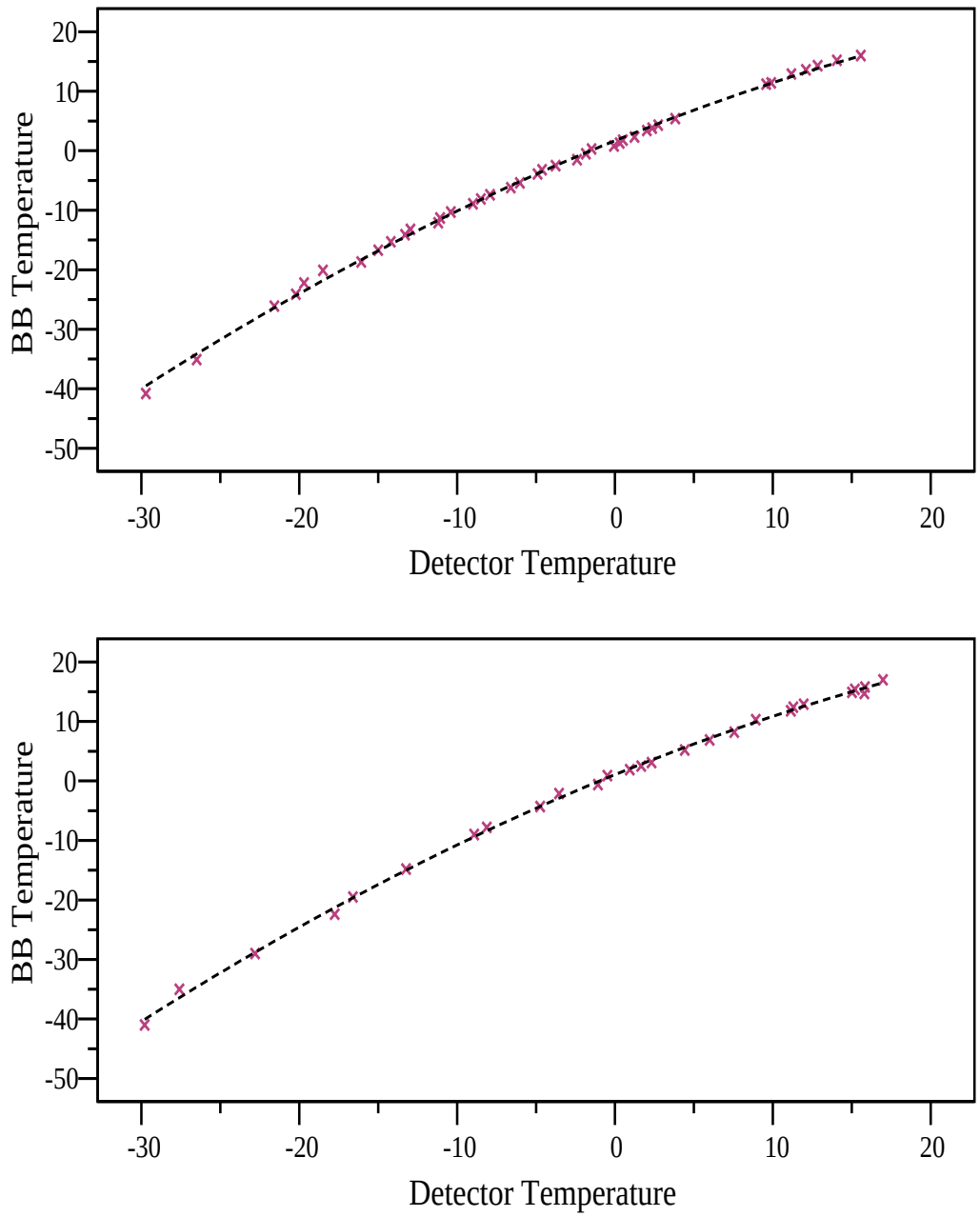

Figure 3. 11: A plot of black body (BB) temperature versus the compensated output temperatures along with second degree-polynomial fit for STD detectors. These are (from top to bottom) STD 3^o and STD 90^o.(-) is the fitted line.

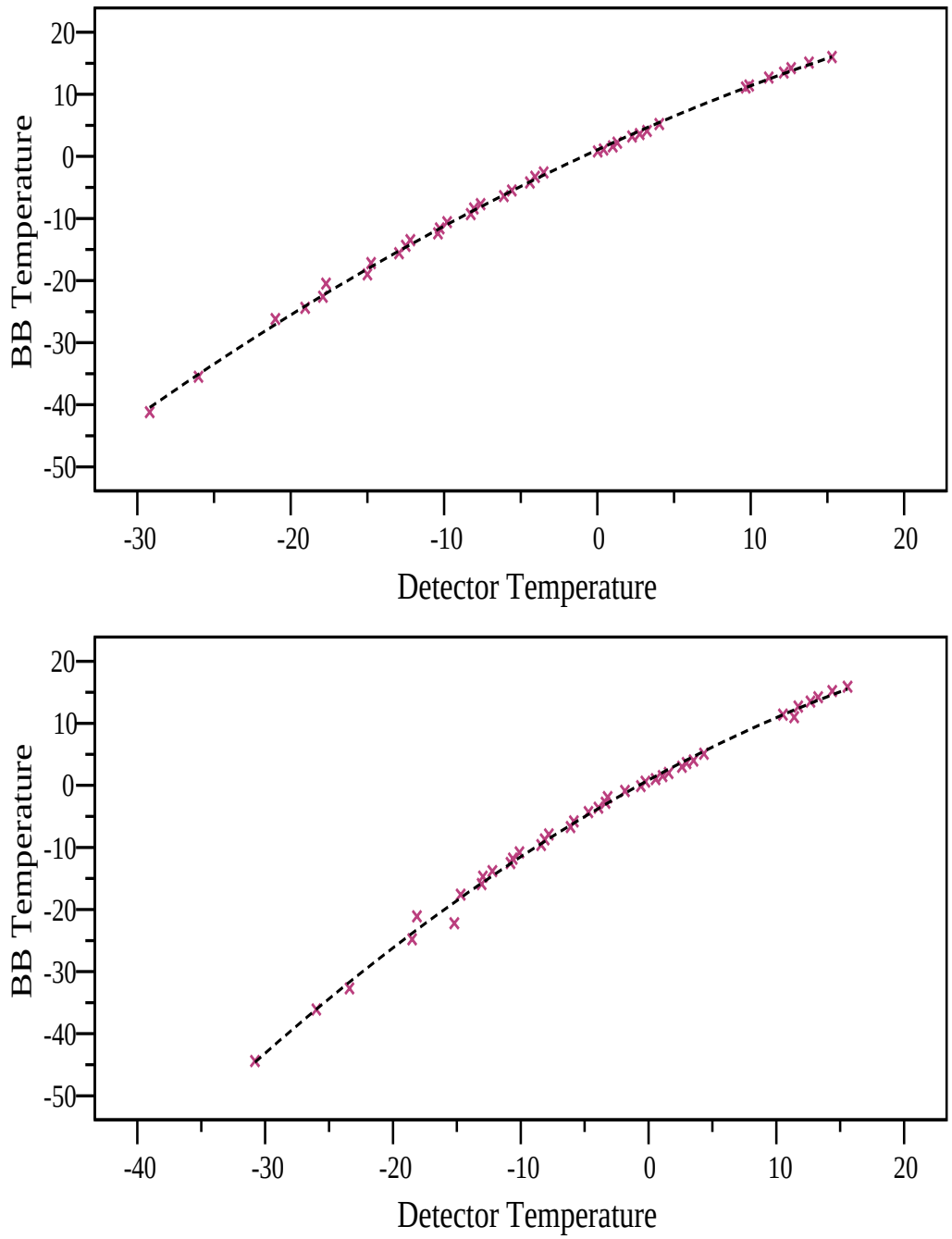

Figure 3. 12: Same as figure 3.11 but for G15 filters temperatures the top panel is for to G15 filter with 3^o FOV while the lower panel is for G15 90^o FOV. (-) is the fitted line.

It is clear from those curves that at temperatures above 0 ^oC the detectors read temperatures similar to those for the BB temperatures. On the other hand, for lower temperatures the detectors do not give the exact BB temperature. In this case corrections are needed for the detectors measurements.

Table (3.1) shows the quadratic fit formula for each detector along with the regression coefficient and standard errors for this fit. This calibration was conducted three times between 2003 and 2005. This was to achieve optimal performance for the detector as a good cloud identifier. The results of the repetitive calibrations showed no major differences, drift or any major changes to the formulae considered here.

The correlation coefficient for all the formulae was not less than 0.996. Also the root mean square error (RMSE) was not more than half a degree in the worst case. These equations are describing the output temperature of the detectors over a wide range of temperatures and can be used with excellent accuracy.

These formulae are of great importance and one task of this project was to produce and validate them.

Filter	FOV	Quadratic Fit	RMSE ^{o}C	R^2
G15	3	$T_{BB} = -0.010T_{Det}^{\ 2} + 1.077T_{Det} + 1.693$ (3.14)	0.59	0.998
G15	90	$T_{BB} = -0.010T_{Det}^{\ 2} + 1.080T_{Det} + 1.026$ (3.14)	0.58	0.998
STD	3	$T_{BB} = -0.011T_{Det}^{\ 2} + 1.130T_{Det} + 1.058$ (3. 15)	0.52	0.998
STD	90	$T_{BB} = -0.011T_{Det}^{\ 2} + 1.121T_{Det} + 0.855$ (3. 16)	0.86	0.996

Table 3. 1: Presents the absolute calibration formula for each filter with the corresponding FOV. It also shows the fit parameters, the correlation coefficient, and the root mean square error RMSE (or the standard error of the estimate). T_{BB} is the black body temperature, which in our case is the sky temperature, T_{Det} is the temperature measured by the detector based on 50 mV/^{o}C scaling factor. All the temperatures here are in units of ^{o}C.

Fig (3.13) shows sample data for both the 50mV/^{o}C-linear correlation and the quadratic calibration formula for the G15 detector with 3^{o} FOV for the period from 24 April to 1 May 2005. The figure shows a consistency between the two methods over warmer temperatures, particularly relevant in cloudy times. In clear sky periods, which show colder temperatures, the quadratic calibration scheme should represent the temperatures more accurately.

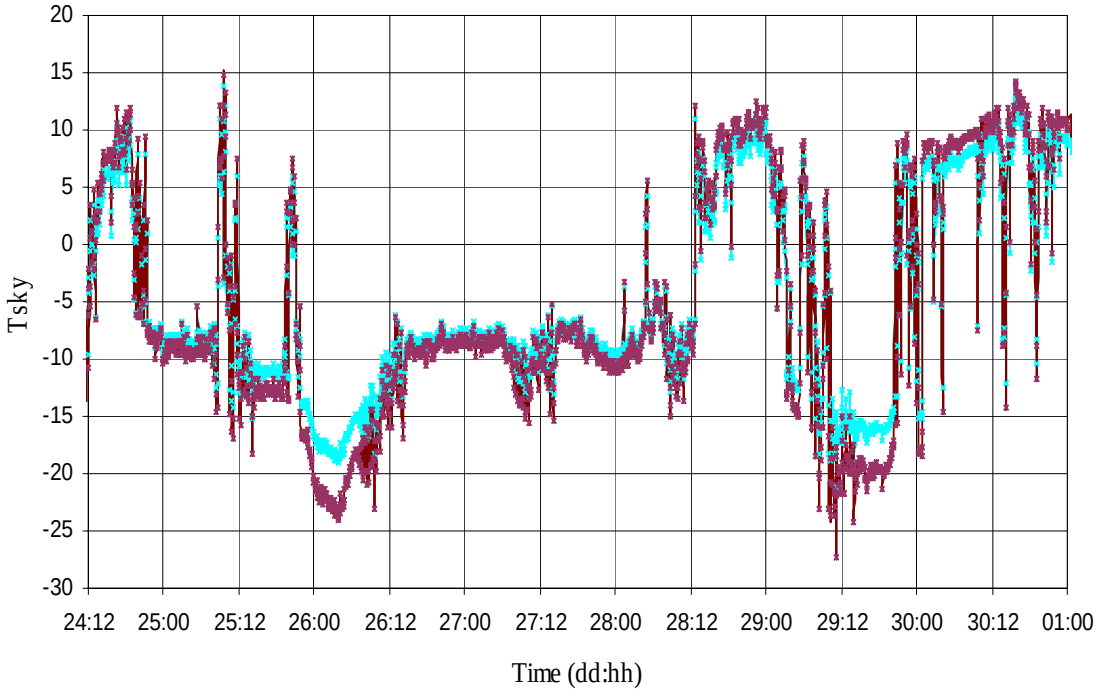

Figure 3. 13: Shows an example from G15 detector monitor with 3^{o} FOV for the period from 24 April to 1 May 2005 for different sky conditions. It shows comparisons between 50mV/^{o}C calibration scale (dark dotted line) and temperatures obtained from the calibration formula equation (3.14) (light green). It shows the agreement between the two scales for warmer temperatures. They differ from each other at colder temperatures where the calibration formula gives the exact sky temperature. The sky temperatures are in ^{o}C.

3.6 Results

3.6.1 Measurements from the Vertical Cloud Monitors

The detectors were tested for their sensivity to cloud coverage for different sky conditions. These conditions vary according to the cloud cover from clear, through partly cloudy, to totally overcast skies. Figure (3.14) shows hourly data taken between 26 May and 4 June 2005 by the STD detector with 3^{o} FOV at the zenith. The

temperatures presented are uncompensated, thermistor and compensated in ^{o}C. Cold temperatures represent clear sky, and warm temperatures (near 0^{o} C) indicate low, thick cloud. The sky was predominantly cloudy over this period. The exceptions were on the morning of 29 May when the sky stayed clear for more than a day, after which there was a build up for cloud followed by thick stratocumulus clouds through the rest of the day, which continued for the following two-day period. During this cloudy period (30 May to 2 June) the sky experienced overcast periods with some broken clouds. The small drop on the morning of the 28 May is due to a short period of clear skies before the clouds developed again in the FOV. From the early morning of the 2nd June till late on the 3rd the sky remained clear.

It is evident that the discrimination between the clear sky and cloud in the FOV is straightforward at most times. A cloud discrimination criterion can be readily determined for the data set. Also the cloud detector's data generally agree with the cloud information recorded by Weather Bureau records, but are more detailed.

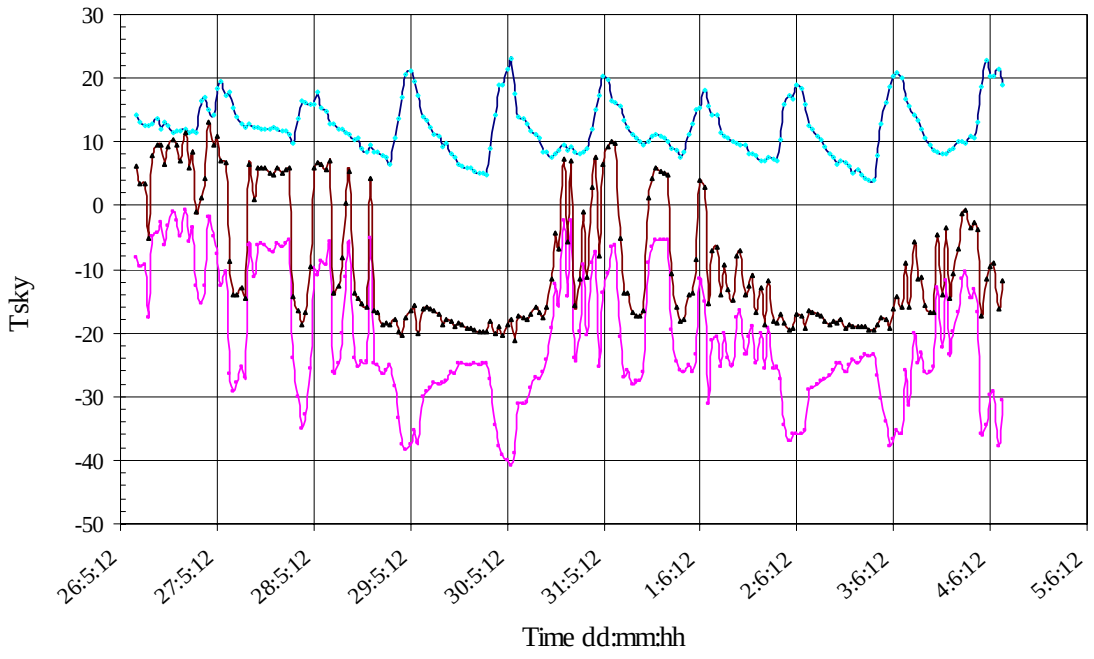

Figure 3. 14: shows a sample of data taken between 26 May to 5 June 2005 from the STD detector with 3^{o} FOV at the zenith. The data is presented in 1-hour resolution and temperatures presented are uncompensated temperature (dark line), thermistor temperature (light green line) and the compensated temperature based on 50 mV/^{o}C (pink line).

The monitor was exposed to direct or indirect sunlight in the FOV which caused considerable temperature variations to occur in the canister at those times. The temperature compensation is not perfect under those conditions, but in terms of defining a cloud free or cloudy FOV it remained adequate under difficult circumstances.

In order to remove solar heating effects and hence ensure an accurate indication from the cloud detector about the real atmospheric conditions, daytime measurements were removed from the data sample, and only night-time data were considered. This is the case for most astronomical and astrophysical situations. Figure (3.15) presents data for 3 night-times selected from the previous period. These data represent uncompensated sky temperature measurements with 3^o and 90^o FOV for both of STD and G15 detectors. The three nights were divided according to the amount of cloud reported at these times, from clear, to variable clouds and overcast sky.

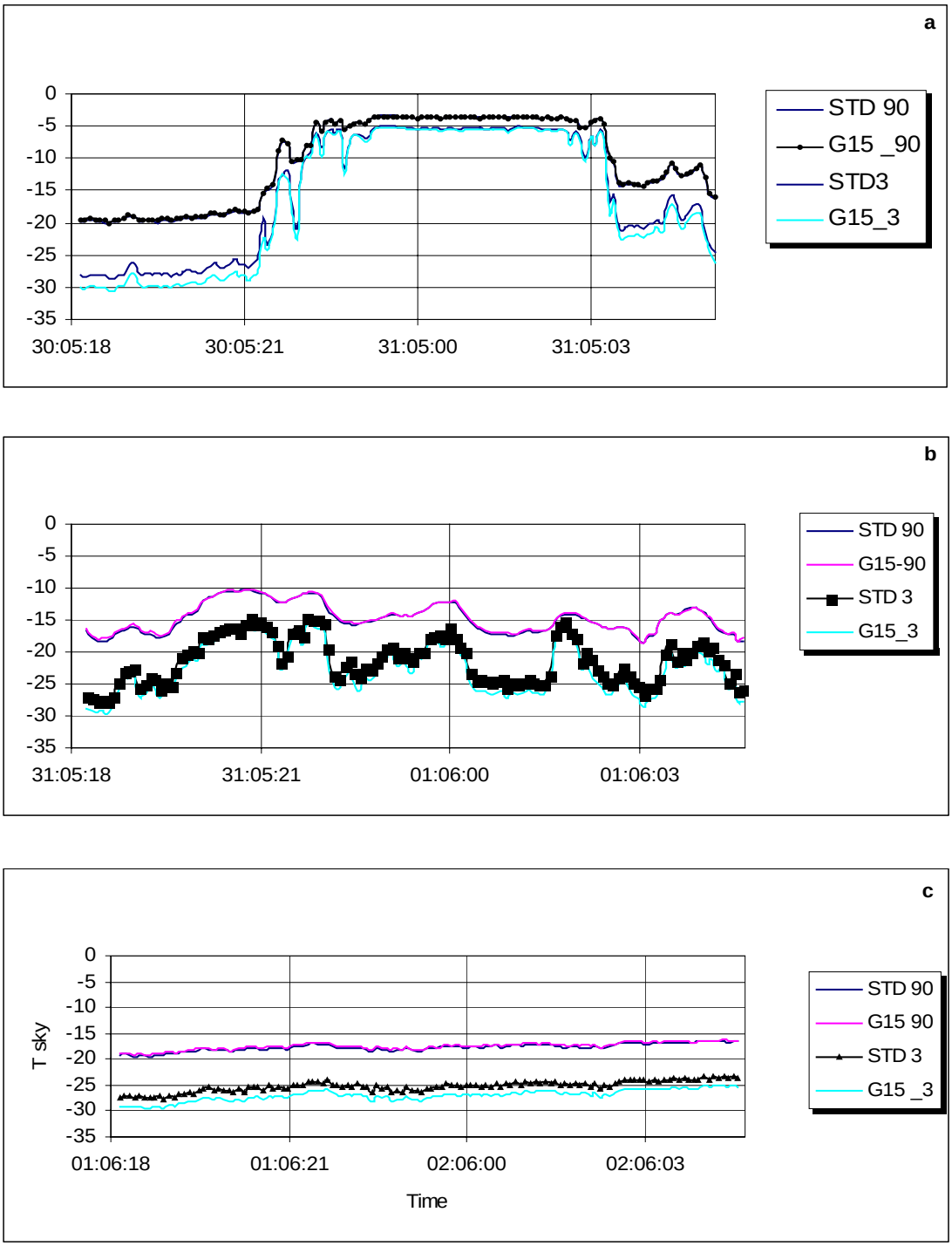

Figure 3. 15: Example of STD and G15 with 90^o and 3^o FOV outputs from Adelaide over three nights between 30 May to 1 June 2005. Each line represents the temperature difference between the measured sky temperatures and the detector temperature (Uncompensated). Top panel (a) represents clear sky, which then become overcast sky. b is a cloudy night with variable cloud amounts and properties, and c is totally clear sky.

Figure (3.15.a) represents a night which started as clear then cloud rolled in around 10 PM. The sky become totally overcast, represented by a plateau at higher temperatures, until around 3 am when the sky started to clear. Figure (3.15.b) represents a night with variable clouds with different properties, e.g. altitudes, emissivites etc. Figure (3.14.c) is a totally clear night with small variations, which may be due to air temperature or wind variations or variation on the amount of water in the atmosphere).

It is clear from their figures that all filters with their different FOV have shown almost consistent responses to the presence of clouds and clear skies. However, some aspects from these data are noteworthy.

1. Both G15 and STD with 90^o show very good agreement in their outputs with temperature differences of no more than 1 ^oC in all sky conditions.
2. Similarly, both filters with 3^o FOV have almost a constant difference in temperatures of about 3 ^oC in response to clear skies. This difference may well be related to the atmospheric humidity since the STD detector has more sensitivity in the window of strong water vapour emission than the G15 for a cloud-free atmosphere. Under overcast skies, and some cloudy periods, this difference in temperature between the two detectors reduced to about a degree. This related to the emission from the clouds in the atmospheric window 8 μm to 14 μm for which both detectors respond equally.
3. Under clear skies there is a difference of about 10 degrees between the 90^o FOV and 3^o FOV, for both filters, being colder for the former. This can be explained by the fact that the 90^o detectors have wider FOV which see more of the sky dome than the 3^o FOV.
4. However, this temperature difference is decreased to about 3 ^oC in overcast and some of the partly cloudy sky conditions, where the cloud cover changes slightly. This again may be due to filling the atmospheric window by the cloud emission, which is rather independent of viewing angle.
5. The 3^o FOV detectors show a fast response to the variation of some of the atmospheric conditions. For example in figure (3.13.a) on the 30^{th} of march at 10 PM when the clouds started to develop in the FOV there was some clear-sky periods before the sky became overcast.

During this time there was a quicker drop in the 3^o FOV detectors than in the 90^o FOV. This can be explained as the 90^o FOV is still viewing a mixture of cloudy and clear skies during this period, while the 3^o FOV will be more likely to see either fully clear or fully cloudy conditions.

Figure (3.16) shows histograms summarizing data from four of the vertical monitors over 1300 hours of night-time operation. These monitors are STD and G15 detectors with 3^o and 90^o FOV for each filter type. The data were taken from the Adelaide site for a period of around 4 years covering a wide range of atmospheric conditions. The data were part of the data used in the investigations conducted in this project. The figure shows interpretation of the criteria for interpreting cloud monitor data. The temperature difference between the detector-measured sky temperature and the thermistor (uncompensated) is shown for three types of skies. The sky is classified as totally clear with 0-1 octa of cloud, partly overcast with cloud coverage of 2-6 octa, and totally overcast with coverage of 7-8 octa. This classification is based on the records of the amount of cloud defined by the Weather Bureau. The first four histograms (1^{st} row) are for 222 hours of data for totally overcast skies. They show the expected range of temperatures from all the detectors, which is between 0 ^oC to around –15 ^oC. The variation in the temperature depends mainly on the cloud properties; however, a mean of -6 ^oC is found in such cases. The second four histograms (2^{nd} row) are for 930 data points for totally clear skies. The temperature ranges for the wide-angle detectors from –30 ^oC to around –10 ^oC with an average of –18 ^oC. On the other hand the 3^o monitors showed colder temperatures between, –39 ^oC and –25 ^oC, with a mean of –27 ^oC for the STD and –30 ^oC for the G15 detector. This variation is mainly due to changing atmospheric conditions, e.g. air temperature and the amount of water vapor. Partly overcast skies are those skies, which showed clouds and clear sky periods at close to the same time. The temperature ranges in this case vary according to the sky clearness or the amount of cloud cover in the FOV. The temperature ranges are intermediate between the clear sky and overcast cases.

These histograms show us that there is clear separation between the cloudy and clear skies. The range of temperatures can be used to make data quality cuts for classifying the sky.

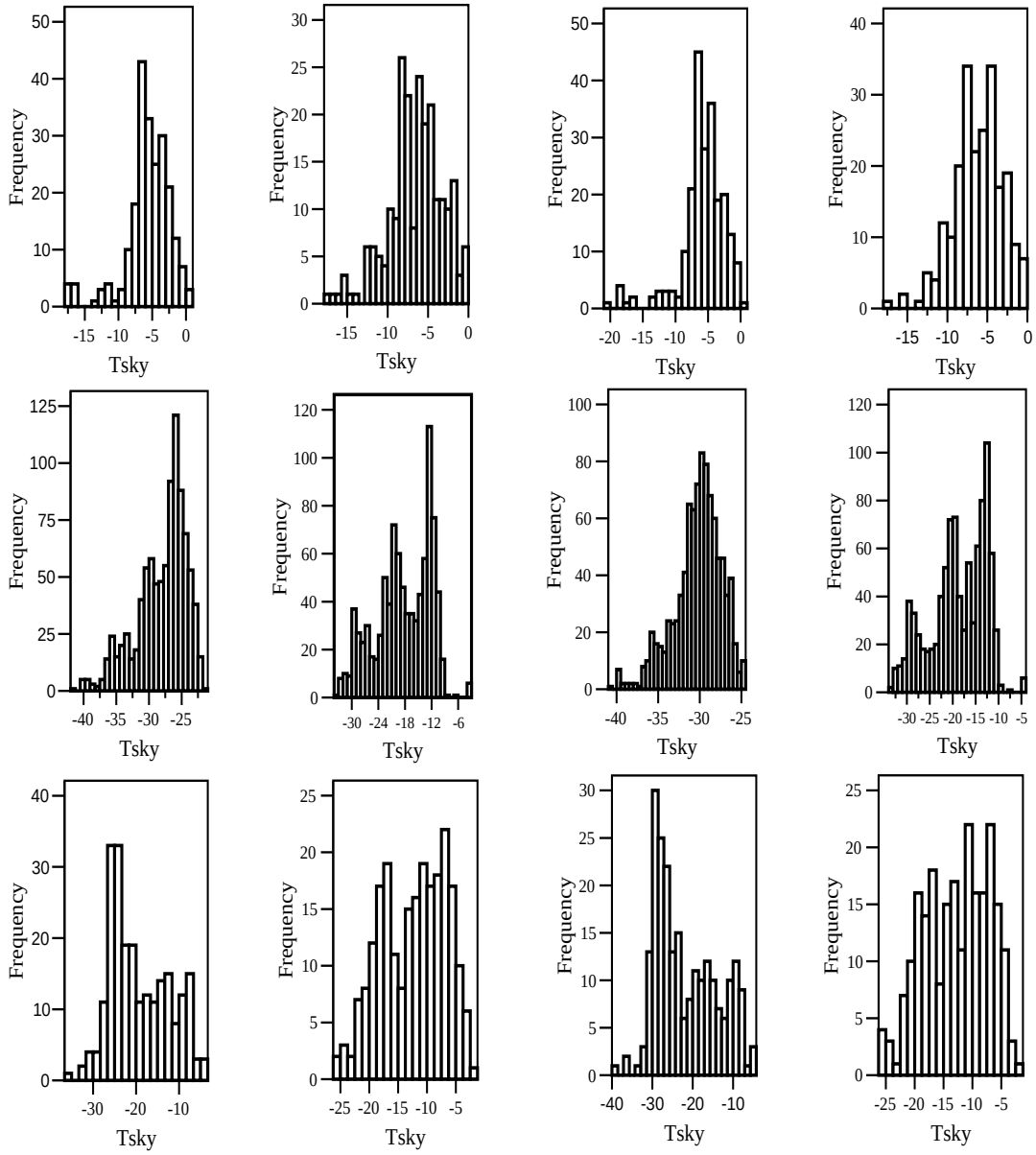

Figure 3. 16: Histograms (frequency distributions) of the uncompensated sky temperatures for STD and G15 detectors with 90^o and 3^o FOV. The first two figures in each row are for STD detector with 3^o and 90^o FOV respectively. Similarly, the third and the fourth figures in each row are for G15 detectors with 3^o and 90^o FOV respectively. The first (1st row) four histograms are for 222 hours of data for totally overcast skies. The second (2ndrow) four histograms are for 930 data points for totally clear skies. Partly overcast skies are the last (3rdrow) four histograms with a total of 230 data points.

3.6.2 Measurements from the Scanning Cloud Monitor

The scanning cloud monitor described earlier in this chapter allowed us to scan the sky from East-West through the zenith in 3^o steps every 5 minutes. Figure (3.17) shows an example of full scans from the scanner with a detector using the STD filter during the

night of 21-6-2002 at 1, 1:30, 2 and 3 am with different cloud coverage. Again, the temperature plotted is the uncompensated sky temperature and it ranges from –25^{o} C at the zenith to -3^{o}C near the horizon. This increase of the temperature at the horizon is a consequence of increasing the optical depth of radiating molecules (particularly water) within the band pass of the detector. At 1 am the sky was totally overcast, as represented by warmer temperatures. At 1.30 am the sky started to clear, which caused a drop in the sky temperatures, with some presence of cloud at some zenith angles. At 2 am the there are still some clouds in the FOV. Finally, at 3 am the sky became totally clear and clouds were almost absent in the FOV of the detectors. The curve now shows no structure. The above scenario is also applicable for G15 detector.

The scanner results provide us with a useful tool for detecting clouds over the whole sky dome. In this project, data from the scanner detectors were used, in addition to the cloud information from the weather records, as a basis for selecting clear skies as well as investigate the IR clear sky zenith angle distribution.

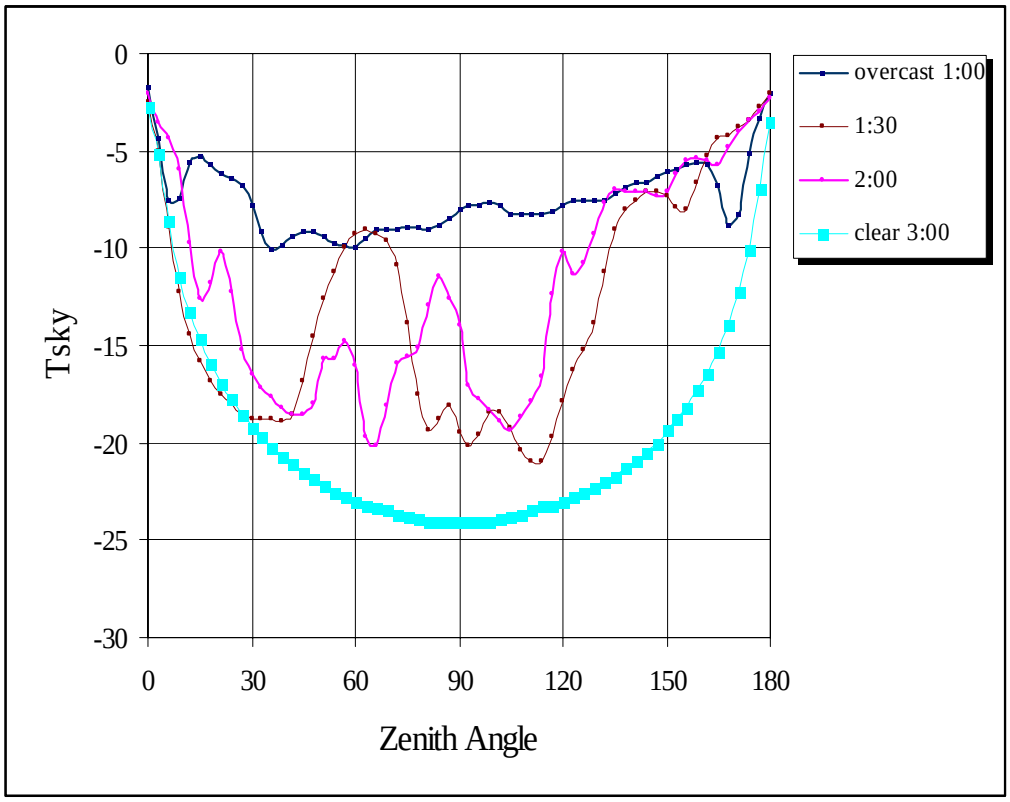

Figure 3. 17: Shows a sample from scanner detector for STD during a night 21-6 -2002 with different cloud covers between 1 am overcast, 1:30 am partly cloudy, 2 am partly with different amounts of clouds and at 3 am a totally clear sky.

3.7 Database

The data sets collected and used in this project contain sky temperature measurements from the IR cloud monitors for different atmospheric conditions over different periods of time from six sites around the world. In addition, the author has gathered data of surface meteorological variables, radiosonde measurements, and the amount of precipitable water vapor derived from a GPS receiver. All this information was obtained from different sources and places, and used to build up a large observational database for the purpose of different investigations conducted in this project.

Standard meteorological observations of ground temperature, dew point temperature, air pressure, and cloud information, such as cloud heights and cloud amounts, were obtained from the nearest airport to the field site.

In all sites the vapor pressure, as an important variable used in this study was calculated from standard formulations. For example the most commonly method is by knowing the dew point temperature. The vapor pressure (in mb) can be easily calculated from (Sonntag 1990):

$$eo = 6.1078 \times 10^{\left(\frac{(T_{dp} \times A)}{(T_{dp} + B)}\right)} \qquad (3.18)$$

where A = 7.5 and B = 237.3 K, T_{dp} is the dew point temperature in K

In the absence of any measure of the dew point temperature in our data set we also calculated it from the available formulae. There are several formulae for calculating the dew point temperatures. For the range from –45 ^{o}C to 60 ^{o}C the dew point temperature in ^{o}C is calculated using the measured relative humidity and air temperature from the following formula (Sonntag 1990):

$$T_{dp} = \frac{b.\alpha(T, RH)}{a - \alpha(T, RH)} \qquad (3.19)$$

$$\alpha(T, RH) = \frac{a.T}{b + T} Ln(RH) \qquad (3.20)$$

where a = 17.27 , b = 237.7 °C and RH is the relative humidity (not in percent i.e. RH/100) and T is the air temperature in ^{o}C. The uncertainty in the calculated dew point temperature using this formula is ±0.4° C, Hardy (1998). The difference between the T_{dp} calculated from the above formula and the measured values, for example, recorded at the Saudi meteorological Agency filed sites, was always below 2 ^{o}C.

Except for the CLF site all available radiosonde measurements for the above sites were also obtained from the corresponding database. These informations include the upper air measurements of the air pressure, air temperature and air density. Some other radiosonde data were taken from the University of Wyoming website[6] where the data are available to the public.

Radiosonde information was useful and mainly used in this project to calculate the total amount of the atmospheric water content, PWV, and the atmospheric water scale height. The former calculated from equation (2.15) while the latter calculated from (2.16). Data from radiosonde were also used as an input into MODTRAN atmospheric code as an atmospheric profile representing the upper air informations for the desired site (chapter 6).

At the Adelaide site, measurements of the precipitable water vapour (PWV) from the GPS receiver at the Buckland Park field site were used. These data are collected every five minutes and covered a period from September 2001 until July 2004. The GPS measured PWV was a useful tool in this study and gives it significance over other previous studies. Hence it is the first of its kind to use the GPS data to parameterize atmospheric radiation in comparisons with the most of the previous proposed models, where some of theses models were reviewed in chapter 2.

3.8 Methodology

While reducing data from the detectors it was necessary to exclude some of the data. This was mainly a matter of excluding from the reading all hours for which the sun was able to influence the detector system and become a source of heat to the sensing elements. Also excluded were all hours during which there was recorded rainfall and data where some meteorological information was unavailable.

[6] http://weather.uwyo.edu/upperair/sounding.html

After all data from cloud detectors were judged to be useable, and when their corresponding meteorological informations were available, a large database was created and became available for further investigation. Each data record was formatted to contain the following information:

- Time. Local Time yy:mm:dd:hh.
- Air temperature measured by the detector (thermistor) and air temperature obtained from the Weather Bureau.
- Dew point temperature (measured or calculated).
- Air pressure
- Calculated vapour pressure *eo*.
- Available PWV for some periods either from a Radiosonde or from the GPS Receiver.
- Cloud information obtained from the weather records.
- Cloud monitors vertical or/and scanner data for Adelaide site.

Having the database ready, the next step was to work with it by sorting it for an appropriate future use. For the purpose of this project, the database was divided into clear, overcast, and partly overcast skies. The criteria for selection of appropriate sky conditions will be discussed in the subsequent chapters.

With the selection of the data for an appropriate purpose the calibration formula, Table (3.1), for the desired filter and FOV were then applied.

The methods used in this project were compared on the basis of standard regression analysis. These mainly parameterize the formulae, investigate the regression and the associated statistical parameters, and then test the validity of that parameterization.

The main procedure used in this study was as follows.

Regression analysis was applied between the measured sky temperature and the meteorological parameters that physically describe the situation. The resultant formulae from this regression were then tested. The data calculated from the proposed formulae were plotted and statistically tested against the corresponding measured values. In some cases a proposed model was tested against some of the available formulae found in the literature. The proposed formula may also be tested using an independent dataset.

For the ideal case when each calculated value equalled the measured values, all points of the scatter plot would be in a straight line whose slope is one and whose intercept is zero. Such a set of points would also have a correlation coefficient of 1 and standard errors of estimate of zero.

Computer software, mainly SPSS and Mathematica, was used to make the parameterization, statistical tests, validation, and comparisons. The above procedures were followed in parameterizing clear and overcast skies.

In parameterizing clear sky formulae the procedure followed in this study was to establish a formula that had enough parameters to predict the clear sky temperatures with minimal statistical biases. This was done by using a single parameter (simple linear regression), and then using two parameters (multiple regressions). These parameters were chosen to correctly describe the real situation and have a real physical relationship with the sky condition. Throughout this study, the ground level measurements of air temperature and a ground level vapour pressure are used as a independent variables to parameterize the clear sky temperatures. However, measurements of the PWV were also used to parameterize the clear sky temperatures.

The established formula for clear skies was used at some sites to predict the presence of clouds by predicting the change of temperature levels between cloud and clear sky as we shall see later.

The screen level water content throughout this text alternatively denoted *Sqrt(eo)* or $\sqrt{eo}$, and alternatively called vapour pressure, water vapour pressure or screen level vapour pressure. Similarly air temperature alternatively may be called screen level air temperature and denoted as T_{air} or T_a.

Most of the statistical tests were performed using SPSS statistical software (Statistical Package for Social Science). The program computes a regression with the following statistics: the correlation coefficient (r), the standard error of estimate or root mean square errors (RMSE), the constants of the regression analysis (intercept, slope) and their associated statistics, Student's t-test, one-way ANOVA for repeated measurement, and mean bias error MBE.

The correlation coefficient, R^2, is an indication of the degree of linear correlation between the measured and predicted set of points. It is defined as a statistical measure of the interdependence of two or more random variables, it indicates the strength and direction of a linear relationship between two. It can vary from -1 (perfect negative correlation) through 0 (no correlation) to +1 (perfect positive correlation).

The equation for the correlation coefficient between two variables is:

$$R = \frac{\sum (x - \bar{x})(y - \bar{y})}{(n-1) S_x S_y} \tag{3.21}$$

where $\bar{x}$ and $\bar{y}$ are the sample means of x and y, S_x and S_y are the sample standard deviations of x and y and the sum is from i = 1 to n.

The mean bias error (MBE) is the difference between the estimated values from the fit and the measured values and defined as:

$$MBE = \frac{\sum (T_{i,cal} - T_{i,mes})}{n} \tag{3.22}$$

where $T_{i,cal}$, and $T_{i,mes}$ are the calculated values from the regression equation and the measured values respectively, and n is the number of observations. A low MBE is desired. A positive value gives the average amount of over-estimation in the calculated value and vice-versa. (Ma,C.C.Y. and Iqbal, M 1984).

Also the root mean square error RMSE is defined as:

$$RMSE = \sqrt{\frac{\sum (T_{i,cal} - T_{i,mes})^2}{n}} \tag{3.23}$$

This is a measure of the fit quality by allowing term-by-term comparisons of the actual deviation between the calculated value and measured value, (Ma,C.C.Y. and Iqbal, M 1984).

The RMSE and MBE are the two most important tests used in this project to evaluate the accuracy of the correlations analysis. All the presented models in this thesis will be compared by the predicted to measured correlation coefficient(R) which can be calculated by:

$$R = \sqrt{1 - (MBE \times VAR^{-1})} \tag{3.24}$$

Where MBE is the mean bias error and VAR is the variance.

For further details about the explanation of the other statistical parameters from SPSS see, for example, Lee *et al*.(2005).

3.9 Comments on the Operations of the Detectors

The absolute calibration for Adelaide cloud detectors was made 3 times during their period of operation. This calibration was conducted for three reasons. The first calibration was to produce the absolute curve to be used for real data analysis. The second calibration was done 2 years later to check if there was any drift or misbehaviour from the detectors or from their components. The third calibration was done after replacing the lenses and covers. No major differences were found, nor were any major drifts observed.

Daily and weekly checks were done by observing the displayed output from the detectors on the screen of the PC. During the years of operation, the detectors had a number of periods of downtime. The STD detectors were replaced by another detector in July 2003 namely G7. These detectors have a narrow band response around 9.5 μm and were installed for different study. However, since July 2004 all the 6 detectors have continued in operation and, since that time, they have continued to work well.

The data from Saudi sites were downloaded every 90 days for some stations. After collecting a reasonable amount of data from 3 sites, which have detectors with 90 FOV, these detectors were taken out of operation for maintenance purposes. The covers of the detectors were replaced by high quality polyethylene to operate in the extreme conditions experienced in Saudi Arabia. The fourth one, which has a 3^o FOV, still continues in operation.

Both G15 and STD detectors were installed at Adelaide of the same location. They both have a peak response at 10 μm and a similar upper limit of response. Consequently they both have similar transmission characteristics and have consistency in responding to the presence of clouds. We have seen previously that both detectors work perfectly as cloud identifiers and both have the same temperature ranges in overcast conditions. We also noticed (see chapter 4) close similarities in measuring sky temperatures over different sky conditions between the G15 and STD detectors with 3^o FOV. Hence, in this study, it has been assumed that the results from one filter will be representative of the other, to avoid any repetitive discussion.

CHAPTER FOUR

PARAMETERIZATION OF I.R CLEAR SKY TEMPERATURES USING GPS MEASURED PWV AND GROUND LEVEL PARAMETERS IN ADELAIDE

4.1 Introduction

This chapter describes the first of four studies conducted in the first part of the work to be presented in this thesis. These studies are based on data collected from different cloud monitors operated at the Adelaide site. The techniques and the instrumentation detailed in chapter three are used to study and parameterize night-time clear sky temperatures at the zenith.

This chapter presents two parameterizations of the IR clear sky temperature at the ground as measured by the cloud monitors. The *first* model is based on the screen level temperature and the amount of precipitable water vapor PWV (T_a, PWV) as measured from GPS satellite transmissions. The *second* is based on the screen level of temperature and the square root of the ground level vapor pressure (T_a, $Sqrt(e_o)$). These

models were developed for the 3^o FOV and 90^o FOV, STD and G15 filters. In both cases the functional forms, MBE and RMSE for the two filters with the two FOVs will be summarized, while the discussions and the results presented will be restricted to those found for G15 detector with 3^o FOV.

The first model was found to predict the sky temperature with high accuracy (standard deviation less than 2 ^oC) for the G15 detectors. The model allows us to reverse the process to determine the clear sky PWV with an uncertainty of the order of 2 mm. In the absence of the PWV measurements the alternative model (model 2) was found to give a reasonable performance with standard deviation of less than 3 ^oC for the G15 detector.

These models for the G15 detectors having a 3^o FOV were tested against some of those found in the literature.

4.2 Observational Data

The observational dataset consisted of measurements of the clear sky temperature from the Adelaide infra-red cloud detectors, surface meteorological data, radiosonde data, and the amount of precipitable water vapor. A brief description of how these data were collected and used will be given in the following sub-sections. Also, the criteria of selecting clear sky data and the method of analysing the data will be given in the last two subsections.

4.2.1 Precipitable water vapour from the GPS at The Buckland Park (BP) Field Site

As part of the Australian Regional GPS Network (ARGN) the atmospheric physics group of the University of Adelaide installed its GPS system at its Buckland Park (BP) field site in August 2002. The GPS antenna is a NovAtel 600 pinwheel antenna, connected to an OEM4 receiver. The site coordinates are; longitude (E 138 28 5.40), latitude (S –34 37 36.59), and height (13 m). The antenna is primarily designed for marine or kinematics applications. A detailed description of instrumentation, techniques, measurements and data acquisition and treatment for the BP experiments can be found in Alexander (2004).

Over the last decade, much work has been done to demonstrate the capability of the Global positioning system (GPS) to derive atmospheric PWV (e.g. Bevis *et al*. 1992, Bevis *et al*. 1994, Rocken *et al*. 1993).

In the following, a method of estimating the PWV using GPS will be briefly discussed. For more details in this subject see, for example, Bevis *et al.* 1992.

Radio signals transmitted from GPS satellites are delayed by the atmosphere before they are received on the ground. Some of that delay is due to the presence of water vapor in the troposphere. The tropospheric delay Δ_{trop} can be expressed by:

$$\Delta_{trop} = \text{ZHD} + \text{ZWD} \tag{4.1}$$

Where ZHD is the zenith hydrostatic delay, and ZWD is the zenith-wet delay. The ZHD can be calculated with high accuracy if precise measurements of the surface pressure at the receiving site are available (Saastamoinen 1972; Asken and Nordius 1987) by:

$$\text{ZHD} = \frac{(2.2768\times10^{-3})P_s}{[1-2.66\times10^{-3}\cos\ (2\theta)-(2.8\times10^{-7})H]} \tag{4.2}$$

Where θ (in radians) is the latitude, H (m) is the altitude, and P_s(mb) is the surface pressure. The value of ZHD for Buckland Park was 2.296 m Alexander (2004). A software package from the Jet Propulsion Laboratory (JPL) called GIPSY-OASIS II was used to solve the GPS observable carrier phases and calculate the tropospheric delay. The software requires specific orbital information from the satellite plus the position of the antenna to make water vapor calculations. Zenith Wet Delay was subsequently derived by subtracting the ZHD from the measured tropospheric delay. The ZWD is the delay attributed to water vapor in the troposphere. PWV can then be derived from the ZWD (Bevis *et al.* 1994 and Asken and Nordius 1987) by:

$$PWV = \kappa \times ZWD \tag{4.3}$$

Where

$$\kappa = \frac{10^8}{\rho_w R_v [(\frac{k_3}{Tm}) + k_2]} \tag{4.4}$$

and ρ_w is the density of water (kg/m^3), R_v is the specific gas constant of water vapor (J/kgK), k_2 is (22.1 ± 2.2) (K/mb), k_3 is (3.739 ±0.012)×10^5 , T_m is the weighted mean temperature of the atmosphere(K) and can be calculated from :

$$T_m = \frac{\int (\frac{e_o}{T}) dz}{\int (\frac{e_o}{T^2}) dz} \tag{4.5}$$

where e_o is the vapor pressure (mb), and T the temperature of the atmosphere (K). Both vapor pressure and temperature at height z are deduced from radiosonde measurements. In general, κ is about 0.15 and it is a function of season, location, and weather. Its spread may scatter over a range of 20 % (Bevis *et al.* 1994). For Buckland Park, the mean value of κ was calculated using three years of radiosonde data from Adelaide airport and found to be 0.16 ± 0.003, (Alexander 2004). Knowing both κ, and ZWD, the PWV was then derived using equation 4.3.

The PWV data are reduced in two modes, real time data, and post-processed data. Real time GPS data are those PWV deduced from the predicted orbital data for the satellite position. The post-processed data are water vapor amounts calculated using the final orbital information of the satellite, which is usually available two weeks after the orbit occurs. The main difference between the two methods is that the former gives quick information about the amount of water vapor 15 minutes after the orbital pass occurs. This method is preferable for weather prediction calculations, which requires at least two hours of such information. Post-processed data are more accurate since exact orbital parameters are used, but they are only available afterward.

The PWV used in this study, was calculated for every five minutes using post-processed methods. The root mean square variation for the data is 1 mm. Comparisons between PWV measured at Buckland Park (BP) using the GPS method and PWV measured at Adelaide airport using a radiosonde show that the PWV at Buckland Park is generally lower than the radiosonde measured PWV, especially for PWV values less than 20 mm (Alexander 2004). The bias of this comparison was 2.1 ± 1.4 mm, which may be due to the difference of air mass between the two sites. However, in the current study, due to

the small differences between the Adelaide and BP, it was assumed that the GPS PWV data can be used to high accuracy for our purposes. The PWV data collected and used in this study covers a period from September 2002 until July 2004, excluding the period from September to December 2003, when the data were not available.

4.2.2 Meteorological Data from Adelaide Airport

Half-hourly standard meteorological observations of ground temperature, dew point temperature, air pressure, and cloud information were obtained from Adelaide Airport records made by the Bureau of Meteorology. This is located at a distance of 30 km from BP site, and 8 km from the city of Adelaide. These data covered a period from July 2001 until September 2005. Also, some available radiosonde profiles were used during this period of time.

4.2.3 IR Sky Temperature Measurements

The infrared sky temperatures were obtained from the cloud detectors, which were in operation since July 2001. These detectors were installed on the roof of the Oliphant Wing of the Physics Building, at the University of Adelaide, South Australia. Four cloud detectors were in operation, two STD and two G15. The detectors were operated in two modes, *fixed*, and *continuous scan* (chapter 3). Sky temperature measurements were selected for each half an hour period, to match those data recorded by the Weather Bureau.

During the years of operation, the detectors had a number of periods of downtime. The standard STD scanning detector and the 90^{o} FOV detector were removed in January 2002. From June 2002 till December 2002, G15 and STD with 90^{o} FOV showed drift and severe misbehaviours. This may be caused by the effect of solar heating to their window materials due to the continuous exposure to the sun at their fixed position. In February 2003 all detectors were taken off for maintenance. The STD detectors were replaced with another detector namely G7, in July 2003. G7 is a detector installed to study the atmospheric emission in the atmospheric window with wavelength centered at 10.9 μm. In early March 2004 all detectors were removed for calibration and maintenance purposes. From mid-March 2004, a total of six detectors of STD, G15 and G7 with 90^{o} and 3^{o} FOV in scanning operation mode were placed all together at the

same rotator and started acquiring data. Here the 90^{o} detectors also rotate but they only take a reading when the system at the zenith. Since that time all the detectors have operating continuously without any apparent faults or fatigue.

Comparisons between air temperatures obtained at the airport and those measured by the thermistor (inside the thermopile) at the roof, showed that, at night times, 99.6% of the differences between the two readings are less than 1 ^{o}C. It would not be expected that the two air temperature measurements would be exactly equal at all times, primarily due to the difference in location. The Bureau measurements are near ground level, while the roof site measurements were taken at top of five-story building. It was felt that the thermistor would be more representative in observing temperatures, since it is at the same height as the cloud detectors. Consequently, temperature measurements by the thermistor were taken and used in this study as the measure of the air temperatures at the level of observations (screen level temperature).

Also, it was assumed that the sky dome seen from both sites (separated by 8 km) was essentially the same. This implied that the cloud data would be nearly the same for both site.

4.2.4 Clear Sky Selections

For the purpose of studying the clear sky, clear-sky times were selected by use of the following criteria:

1. The visually observed total cloud cover reported by the Bureau of Meteorology has to be zero octa. Despite the fact that the observations were made at nighttime, the visual cloud observations are considered reliable in most cases. However, we believe our cloud detectors were able to observe all types of cloud equally during the day or night.
2. The absence of any structure in the scanning curve, i.e. the full sky curve from the scanner has to be totally smooth at the time that matches zero cloud cover. Therefore, data from the scanners were also used in judging the presence of clouds.

Figure (4.1) shows an example of two scans, from east to west through the zenith from the G15 detector. The scans represent a totally clear sky and sky with cloud close to the zenith. The depth of the curve represents its response to the sky temperature at that

angle. Generally speaking, the clear skies always show a curve with absence of any structure and have colder temperatures. Cloudy skies, on the other hand, always have a structured pattern at the angle where the clouds are found. They can also be distinguished by an increase in the measured temperature.

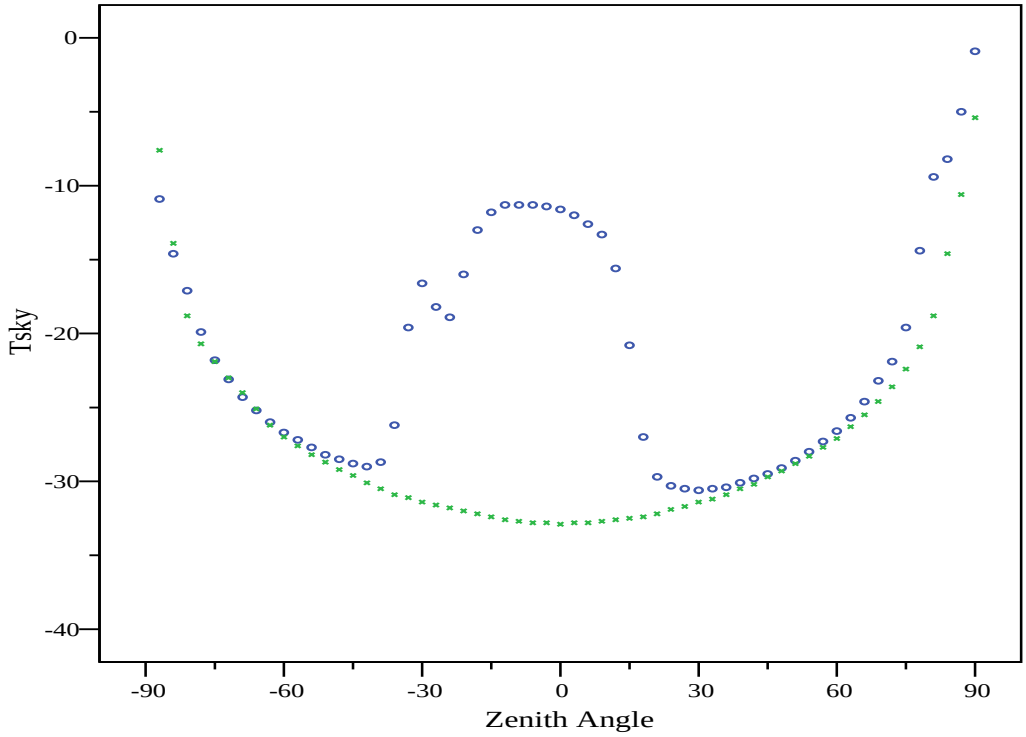

Figure 4. 1: East-West scans through the zenith for a G15 filter for clear sky temperatures, in ^{o}C, (Green squares) and for partly cloudy sky (Blue circles). The zenith angle is in degrees.

4.2.5 Data Treatments

The analysis procedures discussed in section 3.8 for parameterizing the clear sky temperatures will be followed here.

Clear sky data, using the methods described in the previous section, were extracted from the main database after being calibrated. Regression analyses between the IR clear sky temperatures, the local screen temperature (*Ta*) and the PWV (from the GPS receiver) were carried out in the first part of this study. In the second part, the parameterization of the sky temperature was achieved using the screen temperature and the square root of the vapor pressure $Sqrt(e_o)$.

4.3 Relation between PWV from GPS Measurements and Clear Sky Temperatures

As we saw in reviewing the literature for parameterizing the atmospheric IR radiation, that radiation is usually fitted as a function of screen temperature or/and ground level water parameters. However, no clear link has been experimentally established up to this time between this radiation and the PWV using measured PWV from radiosonde or by any other method. Even in the model developed by Dilley and O'Brien (1998) the precipitable water vapor has been established using atmospheric profiles extracted from a standard data base (TIGR data base.) not from real measurements Also, using the measured PWV from GPS satellites in parameterising the clear sky temperatures was the first to be conducted in this study.

The measurements for the PWV, air and sky temperatures covering the period from October 2002 until July 2004, excluding the early days of August 2003 which did not include enough clear sky data points, are used here. The data at times for which the detectors were suspected of misbehaving or were not in operation were also excluded.

A total of 626 scans for G15 (3^o FOV), 432 for STD (3^o FOV), 425 for G15 (90^o FOV) and 377 for the STD (3^o FOV), were judged to be completely clear using the criteria discussed in section(4.24) and with corresponding GPS data available for analysis. For this work, the *zenith* temperatures from the scanners and the temperatures from the wide angle detectors were used. A summary of the main statistical parameters for the measurements used in this study is given in table (4.1).

Results from the G15 detector with 3^o FOV will be considered and discussed in detail. Similar results are expected for the STD detectors with the same FOV (see chapter 3). This is because the G15 detector with a narrow FOV has less downtime and so has a reasonable amount of data during the period of running the GPS experiments. However, fits to the data from the other detectors will be given in the text but without any further considerations.

STD 3^o FOV (N = 432)					
	Range	Minimum	Maximum	Mean	Std. Deviation
PWV (mm)	18.42	1.86	20.29	10.65	3.46
Ta(^{o}C)	23.60	5.50	29.10	16.21	5.50
Tsky(^{o}C)	24.56	-29.29	-4.72	-17.53	4.29
STD 90^o FOV (N = 377)					
PWV(mm)	16.52	3.77	20.29	10.64	3.40
Ta(^{o}C)	23.60	5.50	29.10	16.02	5.75
Tsky(^{o}C)	28.93	-23.19	5.74	-8.91	5.88
G15 3^o FOV (N = 662)					
PWV(mm)	19.83	0.46	20.29	9.84	3.79
Ta(^{o}C)	23.60	5.50	29.10	15.81	4.95
Tsky(^{o}C)	23.06	-27.96	-4.90	-17.62	4.60
G15 90^oFOV (N = 425)					
PWV(mm)	19.83	0.46	20.29	9.92	3.84
Ta(^{o}C)	23.60	5.50	29.10	15.39	5.76
Tsky(^{o}C)	26.69	-20.22	6.47	-8.61	5.59

Table 4. 1: Overall statistics for clear sky night-time values of PWV from GPS, T_a, and Tsky for STD and G15 filters with 3^o FOV and 90^o FOV during the period of study.

Hourly variations of the sky temperature and the air temperatures and the precipitable water vapor, PWV, for the G15 detector are shown in Fig. (4.2). Sky temperature is clearly correlated with air temperature and the PWV, although with spread in the data. In both cases the general trend is an increase of the sky temperature with an increase to any of the two parameters. This also confirms that over different seasons, e.g. summer and winter, the relationships are still valid. The spread in the figures may be reduced if both parameters are considered together through multiple regression or other parameters are included, as we shall see later

The correlation between air and sky temperature is not surprising; the mean temperature of the sources of sky radiation is related to the air temperature, which in turn is related to the temperature at the ground level. This positive relationship indicates that the temperature in the part of the atmosphere where the radiation originates is correlated by some combination of radiation, turbulence, and advective process to the surface temperature. The dependence on the second parameter is generally needed, since atmospheric water vapour strongly absorbs the infrared radiation as a result of both infrared continuum and selective absorption by its vibro-rotational and rotational absorption bands centred at infrared wavelengths longer than 5 μm. That is, within the spectral range characterised by the most intense atmospheric emission (Bignell, 1970; Goody, 1964).

Regression analysis between the sky temperature and the PWV and air temperature using one independent variable will be described in the following subsection. Regression results optimized by multiple regression using two independent variables will be presented in subsection (4.3.2).

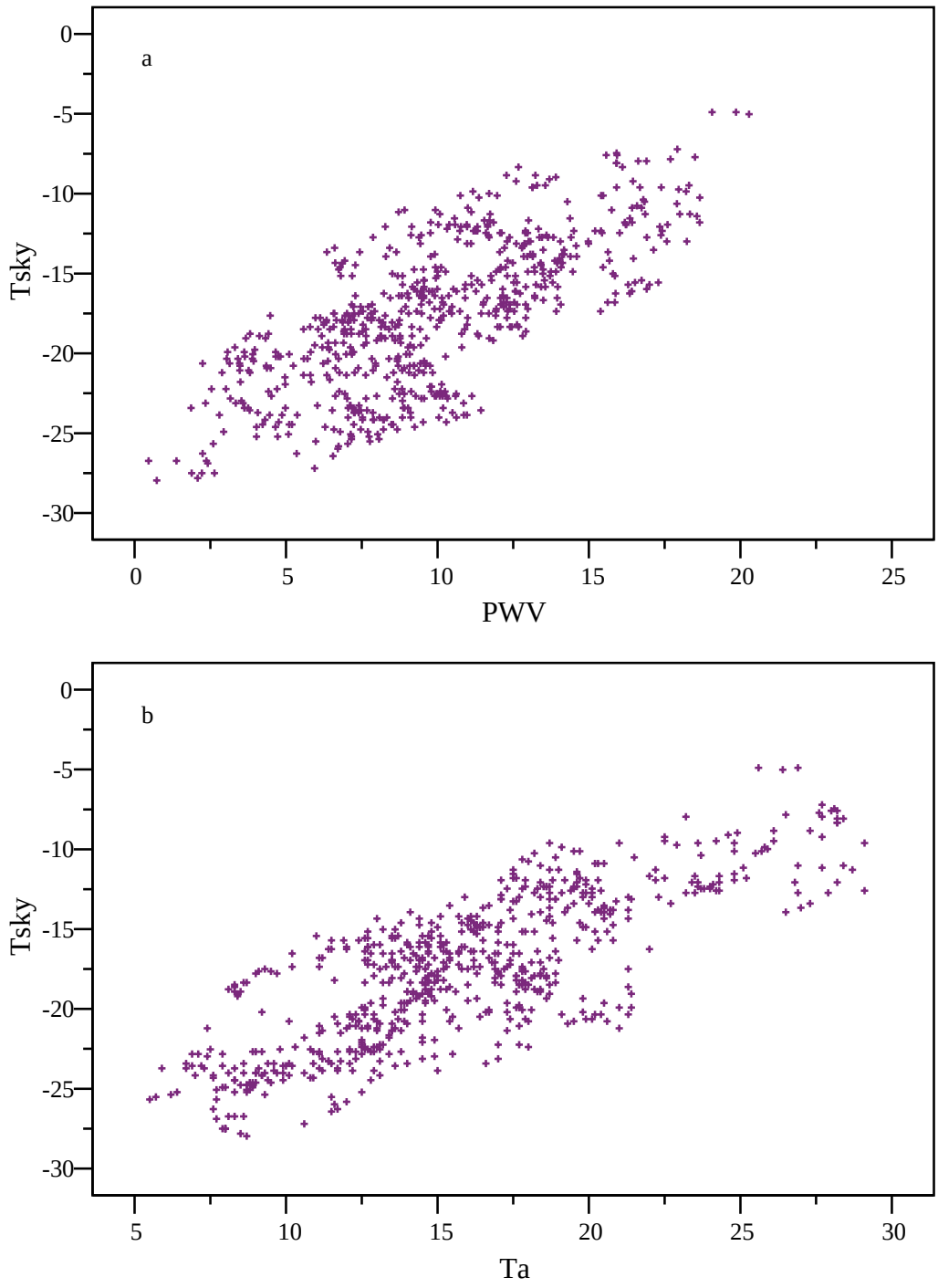

Figure 4. 2: Shows the relationship between hourly clear sky temperatures (Tsky) in ^{o}C and a: the PWV in (mm) and b: air temperature (Ta) in ^{o}C.

4.3.1 One Variable Models

The analytical form, the coefficients, and the modelled-to-measured root mean square errors and correlation coefficient are given for all the one variable regression models in table 4.2. Non-linear (logarithmic, power law, and exponential) fits were tried but gave no better results than the linear fit.

As indicated by the statistics in the table, for all detectors the air temperature correlates better with sky temperature. This is confirmed by the values of the root mean square errors (RMSE), the mean bias error (MBE) and the correlation coefficients. Although these variables show different values from filter to filter, they generally show a better estimation of the sky temperature using air temperature than found using only the PWV. However, the dependence of the clear sky temperature on the amount of water still showed reasonable statistics.

The values of the intercepts and slopes for these formulae are different for each filter and each different FOV. For example the values of the slope of the Tsky versus PWV range from 0.7 to 0.8 for the G15 filter to 0.9 to 1 for STD filter. On the other hand, slopes of the Tsky versus Ta are confined to a smaller range, from 0.6 to 0.8.

Filter and FOV	Formula	R^2 %	RMS ^{O}C	MBE ^{O}C
STD 3^o	Tsky = - 27.8 + 0.96 PWV (4.6)	77	2.6	0.05
	Tsky = - 27.8+0.63 Ta (4.7)	82	0.48	0.04
STD 90^o	Tsky = - 20.0 + 1.06 PWV (4.8)	62	4.6	-0.19
	Tsky = - 21.7 + 0.80 Ta (4.9)	78	3.6	0.03
G15 3^o	Tsky = - 26.3 + 0.88 PWV (4.10)	73	3.15	0.02
	Tsky = - 29.3 + 0.74 Ta (4.11)	80	2.7	0.02
G15 90^o	Tsky = -15.6 + 0.70 PWV (4.12)	50	4.9	0.05
	Tsky = -19.18 + 0.69 Ta (4.13)	70	3.9	-0.05

Table 4. 2: Gives a summary of the one variable regression for the hourly measured, functional forms, sky temperature and its associated statistical parameters(correlation coefficient R^2, RMSE and MBE) for both G15 and STD detectors with 90^o and 3^o FOV. Sky temperature, Tsky, *and air temperature,* Ta, *are in ^{o}C and the PWV mm.*

4.3.2 Two Variables Models

Multiple regression analyses between the sky temperature and both the air temperature and the PWV were carried out. The reason of doing this is to find a model (having two physical variables) that can describe the IR clear sky temperature with good performance and minimize the errors found by using a single variable model. The analytical forms, the modelled-to-measured statistical variables of RMSE, MBE and correlation coefficients of two variable models are given in table (4.3). The use of two variables further optimized the predictions. It can be seen, for example, by comparing results from tables (4.2) and (4.3), that two variable models clearly give better results

than the one-variable model. The correlation coefficient for both filters with 3^o FOV was 93 %, with a RMSE of less than 2 ^oC. This is really surprising since this is within the range of the estimated instrumental and measurement errors of the meteorological variables.

The statistics of filters with 90^o FOV were poorer. They are not greatly different from those found in using one variable model. There is no clear explanation for this result. However, their *average* predicted temperatures are not far from those measured.

For many applications the 3^o FOV detectors can be used with good estimation and accuracy as we shall see later.

Filter FOV	Formula	R^2 %	RMSE ^oC	MBE ^oC
STD 3^o	Tsky = - 31.7 + 0.45 Ta + 0.63 PWV (4.14)	93	1.5	0.16
STD 90^o	Tsky = - 25.2 + 0.65 Ta + 0.55PWV (4.15)	83	3.2	0.015
G15 3^o	Tsky = - 33.0 + 0.58 Ta + 0.63 PWV (4.16)	93	1.6	0.04
G15 3^o (340)	Tsky = - 31.8 + 0.53 Ta + 0.60 PWV (4.17)	96	1.1	-0.01
G15 90^o	Tsky = - 20.2 + 0.61 Ta + 0.22 PWV (4.18)	72	3.9	0.01

Table 4. 3: Same as table (4.2) but multiple regression results are presented here. The G15 (3^o) 3^{rd} row is the parameterization based on the whole 662data points. The 4^{th} roe is the parameterization based on 340 data points. (see text for details).

.3.3 Validation of the Model (G15 with 3^{o} FOV)

Equation (4.16) for G15 (3^{rd} row in table (4.3)) was based on the whole data set. However, in order to produce more reliable and accurate model, the data set was divided into two groups. The first was for the parameterization and the second for the validation.

The first data (*set1*) includes 340 data points cover the period from September 2002 to June 2003. Multiple regressions analysis was carried out on *set1* and its results are found in the 4^{th} row of table (4.3), equation (4.17). Although, equations (4.16) and (4.17) do not differ largely from each other in term of their coefficients the performance of equation (4.17) shows better statistical results than equation (4.16). Therefore equation (4.17) was adopted here to be the final model for predicting the clear sky temperature using the (PWV, Ta) for the G15 detector.

Figures (4.3) and (4.4) show the estimated clear sky temperatures based on the equation (4.17), plotted against the measured sky temperature for *set1* and for the whole data set respectively.

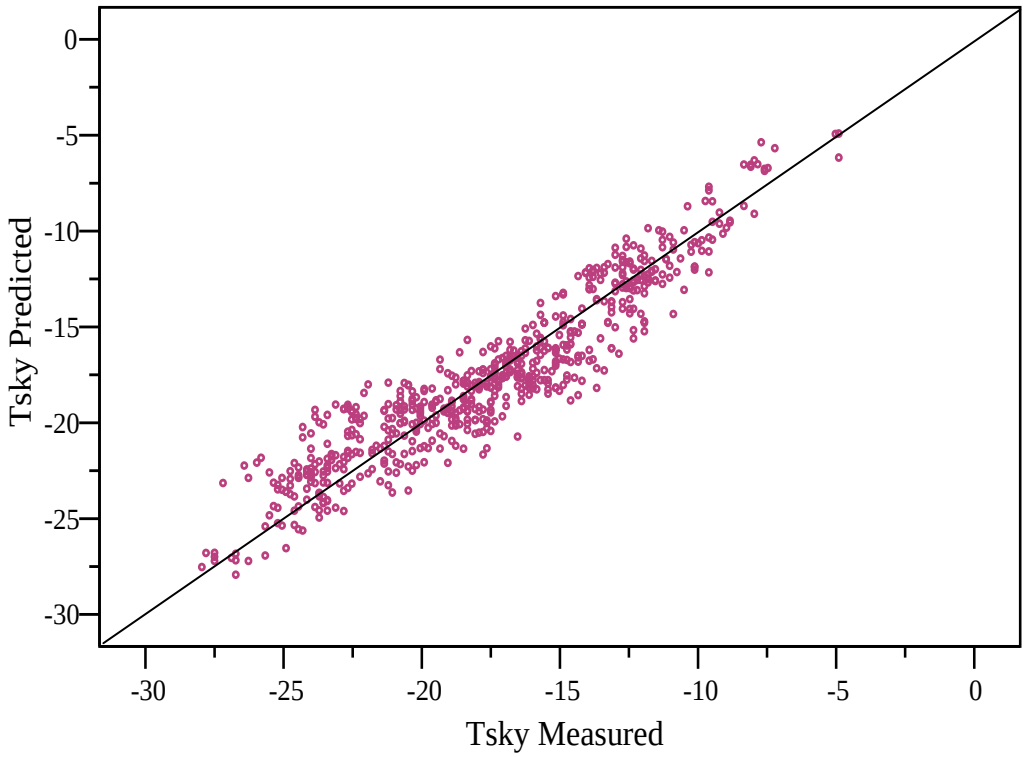

Figure 4. 3: Comparisons between measured and predicted sky temperatures for the G15 detector (both in ^{o}C) using equation (4.17) for data set 1. The straight line is 1:1 line for reference.

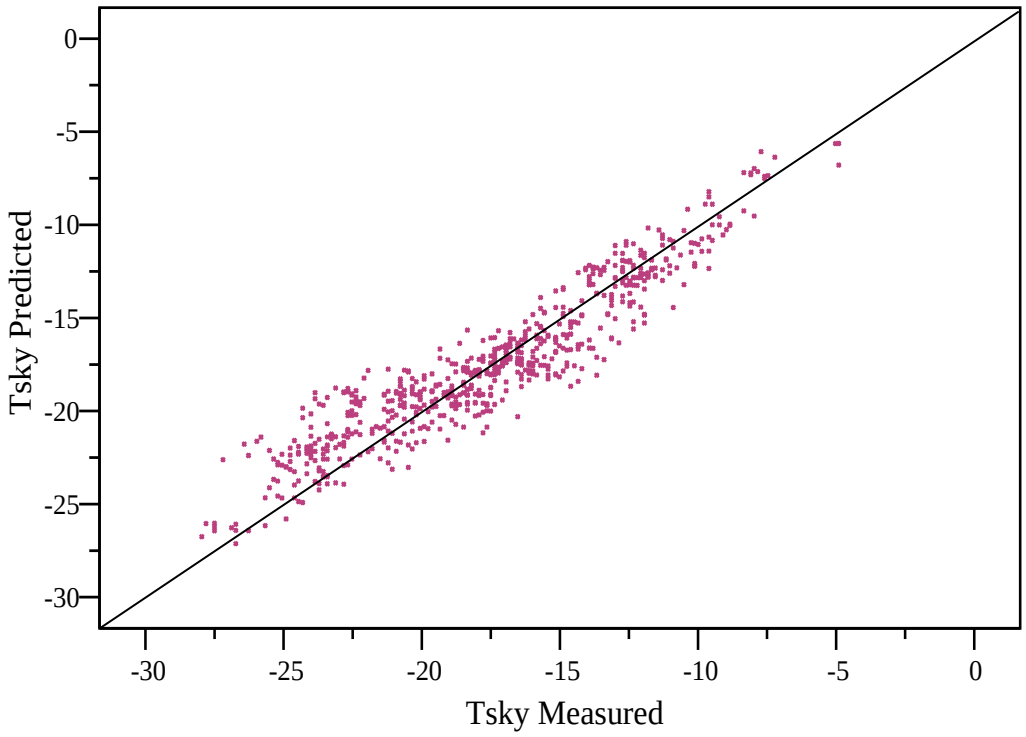

Figure 4. 4: *Same as figure (4.3) but for the whole data points.*

It is clear from both figures that the model is able to predict the clear sky temperature with good accuracy and less scatter than that found, for instance, in figure 4.2.

The performance of equation (4.17) was further validated. This was achieved by using an independent dataset. The additional data set covering the period from July 2003 to July 2004, excluding the period from September to December 2003, when there were no GPS data available. This data include 322 points and will be called *set2*.

It was used as an independent verification of the resulting model. This is shown in figure (4.5), whilst covering a limited range of measurements, confirms the ability of the model to predict clear sky temperatures with less scatter and good accuracy.

The linear relationship between the observed (whole data points) and predicted values (equation 4.17) of the sky temperatures was also statistically tested based on a simple linear regression test at a significance level of $\alpha = 0.05$, where α is one minus the confidence interval which in this test equals 95 %. The equation of the regression was:

$$Tsky\ Predicted = 0.9884\ Tsky\ Measured - 0.2463 \qquad (4.19)$$

and has a correlation coefficient of 94 % . This result indicates that the overall regression was statistically significant and the slope was close to unity (0.988 in this case), suggesting a strong 1:1 relationship between the predicted and the observed sky temperature. Figure (4.6) shows the frequency distribution of the errors (MBE) between the measured and predicted values superimposed on the normal distribution curve. The distribution has a mean of 0.01 and a standard deviation of 1 which matches very well that of the normal distribution.

From these results we conclude that precipitable water vapor and air temperature are both, as companion variables, very good predictors of the sky temperature. The theoretical justifications of this conclusion will be discussed more in chapter 6.

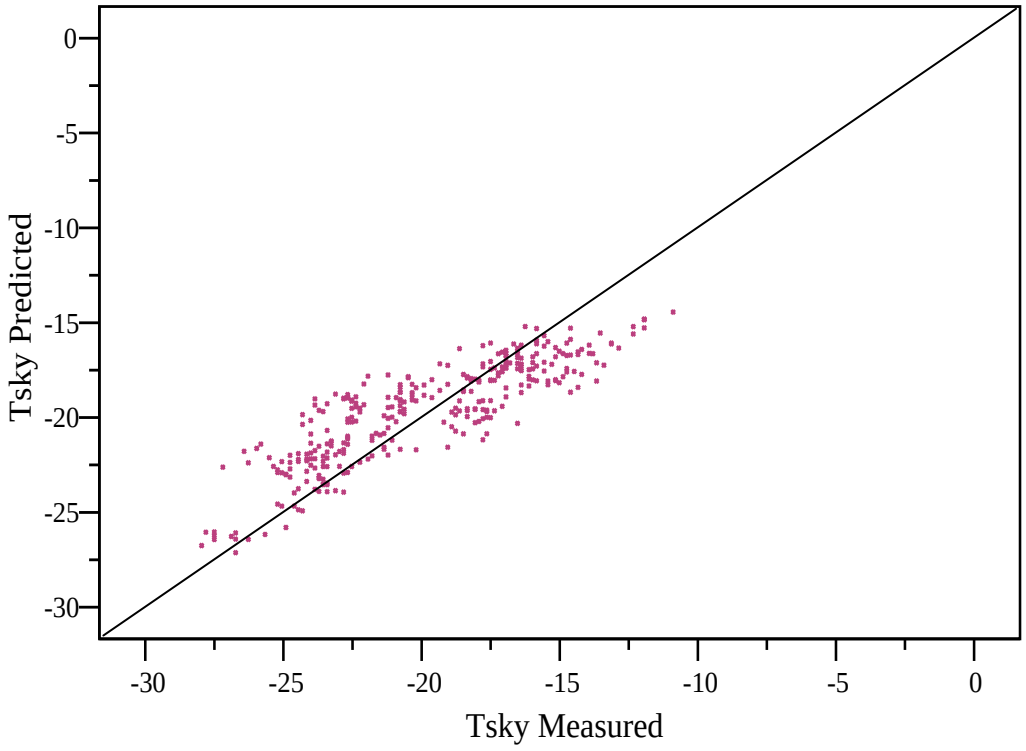

Figure 4. 5: *Same as figures (4.3) and (4.4) but for data set2, 322 points.*

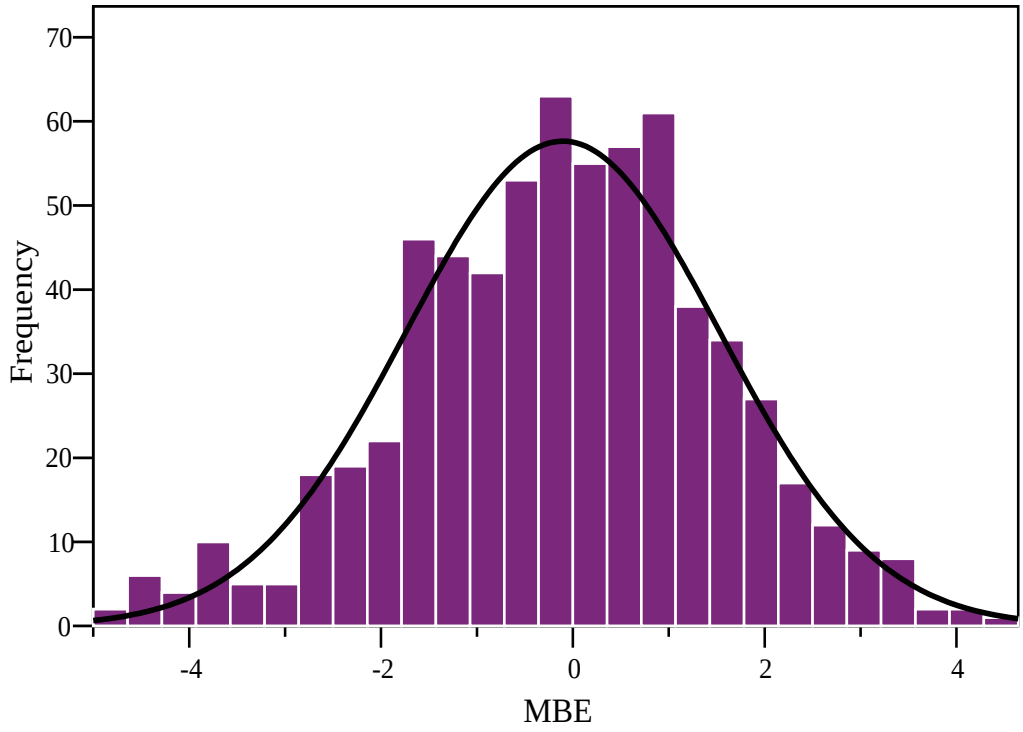

Figure 4. 6: *Histogram shows the frequency distribution of the MBE (^{o}C) of the measured – predicted sky temperature superimposed on the normal distribution curve using equation (4.17) for the whole data set.*

4.4 Determination of PWV Using Our Cloud Detectors

As we mentioned in chapter 2 water vapor is the most important variable of the major constituents of the atmosphere. It plays a crucial role in atmospheric processes that act over a wide range of temporal and spatial scales, from global climate to microclimatology.

Quantifying the amount of water vapor is desirable and would be very useful in atmospheric research and meteorology. The amount of water vapor in the atmosphere can vary considerably depending on the prevailing conditions including the time of the day, wind direction and temperature. This makes quantifying the amount of water vapor extremely difficult. The detection and estimation of water vapor in the atmosphere has been attempted over a long period of time with generally limited accuracy. Until recently, poor knowledge of the water vapor distribution in the atmosphere limited the accuracy of global climate models and precipitation forecasts, Bevis *et al*. (1992).

The standard techniques for measuring the actual amount of atmospheric water are radiosonde, ground-based water vapor radiometers, space–based radiometers attached to

weather satellites, LIDAR systems and, recently, GPS satellites. However, many limitations for using each one have been found. For example, price limits the use of LIDAR measurements (Solheim et al. 1998). Low spatial resolution, and the limited coverage of a relatively small number of sites, limits the use of space-based instruments and radiosondes respectively.

It was not the subject of this project to explore the techniques used to measure the atmospheric PWV, nor to calculate it. However, the results found in the previous section encouraged us to examine our radiometers as an inexpensive and reasonably accurate ground-based tool, which could be used to quantifying the atmospheric water vapor. This is also an encouraging area for future research for those who are interested in this subject.

Recall the results from the previous section; equation 4.17 can be reversed, using the PWV as a dependent variable and the measured sky and air temperatures as independent variables. It can be written as:

$$PWV = \frac{Tsky + 31.8 - 0.53Ta}{0.60} \tag{4.20}$$

The physical reason for this relationship is, as we discussed in chapter 2, that the emission by atmospheric water vapor covers part of the spectral response of our detector, which is consequently related to the ground temperature.

Figure (4.7) shows comparisons between hourly measured and predicted values of PWV using equation (2.20) for data *set1* (used to produce 4.17 and consequently 4.20). The RMSE for this parameterization was about 1.88 mm, the MBE was -0.12 mm and the modeled-to-measured correlation coefficient was 85 %. Figure (4.8) shows the frequency distribution of the MBE superimposed with that of normal distribution.

In figure (4.7) the data are spread evenly about the 1:1 line with a maximum of 2 standard deviations. It also shows that some of the predicted values, especially for those of low measured PWV values, are unphysical and give negative values. This may be due to the measurements errors in the PWV. The regression analysis between the measured and predicted values of the PWV (figure 4.7) gives a slope of 1 and an intercept of 0.015 ^{o}C. The frequency distribution of the bias presented in figure (4.8) is not far from the ideal normal distribution with mean of zero and standard deviation of 1.

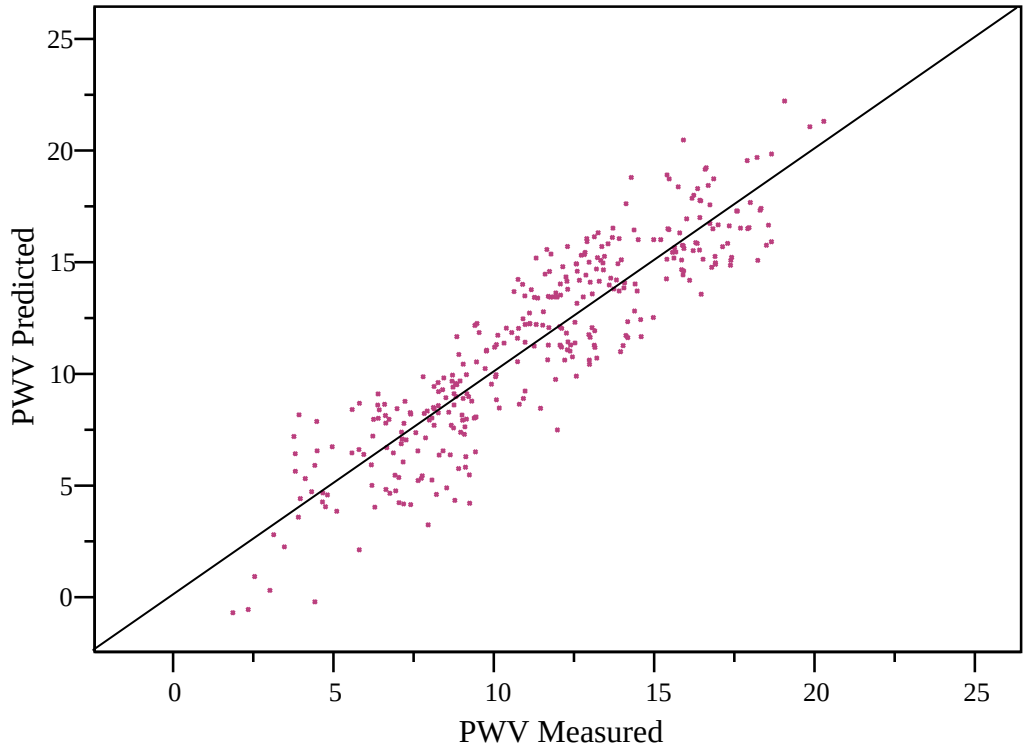

Figure 4. 7: Comparisons between predicted (equation 4.20) and measured hourly values of PWV in mm, for data set1 for G15 detector. The straight line is a 1:1 line for reference.

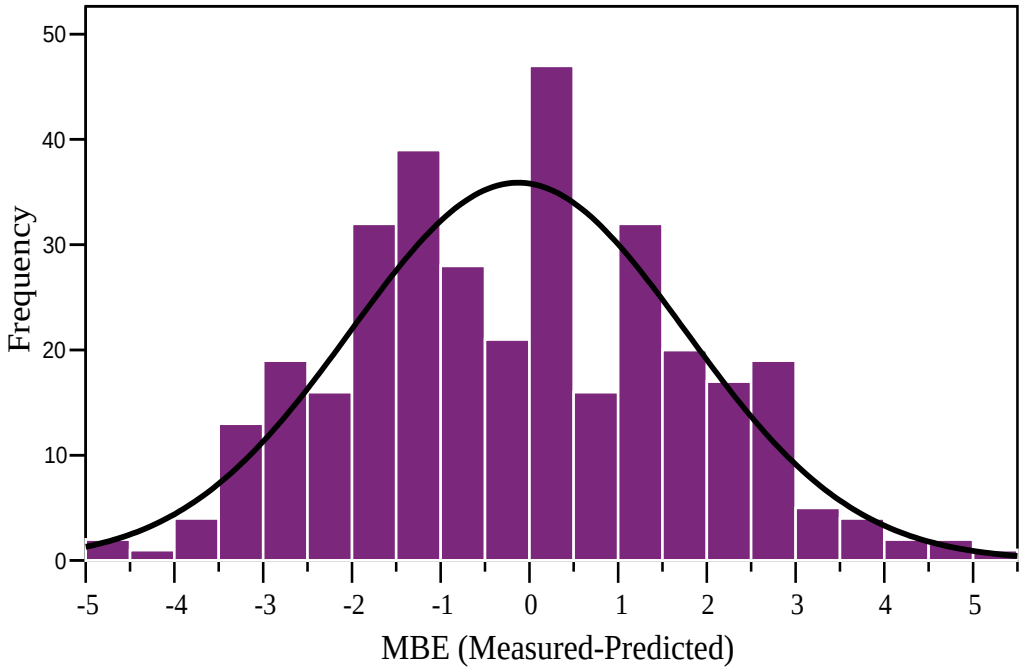

Figure 4. 8: Histogram shows the frequency distribution of the MBE (mm)of the Measured – predicted PWV superimposed on the normal distribution curve using equation (4.20) for the set1.

The validations of the above equation were carried out in two different ways.

Firstly, the predicted PWV were compared with the available radiosonde data during the same period of time when the GPS experiment was conducted. Since we are limited to clear night-time skies, 64 coincident measurements between radiosonde and GPS were found. Comparisons between GPS measured PWV and integrated radiosonde PWV values for the 64 points show an average bias of about 2.8 mm. This difference may be due to the spatial variability of water vapor. Apart from this bias, the predicted values from our model followed those predicted by the GPS.

Figure (4.9) shows the radiosonde measured PWV against those predicted by equation (4.20) for the 64 data points. The average MBE and RMSE between the two methods were 1.4 mm and 3 mm respectively. The model-to-measured correlation coefficient between the two values was 75%. The data points fall close to the vicinity of the 1:1 line. This result shows the ability of IR technique produced model to produce PWV with no worse uncertainties than the radiosonde measurements.

The *second* procedure used to validate the model is to use an independent data set, which is in this case called data *set2*. This data set covers reasonable values of PWV from less than 1 mm to about 20 mm. Figure (4.10) shows the estimated PWV values based on the model against the 322 data points measured by the GPS. The linear relationship between the two values was statistically tested based on a simple linear regression test. The results indicated that the MBE and RMSE of the predicted PWV using the proposed models were 0.50 and 3.4 mm respectively. The graph shows that the model broadly fits the measured values. The model under or overestimates some of the measurements but by no more than 2 standard deviations. These biases may be due to the spatial differences between the two sites, or error in the measurements of the PWV. However, the model can reasonably predict the PWV within the range of uncertainty of those values measured either by the GPS or by the radiosonde. It is worth noting that these biases are within the range of the acceptable values used in weather forecast predictions.

Extended investigations for daytime measurements, cloudy and overcast skies days and nights are highly recommended for further studies. These investigations may then fit data over wider ranges of PWV than those covered in this study. This will ensure a promising future for a new simple inexpensive method of measuring and continuously monitoring the atmospheric water vapor.

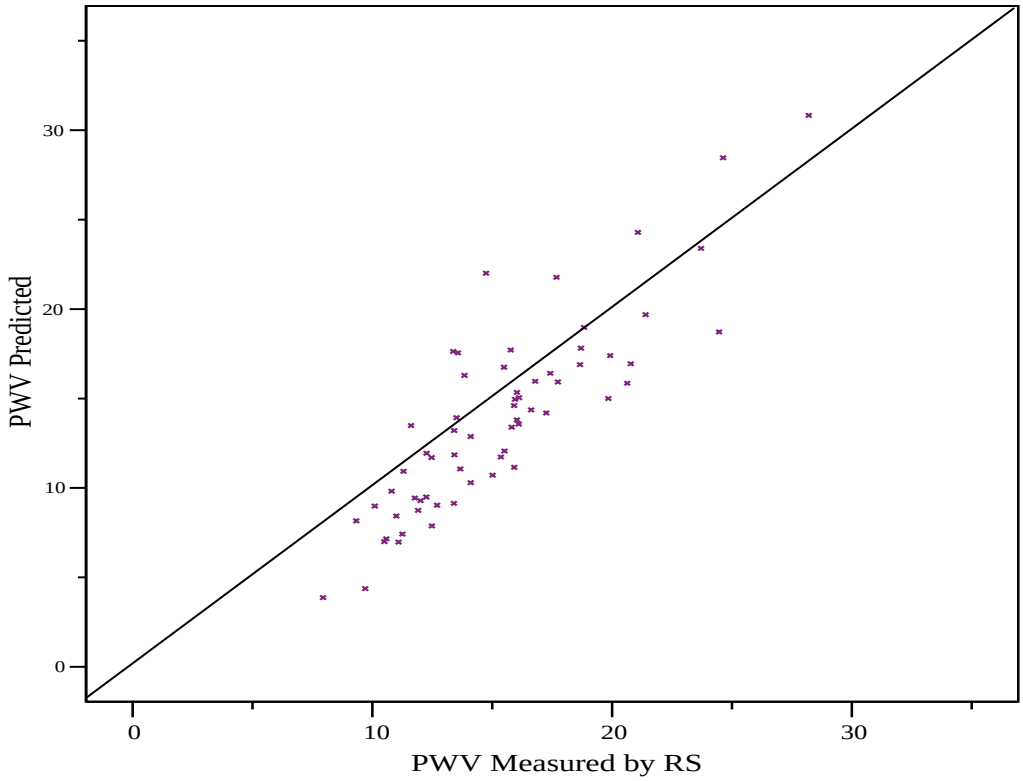

Figure 4. 9: Comparisons between integrated PWV measured by radiosonde, and the predicted values, equation(4.20), of PWV (both in mm). The straight line is a 1:1 reference line.

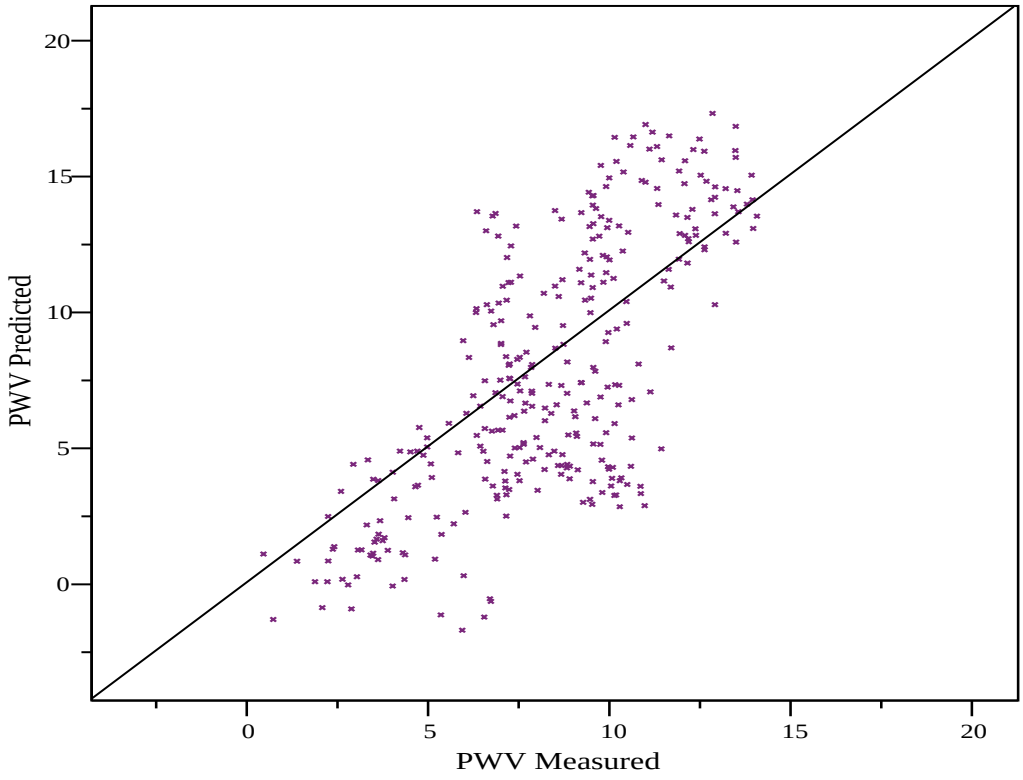

Figure 4. 10: Comparisons between predicted and measured hourly values of PWV in mm, for data set2 for the G15 detector. The straight line is 1:1 line for reference.

4.5 IR Clear Sky Temperatures Correlated With Ground Level Parameters

The results of section 4.4 have shown that the equations in table (4.3) are capable of providing accurate and consistently reliable estimations of clear sky temperatures, using the total amount of water vapor, PWV, and screen temperatures. The availability of direct measurements of the PWV can be a major limitation in using the proposed schemes. It is more desirable to make use of a formula that relies on conventional, and more generally available, ground meteorological measurements. It is important however, that such a formula retains a high accuracy in fitting the sky temperatures.

In this section an alternative simple and accurate formula for predicting the clear sky temperatures, utilizing simple measurable ground level parameters is developed.

The procedures utilized here in treating and analyzing the data are similar to those discussed in chapter 3 and followed in the previous section.

Firstly, linear regressions correlations between the sky temperature and the ground level parameters were established. The data collected and used for the purpose of this study are those of sky temperature measurements, and meteorological variables discussed in the previous chapter. Vapor pressure is calculated using equation (3.18). The data covered the period from July 2001 to September 2005, excluding the downtime periods for some detectors as discussed above. The main statistical parameters for all the variables used in this study are given in table (4.4).

It is evident from the table that the data cover a reasonable spread of atmospheric conditions and sky temperatures during the period of study. Due to Adelaide's closeness to Mediterranean climatic conditions, no extreme weather or severe variability was found among the data set over the whole period. This is in contrast to those found, for example, at the Riyadh site in Saudi Arabia as we shall see later. Also the data in the table exhibited a wider range of air and sky temperature measurements in comparison with those used in the previous study, (table 4.1).

For the same reasons discussed before, results from the G15 detector with 3^o FOV will be considered here.

STD (N = 1017)					
	Range	Minimum	Maximum	Mean	Std. Deviation
Ta (^{o}C)	27.20	2.40	29.60	13.59	5.36
Tdew (^{o}C)	23.90	-5.00	18.90	6.91	2.97
RH(%)	86.00	11.00	97.00	68.29	17.64
eo (mb$^{0.5}$)	17.58	4.22	21.80	10.13	2.10
Sqrt(eo) (mb)	2.62	2.05	4.67	3.17	0.32
Tsky 90^o FOV (^{o}C)	39.29	-28.96	10.32	-8.33	6.12
Tsky 3^o FOV (^{o}C)	34.89	-33.95	0.94	-17.38	5.50
G15 (N = 1341)					
	Range	Minimum	Maximum	Mean	Std. Deviation
Ta (^{o}C)	27.40	2.40	29.80	14.18	5.46
Tdew (^{o}C)	36.20	-6.60	29.60	9.32	5.72
RH(%)	86.00	11.00	97.00	65.10	18.90
Sqrt(eo) (mb$^{0.5}$)	18.07	3.73	21.80	9.93	2.12
Sqrt(eo) (mb)	2.74	1.93	4.67	3.13	0.33
Tsky 90^o FOV (^{o}C)	30.70	-20.22	10.47	-8.00	5.03
Tsky 3^o FOV (^{o}C)	29.94	-28.90	1.05	-18.85	5.17

Table 4. 4: Overall statistics for clear sky night-time values during the period of study of some of the important meteorological parameters: air temperature (T_a), dewpoint temperature (Tdew), Relative humidity (RH) square root of vapour pressure (eo in mb) and its square root (Sqrt(eo)) and the measured sky temperature (Tsky) for STD and G15 filters with 3^o FOV and 90^o FOV.

Figure (4.11) shows the variations of the sky temperature against the air temperature, Ta, and the square root of vapor pressure (*Sqrt (eo)).* The sky temperature has a pronounced positive dependency on Ta over the whole range of temperatures. Water vapor pressure showed a general positive trend with the sky temperature. That is, an increase of sky temperature is associated with increasing the amount of vapor pressure. This relation is physically expected. However, the degree of correspondence is variable. For example between the values of 2.5 mb$^{0.5}$ to 4 mb$^{0.5}$, although with some spread due to data clustering, the sky temperature correlates very well with the vapor pressure. On the other hand, between 4 mb$^{0.5}$ and 5 mb$^{0.5}$ the relation flattens and no further clear trend stands out. At values below 2.5 mb$^{0.5}$ the relation is rather poorer and this relation may not be totally clear or maybe at some values disappears.

A single variable linear regression analysis between the sky temperature and the Ta and the *Sqrt (eo)* was conducted. Table (4.5) includes the algebraic forms, correlation coefficients and the RMSE of this regression. It shows that the statistics of the ground

level vapor pressure for all filters and FOVs are poorer than those found using the PWV, table (4.2), which is the real measure of the atmospheric water content. The intercepts and the slopes for the water vapor coefficients in the sky temperature relationship are different from one filter to another and from FOV to another. This is in contrast to that found for the PWV as a single variable. On the other hand, air temperature shows better statistics, with no RMSE greater than 4 ^{o}C when correlated with the sky temperature. Comparable values of intercepts and slopes with some of those found in table (4.1) for the same variable were found.

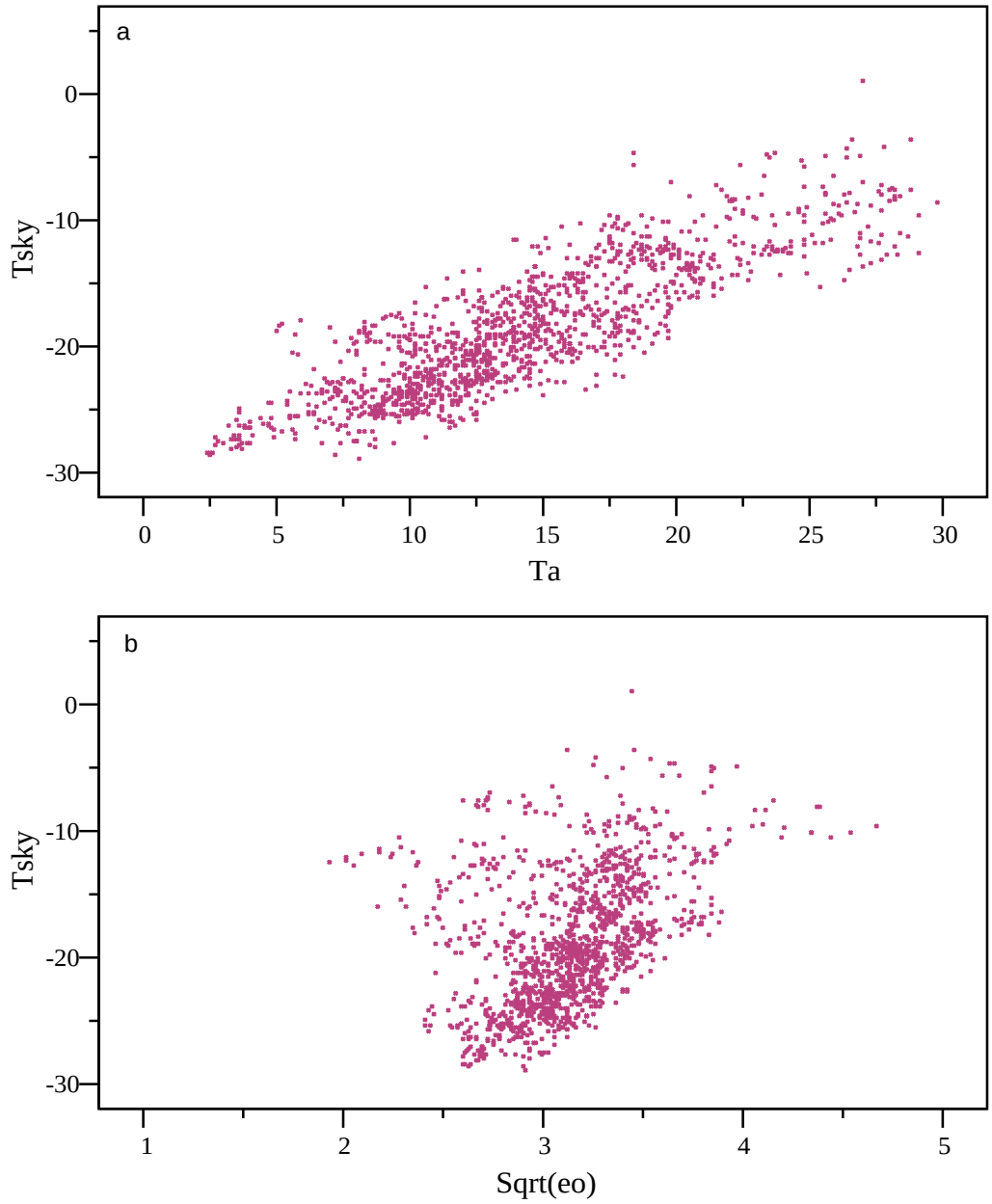

Figure 4. 11: Shows the relationship between the hourly sky temperatures (in ^{o}C) and,(a) air temperature, Ta, and (b) square root of vapour pressure Sqrt(eo) ($mb^{0.5}$).

Filter and FOV	Formula	R^2 %	RMS ^{O}C
STD 3^o	Tsky = - 42.6 + 8.0 Sqrt(eo) (4.21)	55	5
	Tsky = - 29.2+0.87 Ta (4.22)	86	2.9
STD 90^o	Tsky = - 33.2 + 7.8 Sqrt(eo) (4.23)	42	5.6
	Tsky = - 19.9 + 0.84 Ta (4.24)	74	4
G15 3^o	Tsky = - 39.2 + 6.5Sqrt(eo) (4.25)	42	4.7
	Tsky = - 30.3 + 0.8 Ta (4.26)	85	2.7
G15 90^o	Tsky = -17.9+3.2Sqrt(eo) (4.27)	35	5
	Tsky = -16.0 + 0.56 Ta (4.28)	62	3.9

Table 4. 5: Summarizes the one variable regression analysis and its associated statistical parameters for both detectors in their hourly measurements. The sky temperature, Tsky, and air temperature, Ta, are in ^{o}C and the square root of vapour pressure ,Sqrt(eo), in $mb^{0.5}$.

Multiple regression analyses between the sky temperature and the two variables (Ta, sqrt(eo)) together were carried out for the two filters with their FOVs. The functional form, R^2, RMSE and MBE of the regression results are summarized in table (4.6).

Although there is not much improvement in the performance of the two variable models for the 90^o FOV detectors, the two variables approach is giving better results for the 3^o FOV detectors than the one variable. The RMSE for the 3^o FOV detectors were between 2.1 ^{o}C to 2.7 ^{o}C. It is worth mentioning that the parameterization results presented in the table are based (except fourth row, see below) on the whole set of data points.

The Parameterization for the sky temperatures measured with the G15 detector (3^o FOV) was achieved in two ways. The first was done by applying the two parameter fits to the whole data points and its results showed in the 3^{rd} row of the table.

The second was obtained by dividing the data into two groups. This first was used for the parameterization and the second for the validation. The first set (*set1)* contains 649 data points covering period from July 2001 till October 2003. The second (set2) covers period from November 2003 till July 2005 and containing 693 data points. The results of the parameterizations based on data set1 are given in the 4^{th} row of table (4.6).

Filter and FOV	Formula	R^2 %	RMSE ^oC	MBE ^oC
STD 3^o	Tsky = - 39.2 + 0.79 Ta + 3.5 Sqrt(eo) (4.29)	87	2.7	0.0
STD 90^o	Tsky = - 29.8 + 0.78 Ta + 3.4 Sqrt(eo) (4.30)	77	3.9	0. 15
G15 3^o	Tsky = - 40.9 + 0.75 Ta + 3.6 Sqrt(eo) (4.31)	88	2.4	0.13
G15 3^o (649)	Tsky = - 43.9 + 0.75 Ta + 4.6 Sqrt(eo) (4.32)	91	2.1	0.0
G15 90^o	Ts = - 19.3+ 0.54 Ta + 1.1 Sqrt(eo) (4.33)	62	3.9	0.19

Table 4. 6: Summarizes the two variables regression and its associated statistical parameters for both detectors in their hourly measurements The G15 (3^o), 3^{rd} row is based on the whole data set, while the 4^{th} row is based on 649 data point. see text for details.

Figure (4.12) shows the predicted sky temperature against the measured for this data set. It shows that the model is performing well in predicting the sky temperature to within a maximum of 1 standard deviation and the data are spread by this amount around the 1:1 line. Figure (4.13) shows the MBE distribution superimposed on that of normal curve. It shows that, although there are higher biases between the measured and predicted using the model, equation (4.32), the distribution is not far from that of the ideal curve.

This model was then assumed to be the preferred model for the G15 detector with 3^{o} FOV.

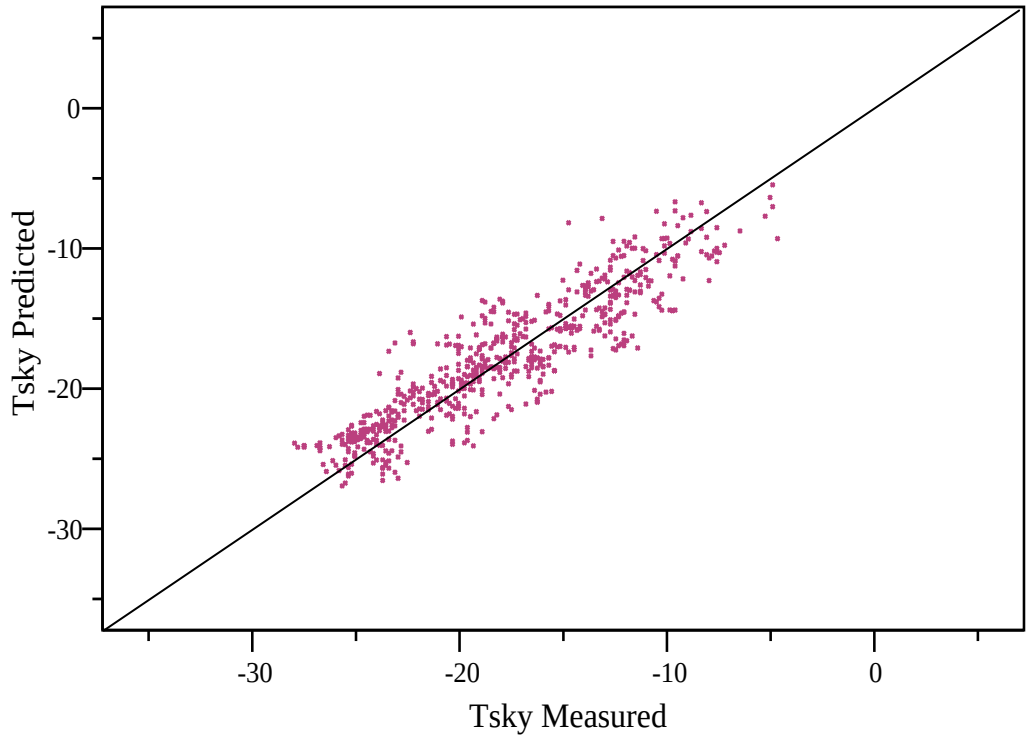

Figure 4. 12: Comparisons between measured and predicted (equation 4.32) sky temperature for the G15 detector (in ^{o}C) using set1. The straight line is a 1:1 line for reference.

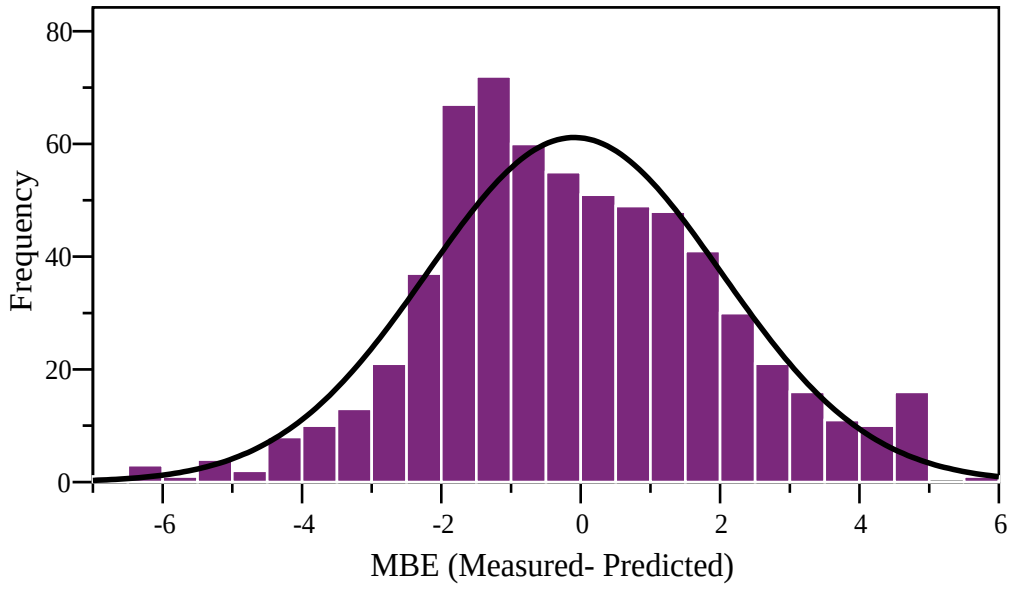

Figure 4. 13: Shows the frequency distribution of the MBE (in ^{o}C) of the Measured – predicted (equation 4.32) sky temperature superimposed on the normal distribution curve for data set1.

Figure (4.14) shows a comparison between the predicted sky temperature using equation (4.32) and measured values for data set2. It tests the applicability of the model in predicting sky temperature from different data set. The MBE, RMSE and R^2 between the modeled and measured values were 0.1 ^oC, 2.7 ^oC and 82 % respectively. Even though there is overestimation and underestimation in some particular situations, the model in general was able to predict the sky temperature over different conditions with reasonable to high accuracy. Figure (4.15) shows the frequency distribution of the bias and gives us an indication about the accuracy of the model.

Theoretical justifications for this model will be developed in chapter 6, using MODTRAN software

In general, the results obtained in this section are not as good as those found in the previous section where the sky temperature was parameterized using the air temperature and the PWV. Part of the reason can be explained by the fact that the PWV is a more appropriate variable and direct estimator of the total amount of the water in the atmosphere. The screen level vapor pressure is not always representative of the real integrated water vapor conditions.

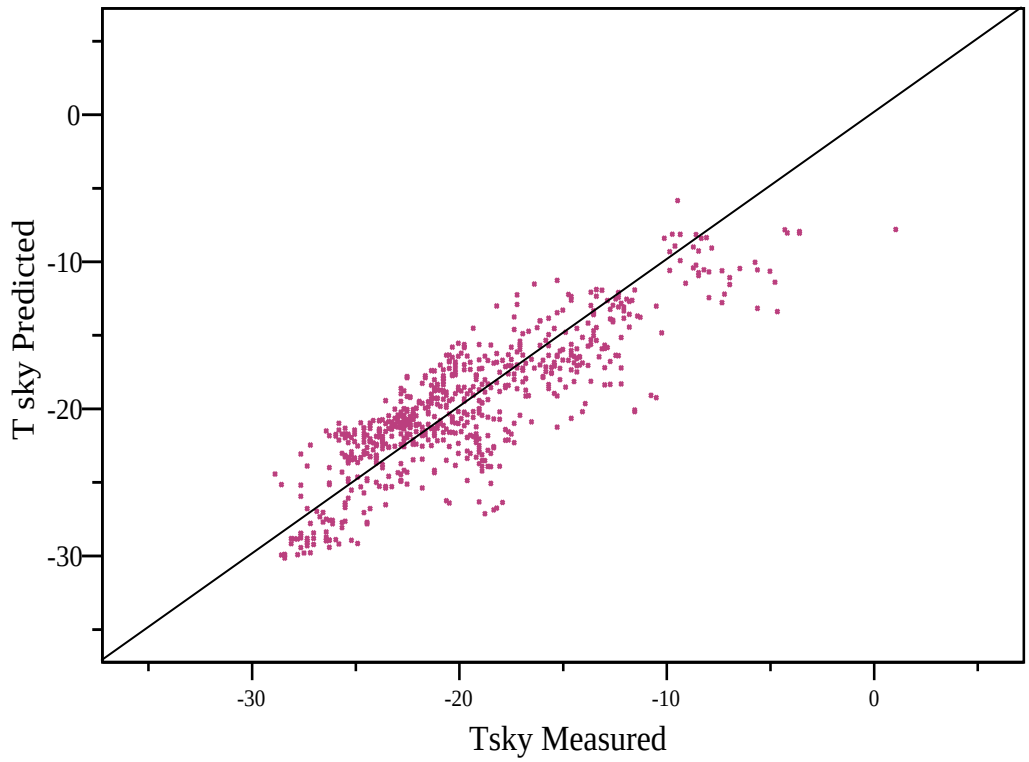

Figure 4. 14: Same as figure (4.12) but for the data set2. The sky temperatures are in ^oC.

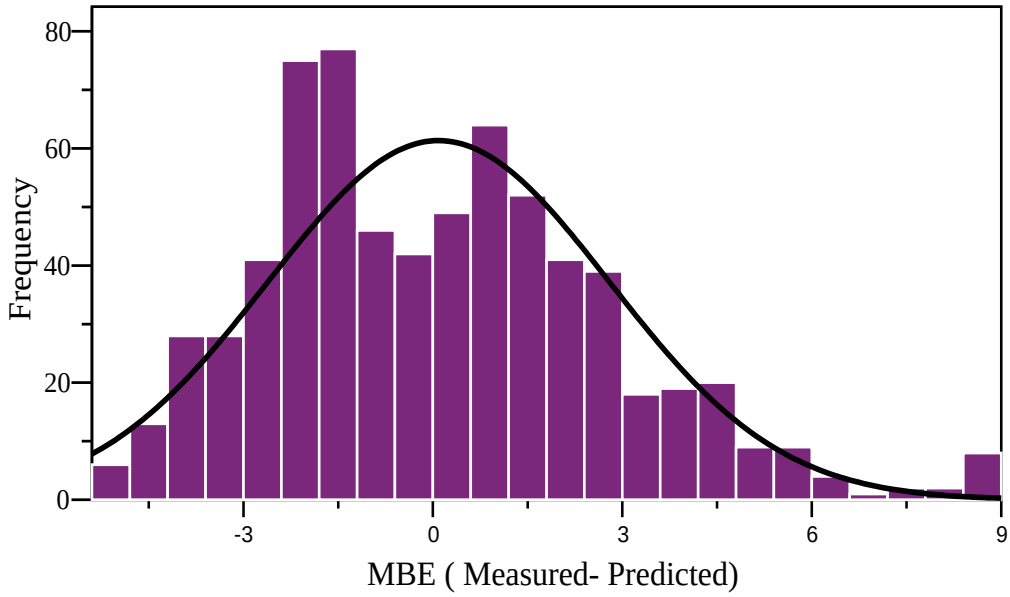

Figure 4. 15: Same as figure (4.13) but it shows the frequency distribution of the MBE (in ^{o}C) of the Measured – predicted sky temperature using equation (4.32) for data set2.

4.6 Comparisons between Observations, Modeled and Some Bulk Formulae

This section presents a comparison between the predictions of some IR clear sky models found in the literature with hourly clear sky temperature observations made with the G15 (3^{o} FOV) detector in Adelaide for the period between July 2001 September 2005. Comparisons between these formulae and the model produced by this study that uses the ground level variables (equation 4.32) will be also carried out.

Ten well-known models (Bulk formulae) were used in calculating the measured sky temperatures. Most of the authors of these formulae, for example, did not specify the range of wavelength and the FOV of their instrument. Prata (1996) did his calculations of IR clear sky emissivity for a single zenith angle of 53^{o}, which he claimed to be the representative angle for the whole hemisphere calculations. Others used hourly, some used daily, and some used monthly averages data for their calculations.

Throughout this thesis clear sky emissivity is calculated using these formulae with their original coefficients without any further considerations. The IR radiation is then

calculated using equation (2.23) which is then converted to sky temperatures using equation (2.22).

The statistical success in fitting observed data and the compatibility with the proposed model from this study (equation 4.32) are given in table (4.7). The functional forms of the formulae presented in the table were summarized in chapter 2.

The table is divided to three parts. The first presents the minimum, maximum and average prediction of these models. Similar statistical parameters for the measured and predicted (equation 4.32) temperatures are also given in this part of the table. The second part of the table shows the MBE and RMSE of the linear fit between the measured and calculated sky temperatures using these models. The third part contains MBE and RMSE of the comparisons between the predicted sky temperature using equation (4.32) and the sky temperature calculated using these bulk formulae. The results of the comparisons presented here are for the whole data set that has 1341 data points and their statistics are shown in table (4.4).

The statistical parameters presented in the table show that all the models either overestimate or underestimate the measured values of sky temperatures. None of these models gives a close to perfect prediction of the measured sky temperatures. The models of Efimofa (1961), Angstrom (1918) and Idso(1982) showed the worst performance with MBE and RMSE of about -18 ^{o}C. On the other hand, the models of Brunt (932) and Izmon *et al* (2003) (low-land values used here, see chapter 2) gave the lowest MBE and RMSE values. Similar results are found when comparing the proposed model (equation 4.32) with these formulae.

The unsuccessful predictions of these models to the measured sky temperatures in Adelaide do not mean that these formulae are inaccurate or incorrect. It means basically that these models were proposed in sites having, overall, different atmospheric conditions from those found in Adelaide. For example the model of Efimova (1961) was proposed from sites with low absolute humidity. This is an important point. As we shall later some of these models showed reasonable predictions when used in some sites in Saudi Arabia.

Because these are empirical models and were proposed for specific conditions, they can be optimized by modifying and adjusting the values of the constants to suite the atmospheric conditions in a desired site. Such adjustments were conducted by several authors; see for example Garcia (2004).

Model	Min	Max	Mean	Measured-Model		Predicted-Model	
				MBE	RMSE	MBE	RMSE
Measured Tsky	-28.90	1.05	-18.85				
Predicted Tsky eq. (4.32)	-29.74	-6.43	-18.98				
Brunt (1932)	-19.40	11.34	-5.43	-13.42	13.69	-13.55	13.62
Angstrom (1918)	-12.40	14.31	-0.32	-18.52	18.71	-18.66	18.69
Efimofa (1961)	-13.31	14.96	-0.43	-18.42	18.61	-18.55	18.59
Swinbank (1963)	-20.17	18.48	-3.74	-15.10	15.69	-15.24	15.64
Brutsaert (1975)	-18.42	11.86	-4.46	-14.38	14.64	-14.52	14.57
Berahal and Fromberg (1982)	-18.92	20.01	-4.60	-14.24	14.70	-14.38	14.71
Idso and Jackson (1969)	-17.56	19.36	-3.10	-15.74	16.26	-15.88	16.23
Idso (1982)	-13.09	14.40	-0.60	-18.24	18.42	-18.38	18.40
Prata (1996)	-16.66	11.90	-3.54	-15.31	15.53	-15.44	15.48
Izmon *et al*. (2003)	-18.77	10.01	-5.61	-13.24	13.49	-13.37	13.41

Table 4. 7: The first part (first 3 columns) summarizes the minimum, maximum and mean, values of the measured clear sky temperatures and those temperatures calculated with from 11 models including values predicted using equation (4.32), all temperatures are in ^{o}C. The second part (2 columns) shows the MBE and RMSE in ^{o}C between the estimated (using the bulk formulae) and measured clear sky temperatures while the third parts show the MBE and RMSE between predicted temperatures using equation (4.32) and the other models for the Adelaide site over the period under consideration with 1341 data points.

CHAPTER FIVE

ZENITH ANGLE DISTRIBUTION OF CLEAR SKY TEMPERATURES

5.1 Introduction

In the previous chapter we proposed models that are able to predict the clear sky temperature at the zenith with high accuracy. In this chapter we will extend our investigations to the dependence of sky temperatures upon the zenith distance. We will establish a reasonable zenith angle distribution model that can be used with good accuracy to predict the sky temperatures at any zenith angle.

Experimental work in investigating the variation of the IR atmospheric radiation as a function of zenith angle was established very early. It started as early as the work of Dines and Dines (1927). Other zenith angle investigations of the atmospheric radiation

were discussed in chapter 2 and more details can be found in the articles mentioned there.

The work presented here will investigate the zenith angle distribution of the IR clear sky temperature using measurements made by the Adelaide IR scanning cloud detectors over a period of more than four years.

5.2 Measurements and Data set

Half hourly clear sky data from the scanner detectors with STD and G15 filters were used for the purpose of this work. Clear sky times were selected using the criteria discussed in chapter 4. The data used here are from the periods when both scanners of G15 and STD filters were in use. Due to the similarities between both halves of a scan through the zenith, only scans from the zenith to the western horizon (one side) were used here. Identical results are expected to be applicable to the other side of the scans. The data were divided into two groups according to the availability of the meteorological variables. The first, *set1*, in addition to the sky temperature measurements has all the ground level meteorological variables available and covers the period from July 2001 to July 2005 with 963 data points. The second, *set2*, includes data for the period when the GPS experiment was running. This covers the period between November 2002 and June 2003 and has a total of 331 data points available when coincident G15 and STD detectors were in use.

Table (5.1) summarizes the statistical parameters for the meteorological variables and the sky temperatures at the zenith for the two groups.

The reason for dividing the data in this way will be clear later.

Set1 (N = 963)					
	Range	Minimum	Maximum	Mean	Std. Deviation
Tair (^{o}C)	27.20	2.40	29.60	13.83	5.46
Tdew (^{o}C)	23.90	-5.00	18.90	6.88	3.03
eo (mb)	6.84	4.22	21.80	10.01	0.11
Sqrt(eo) mb$^{0.5}$	2.62	2.05	4.67	3.16	0.33
Tsky STD (^{o}C)	28.66	-27.72	0.94	-17.41	5.22
Tsky G15 (^{o}C)	29.94	-28.90	1.05	-18.68	5.25
Set2 (N = 331)					
PWV (mm)	18.42	1.86	20.29	10.83	3.93
Tair (^{o}C)	25.90	5.10	31.00	16.94	5.04
Tdew (^{o}C)	25.50	-6.60	18.90	7.67	3.51
Tsky STD (^{o}C)	21.29	-26.02	-4.72	-16.39	4.32
Tsky G15 (^{o}C)	20.76	-25.67	-4.90	-15.86	4.42

Table 5. 1: Overall statistics for clear sky night-time of the meteorological variables and sky temperatures, Tsky, at the zenith for STD and G15 scanners.

5.3 Zenith Angle Temperature Variations

Figure (5.1) is a sample of one scan from the G15 and STD detectors and shows the variation of the sky temperatures at different zenith angles from the zenith to the horizon. For both detectors, the sky temperature increases very slowly on increasing the distance from the zenith. The temperature at an angle of 33^o is less than 2 ^{o}C warmer than that at the zenith. At an angle of 57^o the sky temperatures are warmer by 5 ^{o}C from those at the zenith. For zenith angles less than 60^o, the G15 filter is 2 ^{o}C colder than the STD filter and, in both cases, the temperature decreases slowly with increasing zenith angle. Only close to the horizon does the sky temperature measured by both detectors become very close to each other. Here, the temperature increases rapidly towards the full blackbody values, where the sky temperature is equal, or nearly equal, to the screen level temperature.

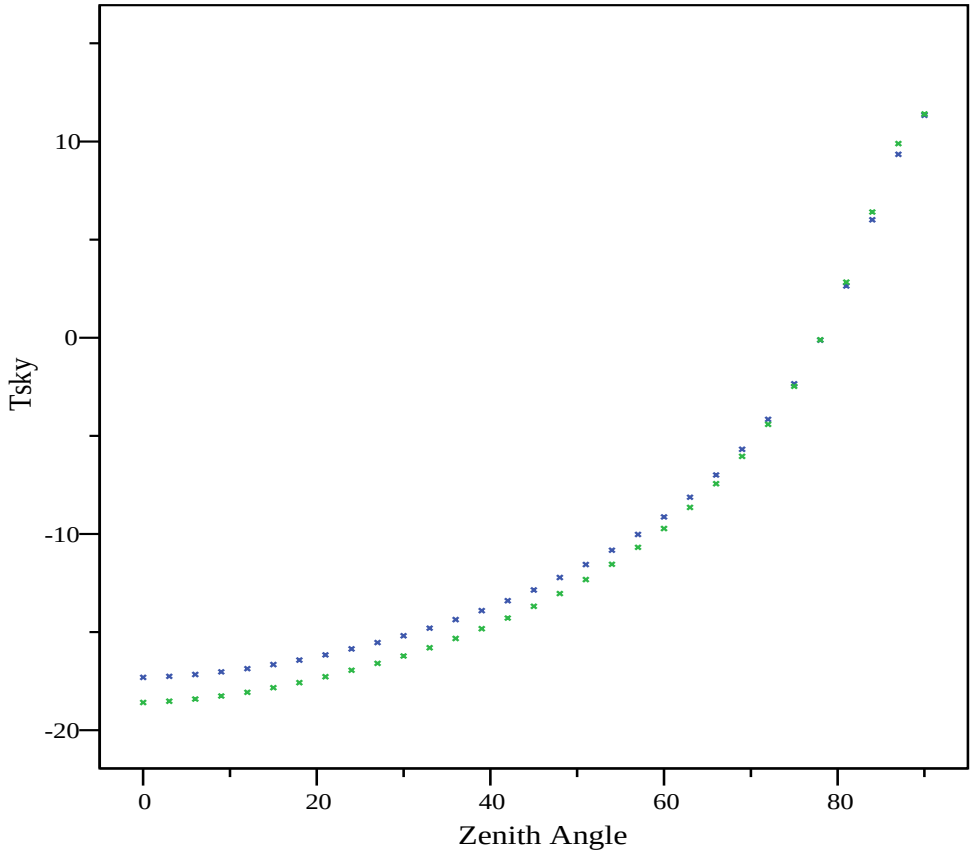

Figure 5. 1: Illustrating the variation of the clear sky temperature with the zenith angle from the zenith to the horizon for the STD filter (Blue) and for the G15 filter (Green). The sky temperature is in ^{o}C and the angles are in degrees. The screen temperature, vapor pressure and dew point temperature were 13.8 ^{o}C, 10 mb, and 6.8 ^{o}C respectively.

The purpose of the current study is to find an appropriate functional form for the dependence of sky temperature upon the zenith distance which can predict sky temperatures at any angle with reasonable accuracy.

Elsasser (1942) showed that the isothermal emission from water vapor and carbon dioxide varies linearly with the logarithm of the optical depth of water vapor. Consequently, in an isothermal atmosphere the emission of an air column at an angle θ from the zenith should increase linearly with the logarithm of $sec\theta$. Robinson (1947, 1950) and others showed that the same relationship is valid for a non-isothermal, real atmosphere, presumably because most of the atmospheric radiation originates within 100m of the ground.

Figure (5.2) shows the variation of the measured sky temperatures for the G15 detector against the logarithmic of secant of the zenith angle (ln $sec\theta$), for three selected scans

having different atmospheric conditions. These scans cover angles ranging from the zenith to 87°.

In spite of the extreme differences in atmospheric conditions between these three scans of the different sky temperatures at each zenith angle, the figure does show an excellent linearity in the relationship between the sky temperatures and the logarithmic of the *secant* of the zenith angle from the zenith to 3° above the horizon.

The linear correlation coefficients for the three scans were respectively 99, 98 and 97 % from the top to the bottom of the figure.

The linear fit of the sky temperatures with zenith angle for those scans can be expressed as:

$$Tsky(\theta) = a + b \times ln(sec\,\theta) \qquad (5.1)$$

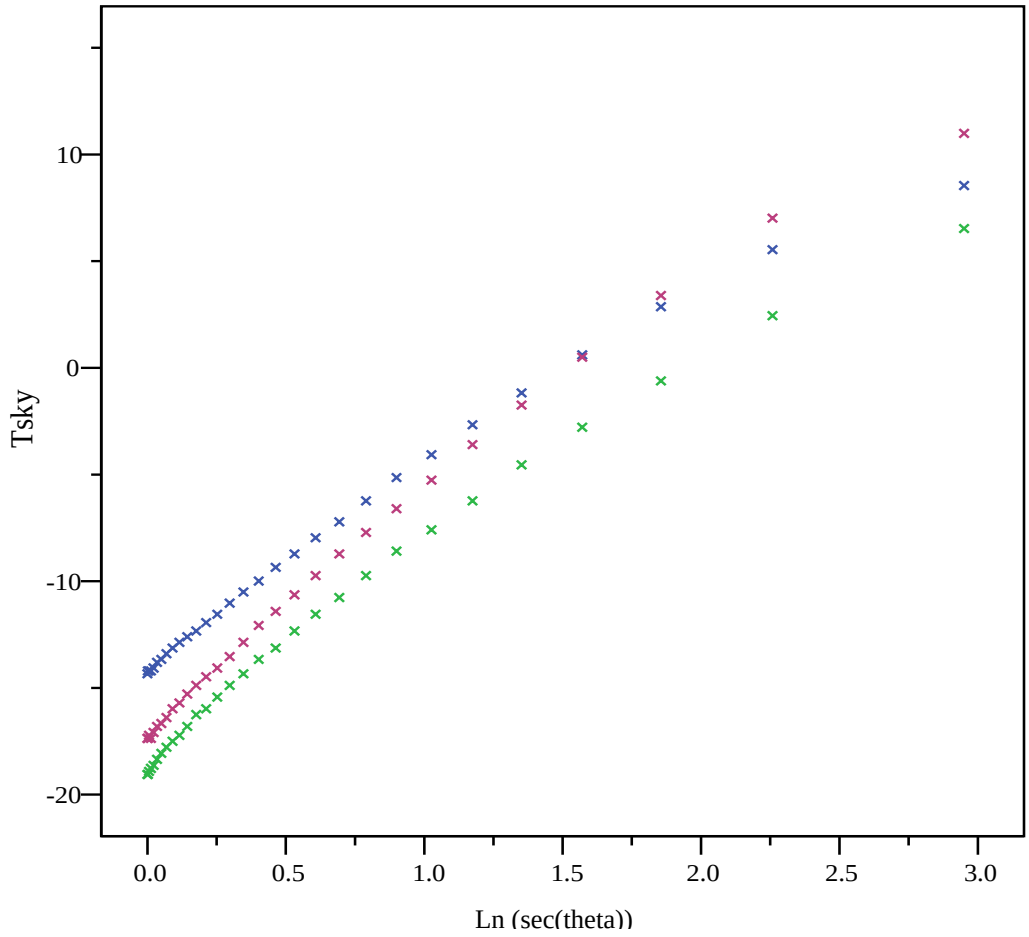

Figure 5. 2: Sky temperature (in °C) as a function of the logarithm of the secant of the zenith angle (ln sec theta) for angles from the zenith to 8 ° for some selected scans. Blue (Tair =13 °C, PWV 14 mm and, Tdew 7 °C),Green (Tair 18.7 °C, PWV = 4.5 mm and Tdew= 7 °C) and dark Pink (Tair = 16 °C, PWV =1.7 mm and , Tdew 11 °C).

In order to test the applicability of the above relationship between the two variables the whole dataset, 1294 data points, was used and the regression analysis done for every single scan.

Mathematica code was written to handle this task. The code was intended to do the following:

1. Read each scan individually from the zenith to 87^o.
2. Apply the calibration formulae (table 3.1) for each sky temperature at each zenith angle for each detector (i.e. G15 or STD filter).
3. Do the regression analysis between the sky temperature and $\ln(sec\theta)$. This step includes the calculations of the regression parameters e.g. *a* and *b* coefficients found in equation (5.1). It also calculates the statistics of this regression such as R^2, maximum minimum and the standard deviation.
4. For each scan, the code produces a plot similar to those in figure (5.2) with a regression line fitted to the data to observe the linearity of the fit.
5. The above steps from 1 to 4 were conducted for each scan and the desired outputs were kept.

The linear regression analysis for the total of 1294 scans was conducted using the above steps. The results showed that the relation between the sky temperature and the zenith angle have accurately the form of equation (5.1) with R^2 for all scans greater than 97 %. Table (5.2) shows some statistical parameters of the *mean* values of the intercept *a* and the slope *b* in equation (5.1) for the whole data set, 1294 data points, for both G15 and STD detectors. The data in the table were obtained by taking the averages of each value of the coefficients obtained for each scan. Clearly, the slope values were not significantly different between scans and have a narrow range of values. On the other hand, the intercepts values were significant and showed wider ranges.

Based on their statistical values from this study, the coefficients *a* and *b* in equation (5.1) can be replaced with their mean values found in the table for each filter to have an approximate model for predicting the clear sky temperature at any zenith angle from zenith to an angle of 87^o.

For example, at any zenith angle the clear sky temperature for the STD detector can be predicted as follows:

$$Tsky(\theta) = 9.74 \times ln(sec\,\theta) - 16.56 \qquad (5.2)$$

where *a* and *b* constants in equation (5.1) replaced by their mean experimental values obtained from the fits found in table (5.2). A similar functional form can be obtained for the G15 detector using the same procedure discussed above.

However, a more general form based on physical parameters is desired. This matter will be discussed in the following section.

Set1 (N = 963) G15					
	Range	Minimum	Maximum	Mean	Std. Deviation
Intercepts (^{o}C)	29.44	-27.94	1.50	-17.76	5.39
Slopes	6.21	8.26	14.47	10.41	0.77
STD					
Intercepts (^{o}C)	30.00	-27.09	2.91	-16.56	5.33
Slopes	9.33	7.10	16.44	9.74	.99
Set 2 (N = 331) G15					
Intercepts (^{o}C)	21.51	-25.11	-3.60	-14.93	4.52
Slopes	2.86	8.43	11.29	9.83	0.53
STD					
Intercepts (^{o}C)	21.86	-25.56	-3.70	-15.02	4.47
Slopes	4.70	6.88	11.58	9.79	0.96

Table 5. 2: Summary of some of the statistical variables for the values of coefficients a, the intercepts in ^{o}C, and b in equation (5.1) for data set1 and 2 for both G15 and STD detectors.

5.4 Extended Models and Discussions

We believe that the variation of the values of the two constants a and b in equation (5.1) are related to the sky temperatures at the zenith and the screen level temperatures respectively.

At the zenith, $\theta = 0$, equation (5.1) can be reduced to the following:

$$Tsky(\theta = 0) = a \tag{5.3}$$

In this case the constant, *a*, represents the sky temperature at the zenith. This is evident from the close agreement between the statistical values of variable a presented in table (5.2) with those of the measured sky temperature at the zenith found in table (5.1).

In the previous chapter we found that the sky temperature at the zenith can be parameterized as a function of (PWV, Tair) or (*Sqrt(eo)*, Tair). For example for the G15 the sky temperature at the zenith as a function of (*PWV*, *Ta*), equation (4.17), and as a function of screen level measurements (*Sqrt(eo)*, *Ta*), equation (4.32) expressed as:

$$Tsky(\theta=0) = -31.8 + 0.53\,Ta + 0.60\,PWV \tag{5.4}$$

$$Tsky(\theta=0) = -43.9 + 0.75\,Ta + 4.6\,Sqrt(eo) \tag{5.5}$$

On the other hand, at the horizon ($\theta = 90^0$) the sky temperature, is approaching that of black body at a temperature which is very similar to the screen level temperature (see figure 6.4 next chapter for more details),. Therefore equation (5.1) can be reduced to the following:

$$Tsky(\theta = 90^\circ) = Tair \tag{5.6}$$

At an angle of $\theta = 87^o$, three degrees above the horizon, equation (5.6) with some proximity is assumed to be valid. Figure (5.3) is a plot of the sky temperature at 87^o versus the screen level temperature for data *set1* for G15 detector.

A linear fit between the two variables gives:

$$Tsky = 0.88Ta - 1.5 \tag{5.7}$$

with R^2 of 96 % and RMSE of 2 ^{o}C.

The assumption of proximity between the two temperatures is reasonably acceptable from the above discussion and by the fact that at this angle (and below it to the horizon) the sky temperature is very close to the screen level temperature. Consequently, this will facilitate the procedure of finding a physical value for the constant b in equation (5.1).

Recall that in equation (5.1) the slope *b*, can be expressed by:

$$b = \frac{Tsky(\theta = 90) - Tsky(\theta = 0)}{ln(sec(87)) - ln(sec(0))} \tag{5.8}$$

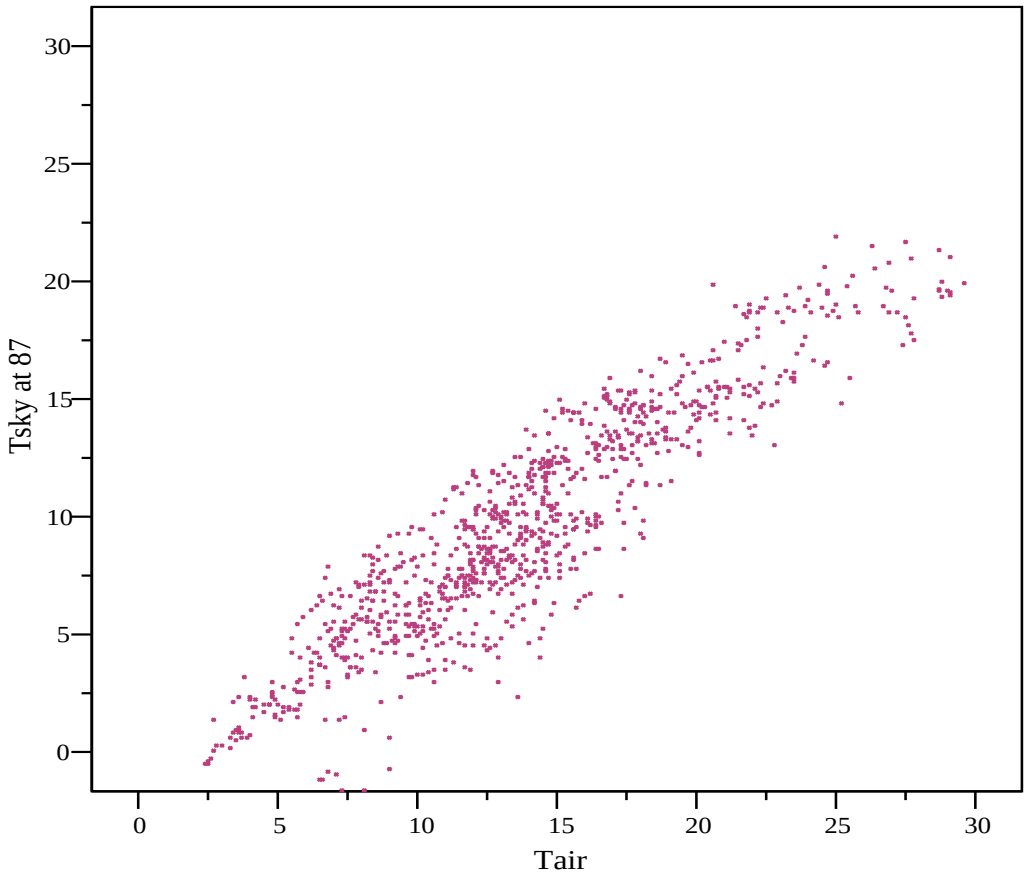

*Figure 5. 3***:** *Shows the relation between the air temperature and the measured sky temperature at 87^{o} zenith angle, both in ^{o}C, for set1 for the G15 detector.*

By applying the above assumptions, and by substituting equations (5.8),(5.6) and (5.3) into equation (5.1), the final expressions for calculating the clear sky temperatures as a function of the zenith angle at any zenith angle, in ^{o}C, for G15 (similar procedure is applicable for the STD detector) is:

$$Tsky(\theta) = [\ Tsky(\theta = 0)\{\ f(PWV, Tair)\} or\{\ f(Sqrt(eo), Tair)\}] + [(\frac{Tair - Tsky(\theta = 0)}{2.95}) ln(sec\,\theta)] \quad (5.9)$$

Where the *Tsky (θ =0) f (PWV,Tair) or f (Sqrt(eo), Tair),* term represents the sky temperature at the zenith equation (5.4), or equation (5.5), and the 2.95 is the approximate value of the *ln(sec(87).*

This can be further written in its full form by inserting equation (5.4) and (5.5) respectively as:

$$T_{\theta} = [(\frac{Tair - Tsky(\theta = 0)}{2.95}) ln(sec\,\theta)] \text{ - } [\ 31.8 - 0.53\ Tair - 0.60\ PWV\ ] \quad (5.10)$$

$$T_{\theta} = [(\frac{Tair - Tsky(\theta = 0)}{2.95}) ln(sec\,\theta)] \text{ - } [\ 43.9 - 0.75\ Tair - 4.6\ Sqrt(eo)] \quad (5.11)$$

The last two equations are in more general form and based on physical relationships between the constants *a*, and *b* rather than based on the experimental values such that of equation (5.2). The next purpose of this study is to test the predictability of these models for the measured values. This will be the topic of the next section. Theoretical justifications for these models will be achieved using MODTRAN software and this will be discussed in chapter 6.

5.5 Validation of the Models

In order to test the expectations of the above equations the sky temperatures predicted by these equations, they were tested against the measured sky temperatures from the zenith to 87^o.

Set2 was used to test equation (5.10) with a total of 331 clear sky temperature scans with their corresponding data of PWV. Similarly, *set1* with 963 scans was used to test equation (5.11). This is the main reason of dividing the data set to two groups.

An algorithm has designed using Mathematica to accomplish this task.

The code was written to do the following tasks:

1. Read the scan from the zenith to 87^o and its corresponding weather variables.
2. Apply the calibration corrections for each detector (G15 or STD) for that scan.
3. Calculate the sky temperature *at the zenith* from the desired model (equation 5.4, or 5.5).
4. Calculate the sky temperature at *all zenith angles* using equation 5.10 and equation 5.11.
5. The code is then allowed to do a linear fit between the measured and calculated zenith sky temperatures for the scan and store the values of the slope, intercept, correlation coefficient and their statistical variables.
6. For that scan, the Mathematica code plots the measured versus predicted sky temperature at each angle, similar to figure (5.8).
7. The code is then run for the whole data set.

The statistics of the results for both the slope and the intercept of the regression analysis between the measured and predicted sky temperatures at zenith angles from the zenith up 87^o are shown in table (5.3). The mean values of the slope for both models for *set1* were close to 1, and vary slightly from this value. The slope mean values for *set2* have values of less than a degree for both models.

Extremes of higher values of slopes and intercept were found which, may be due to an unobserved or unexpected instrumental fault or a strong microclimatic conditions at the time of observations. Also, poorer fit of the model near or at the zenith angle of 87^o have a great impact in producing such discrepancies.

Fig (5.4) and (5.5) show the histogram distributions of both the slopes and the intercept for equation (5.10), data *set2* and equation (5.11), data *set1,* respectively for G15

detector. For both models, the distribution of the slopes and the intercepts is close to the standard normal distributions.

Set1 (N = 963) G15					
	Range	Minimum	Maximum	Mean	Std. Deviation
Intercepts (^{o}C)	0.49	0.88	1.37	1.15	0.10
Slopes	9.04	-2.47	6.57	1.21	1.69
STD					
Intercepts (^{o}C)	0.73	0.96	1.70	1.17	0.13
Slopes	8.78	-2.49	6.29	1.37	1.76
Set 2 (N = 331) G15					
Intercepts (^{o}C)	0.55	0.76	1.31	1.06	0.09
Slopes	16.47	-9.58	6.89	-0.30	2.61
STD					
Intercepts (^{o}C)	0.82	0.63	1.44	1.08	0.11
Slopes	18.26	-8.62	9.63	0.55	2.35

Table 5. 3: Regression analysis of measured sky temperatures and those calculated from equation(5 11) (upper table) and those calculated from equation(5.10) (Lower table).

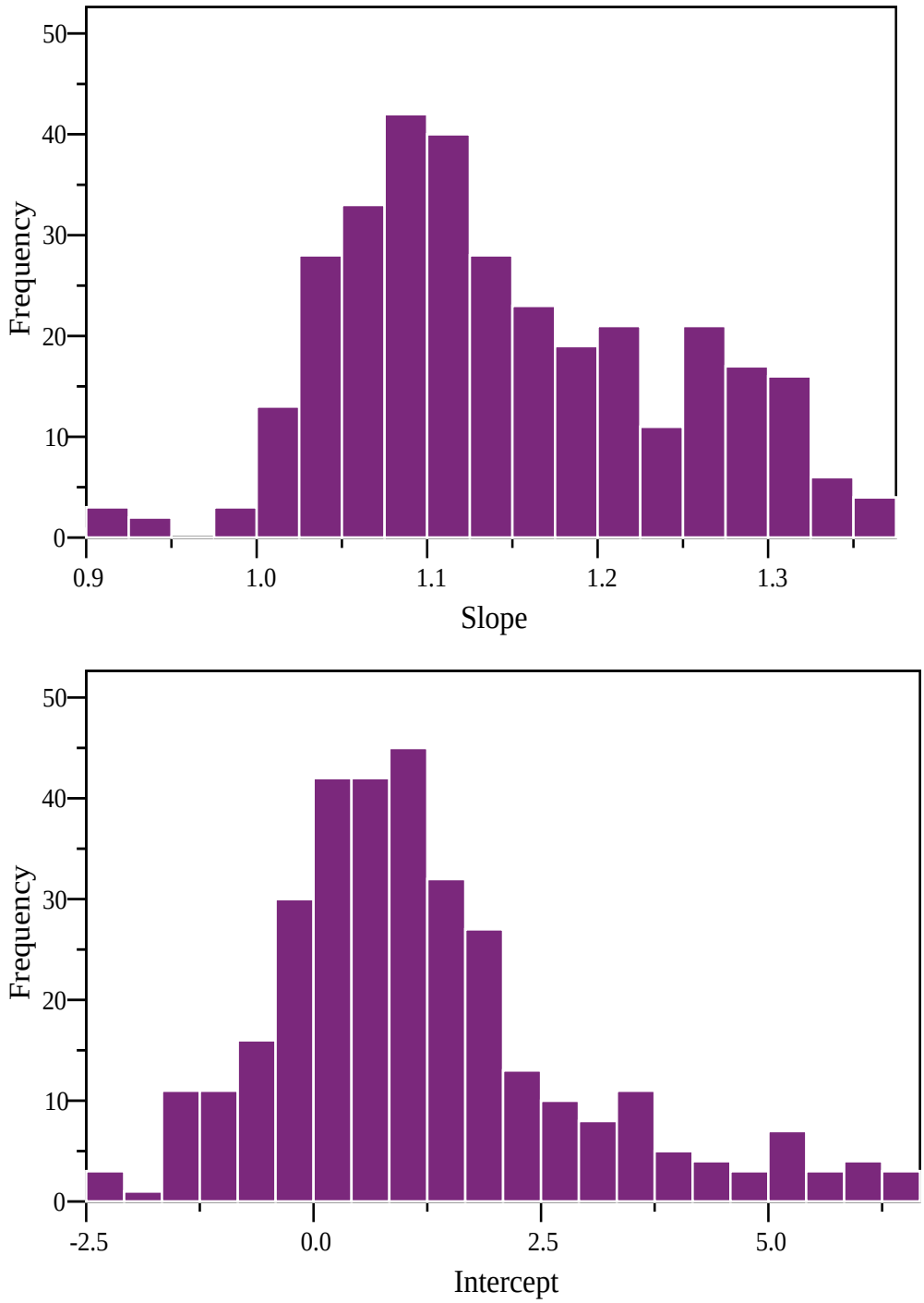

Figure 5. 4: Frequency distribution of the slope (a), and the intercept (b in ^{o}C) of the regression analysis between the measured sky temperatures and those predicted using equation (5.10) for set2 , for the G15 detector.

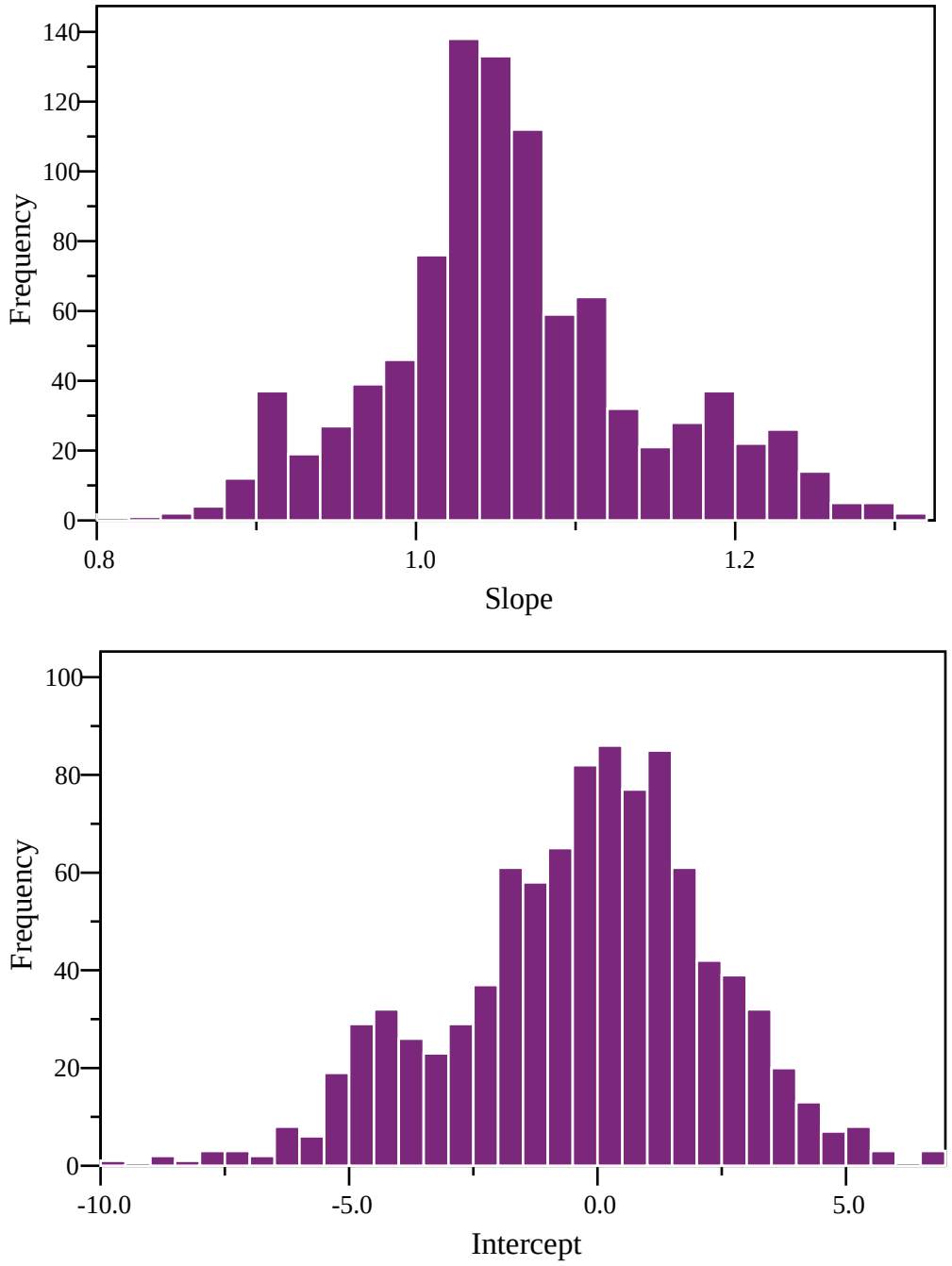

Figure 5.5: Same as figure (5.4) but for sky temperature predicted using equation (5.11) for set1 with the G15 detector.

Figure (5.6) shows a comparison between the measured and the predicted sky temperatures at different zenith angles as predicted using equations (5.10) and (5.11), for a randomly selected scan from eastern to western horizons. The plot shows excellent prediction of both models for the sky temperature at all the zenith angles from 87^{o} West through the zenith to the 87^{o} East side.

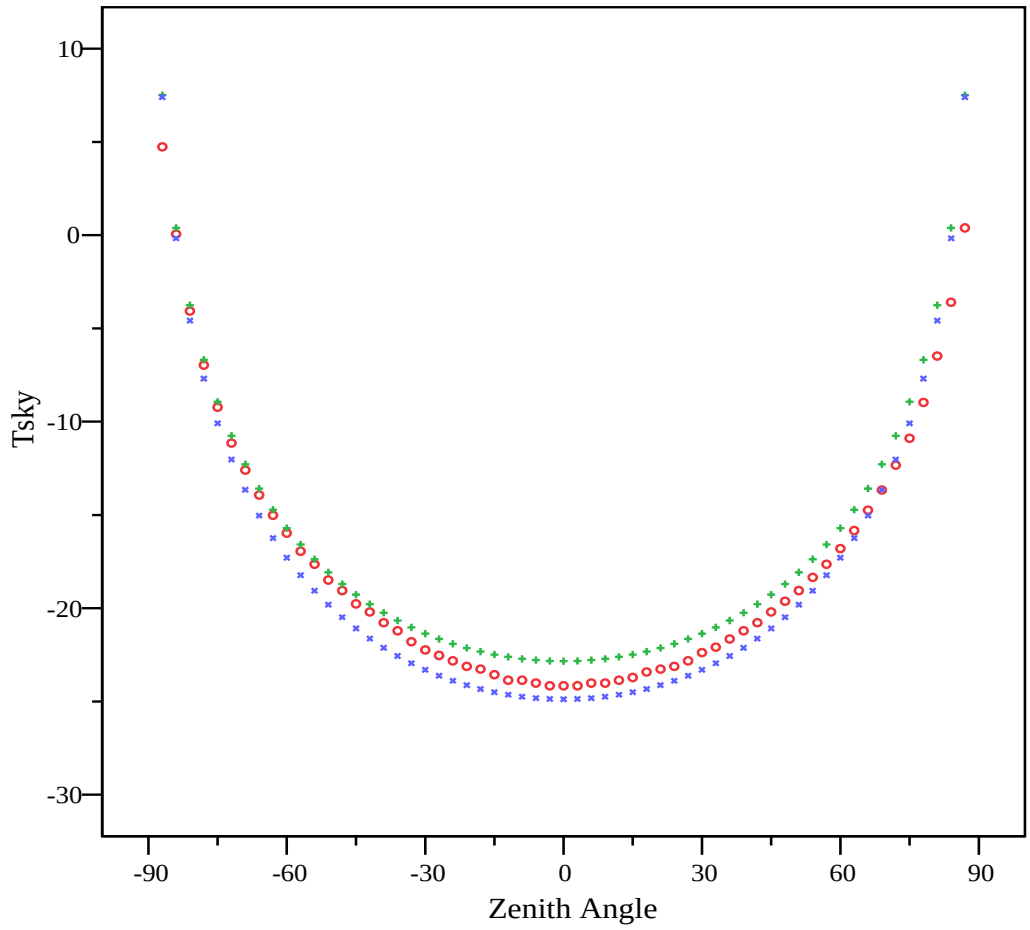

Figure 5. 6: Comparisons between measured sky temperatures and those obtained using equations (5.10) and (5.11) , for a randomly selected scan, light blue× is model (5.11), red ○ measured and green + (5.10).

Figure (5.7) is a comprehensive conclusion of the work conducted in this chapter. It shows the average values of the difference between the measured and the predicted sky temperature, for G15 detector, using equations (5.10) and (5.10) from the zenith to 87^{o}. The graph shows that the maximum mean values of the difference between both temperatures for zenith angles extended from the zenith to an angle slightly above 84^{o} were less than 1.5 ^{o}C. The maximum differences were found at the zenith angle 87^{o}. They were about 4 ^{o}C and 6 ^{o}C for that predicted using of equation (5.10) and equation (5.11) respectively. These larger values are expected to be due to the assumption of the closeness of the sky temperatures at this zenith angle to the air temperature. It may be due to the effect of some of the extreme measurements when averaging the difference at this zenith angle. However, for most of the applications, including those of astrophysical interest, observations at large zenith angles are less important.

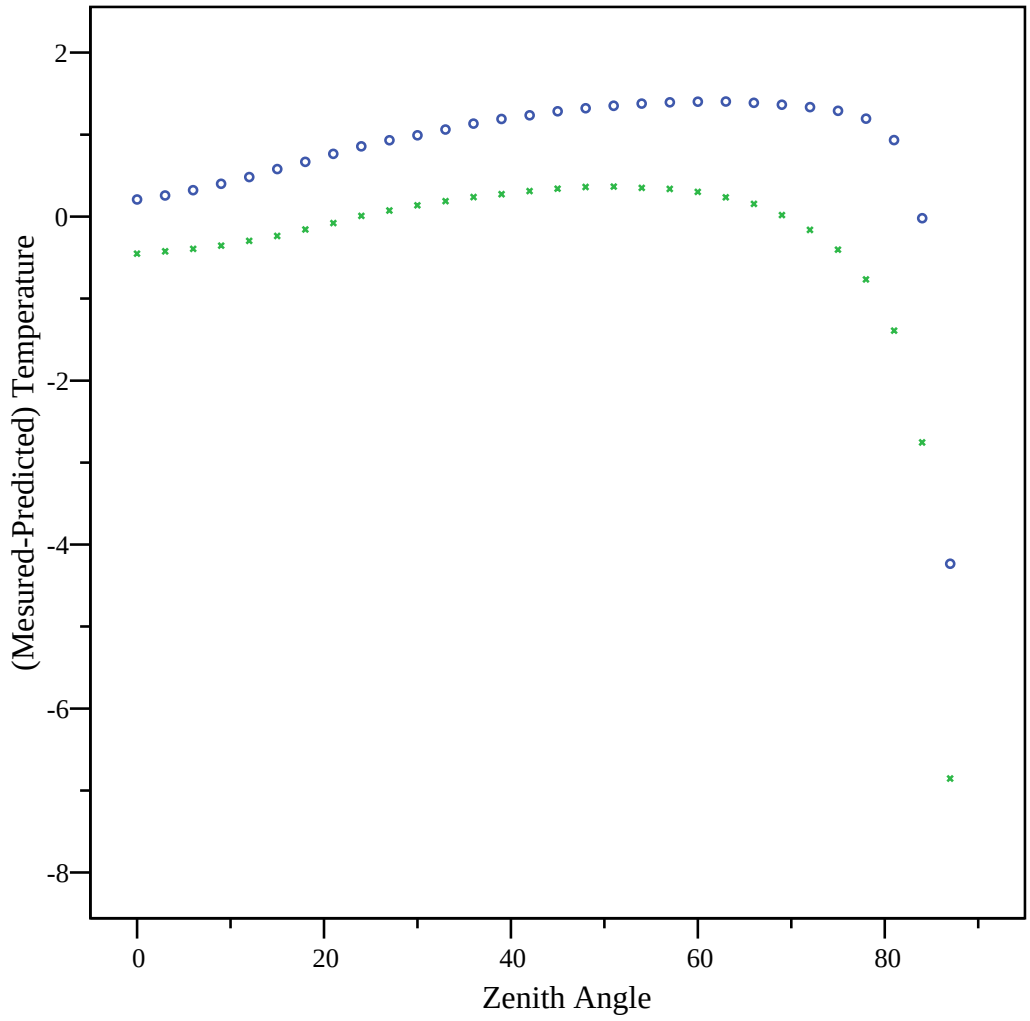

Figure 5. 7: Shows the mean difference between modeled and predicted sky temperatures in ^{o}C (Measured – modeled) as a function of the zenith angle from zenith to 87^{o}. × green and ○ blue is are the differences between measured and predicted using equations (5.10) and (5.11) respectively.

5.6 The Representative Angle

The real IR flux density on a horizontal surface exposed to the whole sky has been found equal to the equivalent flux density at a specific zenith angle. This angle was found to have values between 52.5^{o} and 57^{o}.(Bliss , Berger). The differences in the values result from various integrations of the radiation transfer equation over the hemisphere.

According to Bliss (1963), the monochromatic intensity of radiation originating in an elementary solid angle and striking a small area *dA* is:

$$d^2 q_\lambda = \frac{I_\lambda}{\pi}(1 - \exp(\frac{-k_\lambda m_g}{\cos\theta})) \cos\theta \sin\theta d\theta d\varphi d\lambda \quad (5.12)$$

In which I_λ is the spectral intensity of radiation per unit wavelength, φ the azimuth, and θ the angle from the vertical, m_g is the absorber amount and k_λ is the absorption coefficient. The relation between directional and total emissivity is obtained by integrating equation (5.12). Substituting:

$$x = \frac{k_\lambda m_g}{\cos\theta} = \frac{a}{\cos\theta} \quad (5.13)$$

Then the integration of equation (5.12) yields:

$$dq_\lambda = I_\lambda d\lambda[1 - 2Ei_3(a)] \quad (5.14)$$

In which

$$2Ei_3(a) \equiv 2a\int_a^\infty \frac{e^{-x}}{x}dx = e^{-a} - ae^{-a} + a^2\int_a^\infty \frac{e^{-x}}{x}dx \quad (5.15)$$

The *Ei3* is a mathematical function that does not have a simple expression.
That is:

$$\varepsilon_\lambda = 1 - 2Ei_3(k_\lambda m_g) \approx 1 - \exp(-ab) \quad (5.16)$$

Consequently the relation between the spectral emissivity of a slab and that of a hemisphere depends upon the relation between the function *2Ei3* and the exponential function, which is the *b* value in equation (5.16).
The best *b* value in equation (5.16) can be chosen to minimize the mean error over a wide range of *a* values. Bliss proposed the value of 1.8, while Elsasser choose 1.66. Fig (5.8) is a plot of different values of *b* as suggested by Bliss, Elsasser in the exponential term and 1-2Ei3 functions over a wide range of values.
From the above discussion, the mean equivalent angle for which the emissivity or intensity is the same as that averaged over the whole hemisphere. For b = 1.66 (proposed by Elsasser) $\theta = 53^o$. For b =1.8 (proposed by Bliss) $\theta = 56^o$.

According to equation (5.1), which is similar to that proposed by Unsworth and Monteth (1975), the equivalent sky exposed to the whole sky can be calculated from the integral:

$$Tsky(\theta) = \int_0^{2\pi} d\phi \int_0^{\frac{\pi}{2}} [(a + b \times \ln(\sec\theta))\cos\theta \sin\theta] d\theta \qquad (5.17)$$

$$Tsky(\theta) = \frac{\pi}{2}[2a + b] \qquad (5.18)$$

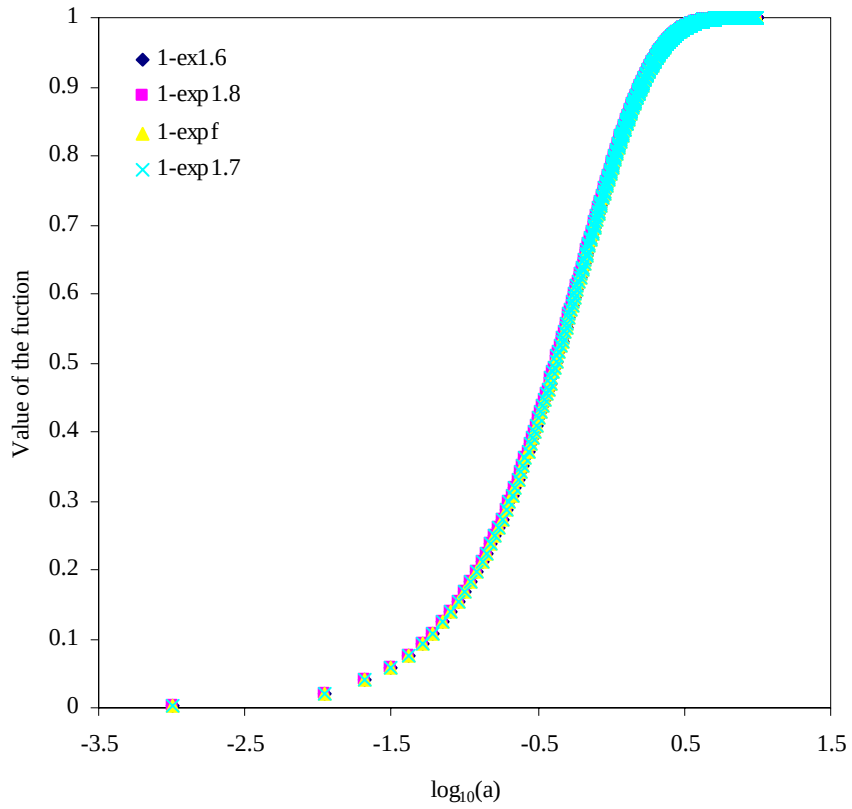

Figure 5. 8. Comparisons of the theoretical function 1-2Ei3(a) , with approximations suggested by Bliss and Elsassr.

It follows then that the equivalent sky temperature on a horizontal surface must be equal to the equivalent sky temperature at an angle θ given by *ln sec θ* = 0.5 which equates to using θ = 52.5^{o}.

The task is now testing the Bliss, Elsasser and the above hypothesis and establishes representative angle experimentally using the available data.

The procedure of achieving the above is firstly to convert (5.17) to a series of sums:

$$T^4\_rep = \frac{\sum_{\theta=0}^{\theta=87} 3(2\pi \sin\theta \cos\theta) T^4(\theta)}{\sum_{\theta=0}^{\theta=87} 3 \times (2\pi \sin\theta \cos\theta)} \quad (5.19)$$

Where the T^4_{rep} is the sky temperature at representative angle. The values of the sky temperature for a particular scan obtained using (5.19) were then compared with the actual measured sky temperatures at different zenith angles from 50^{o} to 60^{o} in order to find the closest measured temperature which matches or give a close value to that calculated temperature using (5.19). The statistics of the calculated sky temperatures using (5.19), measured sky temperatures at 51^{o}, 54^{o}, 57^{o} 60^{o} and 63^{o} and the mean bias error MBE (measured T at these angles– calculated T using the above formula) for the G15 set1 dataset are summarized in table (5.4). The mean sky temperature at the angles 51^{o} and 54^{o} shown the closest values to those predicted using the formula. The MBE between the measured and predicted temperatures at these two angles were less than 0.5 ^{o}C. Also, mean values of the measured sky temperatures at angles 57^{o}, 61^{o}, and 63^{o} and their MBEs show reasonable values with an average MBE no more than 1.7 ^{o}C.

Therefore, measuring sky temperatures at any angle between 51^{o}-63^{0}, with a high accuracy, can be considered as an excellent measure of the sky temperature averaged for the whole hemisphere.

This conclusion was theoretically found in the previous work and confirmed experimentally here.

	Range	Minimum	Maximum	Mean	Std. Deviation
T_rep	38.67	-35.46	3.21	-9.46	5.38
T at 51	38.09	-35.53	2.55	-9.65	5.34
T at 54	38.89	-35.50	3.39	-9.26	5.43
T at 57	40.17	-35.47	4.70	-8.81	5.54
T at 60	40.64	-35.47	5.18	-8.30	5.65
T at 63	41.95	-35.43	6.52	-7.74	5.80
MBE at 51	4.07	-2.14	1.94	0.20	0.24
MBE at 54	5.99	-3.78	2.21	-0.20	0.29
MBE at 57	6.96	-4.75	2.21	-0.65	0.36
MBE at 60	6.50	-4.93	1.57	-1.15	0.44
MBE at 63	5.94	-5.38	0.56	-1.72	0.59

Table 5. 4: Shows the statistics of the measured sky temperatures at four zenith angles (51^o, 54^o, 57^o ,60^o and 63^o) compared to the temperature calculated using equation (5.19) (T_rep) . It also shows the statistics of the differences between calculated and measured at same angles, MBE. The unit for all variables is ^oC. The lowest mean value corresponds to the best fit.